Supplemental Material (SM): Lone pair localization governs ferroelectric stability and excitonic properties in lead free halide perovskites

Shahrbano Rahimi[1] and S. Jalali-Asadabadi [a1,†]

[1]*Department of Physics, Faculty of Physics, University of Isfahan (UI), Hezar Jerib Avenue, 8174673441 Isfahan, Iran*

This Supplementary Material (SM) provides the complete theoretical, computational, and analytical foundation supporting the main manuscript *"Lone pair localization governs ferroelectric stability and excitonic properties in lead free halide perovskites."* It expands upon the coupled lattice–electronic hierarchy underlying $CsGeX_3$ (X = Cl, Br, I) and Rb-alloyed derivatives, uniting first-principles ferroelectric, electronic, and excitonic analyses. The SM details the full GGA→G_0W_0 →BSE workflow for quasiparticle and excitonic spectroscopy, the Berry-phase and Born effective charge (BEC) formalisms for spontaneous polarization, and the real-space charge topology explored via Bader and ELF analyses. Comprehensive datasets include optimized structures, formation energies, band structures, dielectric spectra, polarization pathways, and Python scripts for generating intermediate ferroelectric configurations and quantifying lone-pair localization. Integrating many-body optics with polarization theory and charge-density topology, the SM establishes a quantitative bridge between lone-pair stereochemistry, dielectric screening, and excitonic confinement. The results reveal that electronic localization, rather than geometric distortion alone, governs ferroic robustness and light–matter coupling in these perovskites. Collectively, the materials, data, and code form a reproducible roadmap for the design of multifunctional, lead-free photoferroelectrics with tunable polarization and excitonic responses.

CONTENTS

[a] E-mail: saeid.jalali.asadabadi@gmail.com; Tel: +98-031-37934776; Fax: +98-031-37932800

[†] Corresponding author: sjalali@sci.ui.ac.ir; saeid.jalali.asadabadi@gmail.com

SM1. COMPUTATIONAL WORKFLOW AND THEORETICAL FRAMEWORK

Figure SM1 outlines the integrated multi-tiered computational framework developed to connect the structural, electronic, and excitonic hierarchies governing the ferroic and optoelectronic properties of $CsGeX_3$ halide perovskites and their Rb-substituted or pressure-tuned derivatives. This workflow unifies density-functional theory (DFT), many-body perturbation theory, and polarization topology within a consistent Exciting–G_0W_0–BSE and WIEN2k framework, enabling a quantitative and self-consistent mapping between lone-pair asymmetry, ferroelectric stability, and excitonic dynamics in $CsGeX_3$ halide perovskites.

The procedure begins with the generation of atomic structures in the hexagonal $R3m$ symmetry, selected for its noncentrosymmetric topology conducive to spontaneous polarization. Chemical substitution (A = Cs, Rb; B = Ge; X = Cl, Br, I) and external pressure are systematically varied to simulate the effects of chemical pressure, octahedral tilting, and bond compressibility on the structural landscape. These configurations serve as the foundation for subsequent electronic-structure and excitonic analyses.

Ground-state DFT calculations, performed using the EXCITING full-potential linearized augmented-plane-wave (FP-LAPW) code within the generalized gradient approximation (GGA-PBE), yield self-consistent charge densities $\rho(\mathbf{r})$, Kohn–Sham eigenvalues, and potential landscapes. These data establish the reference electronic manifold for quasiparticle corrections and optical response modeling. The method ensures an all-electron description of both cationic lone pairs and halogen p-states, which are essential for accurately capturing ferroelectric distortions and charge asymmetry.

The single-shot G_0W_0 formalism is subsequently employed to incorporate many-body screening effects and self-energy corrections beyond DFT. This stage renormalizes the band edges, yielding quasiparticle gaps E_g^{e} and the screened Coulomb interaction $W(\mathbf{r}, \mathbf{r}')$, which directly feed into the Bethe–Salpeter equation (BSE). Within the Tamm–Dancoff approximation (TDA), the BSE explicitly accounts for electron–hole correlations, generating the excitonic dielectric tensor $\varepsilon_{xx,yy,zz}(\omega)$, optical transition energies E_g^{opt}, and exciton binding energies E_b^{ex}. The resulting spectra capture excitonic confinement, anisotropy in the dielectric tensor $\varepsilon_{xx,yy,zz}(\omega)$, and the interplay between ionic distortions and optical absorption.

In parallel, ferroelectric and real-space electronic analyses are performed using the all-electron WIEN2K package, interfaced with custom Python automation for structural interpolation and post-processing. The Berry-phase method and Born effective charge (BEC) analysis provide the spontaneous polarization P_s and switching pathways $P(\lambda)$, while double-well energetics $\Delta E(\lambda)$ quantify the energy barrier for polarization reversal. These quantities together define the structural component of the ferroelectric free-energy surface.

Complementary real-space descriptors are extracted from the charge density using the electron localization function (ELF) and Bader charge analysis. The ELF mapping reveals the stereochemical activity of the Ge $4s^2$ lone pairs and their coupling to lattice displacements, while Bader partitioning yields atomic charge deviations $|\Delta q_i|$ and charge-transfer trends. The lone-pair localization index η_{lp}, derived from the processed ELF maps, provides a direct measure of the asymmetry in electron localization and serves as a bridge between ferroelectric and excitonic observables.

The final post-processing stage evaluates the complex dielectric function and energy-loss spectra $\mathrm{Im}[-1/\varepsilon(\omega)]$, tracing the evolution of excitonic and plasmonic resonances under chemical substitution and pressure. This integrated hierarchy—spanning atomic structure, polarization topology, electronic quasiparticles, and excitonic response—captures the cooperative nature of structure–electron–photon coupling in $CsGeX_3$. The resulting framework enables a predictive understanding of how lone-pair-driven symmetry breaking governs both the ferroic and optoelectronic behavior of lead-free halide perovskites, establishing design rules for next-generation photoferroelectric materials with tunable excitonic and polarization properties.

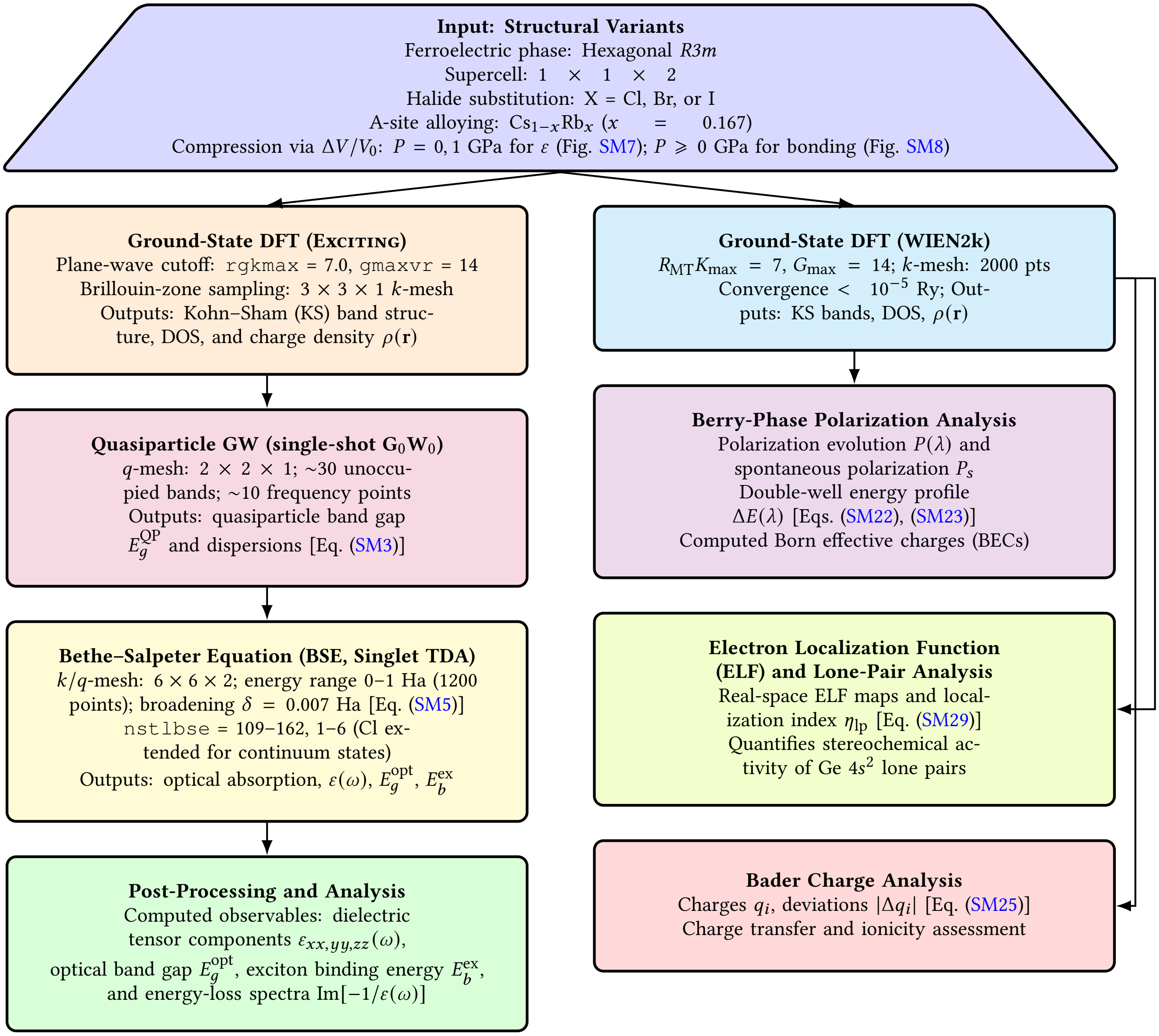

FIG. SM1. **Integrated Exciting–G_0W_0–BSE and WIEN2k workflow linking ferroelectric switching, electronic structure, and excitonic response in $CsGeX_3$ halide perovskites.** The diagram summarizes the fully automated first-principles pipeline coupling structural, electronic, and optical analyses across two complementary branches. The shared input stage defines the halide composition (X = Cl, Br, I), partial Rb substitution at the Cs site, and applied hydrostatic pressure within the hexagonal $R3m$ symmetry. The Exciting branch (left) traces the quasiparticle and excitonic hierarchy from ground-state DFT through single-shot G_0W_0 and Bethe–Salpeter equation (BSE) calculations, providing dielectric tensor components, optical gaps E_g^{opt}, exciton binding energies E_b^{ex}, and energy-loss spectra $\mathrm{Im}[-1/\varepsilon(\omega)]$. The WIEN2k branch (right) performs ferroelectric and bonding analyses, including Berry-phase polarization $P(\lambda)$, double-well energetics $\Delta E(\lambda)$, Born effective charges (BECs), electron localization function (ELF)–derived lone-pair asymmetry η_{lp}, and Bader charge partitioning Δq_i. Together, these parallel workflows provide a quantitative link between lattice distortion, lone-pair activity, and excitonic confinement—revealing the microscopic origin of optoferroelectric coupling in $CsGeX_3$.

SM2. ELECTRONIC BAND STRUCTURE FROM GGA AND G_0W_0 APPROXIMATIONS

Figure SM2 presents the Kohn–Sham (KS) and quasiparticle (G_0W_0) band structures along the high-symmetry path Γ–K–X–Γ–L in the first Brillouin zone for pristine and Rb-substituted $CsGeX_3$ (X = Cl, Br, I) halide perovskites, revealing the cooperative effects of halogen chemistry and A-site alloying on the electronic landscape. The KS dispersions, obtained within the GGA–PBE functional, define the mean-field reference, while the single-shot G_0W_0 correction introduces dynamical self-energy effects that properly account for nonlocal exchange and many-body screening.

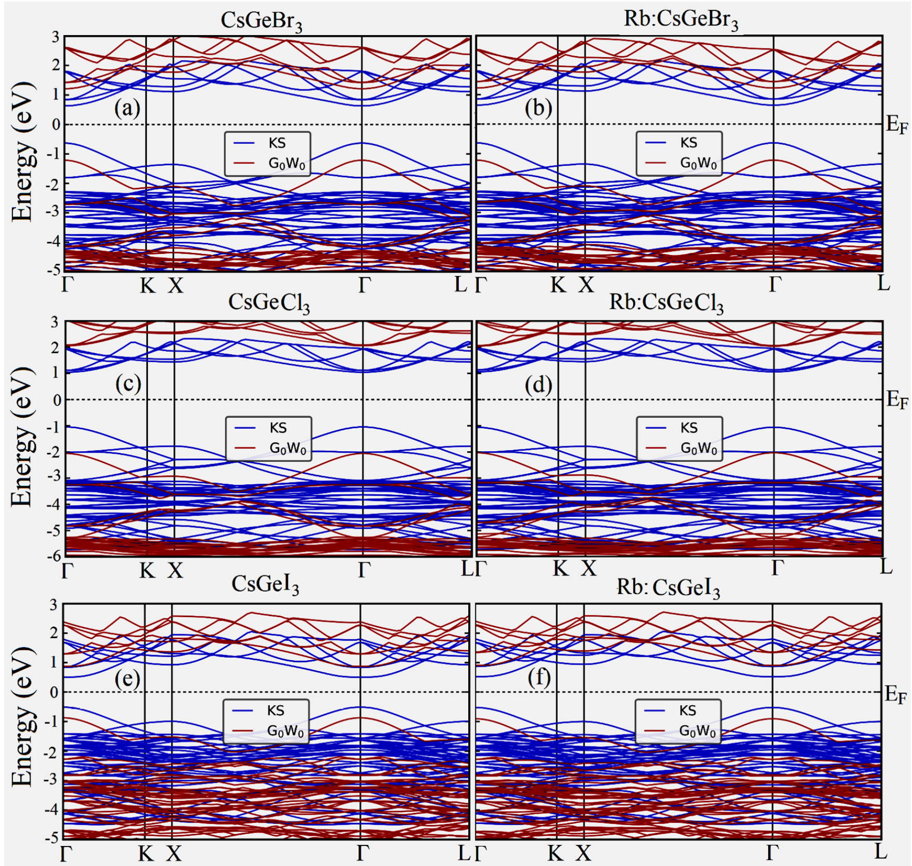

FIG. SM2. **Electronic band structures of pristine and Rb-alloyed $CsGeX_3$ halide perovskites.** Kohn–Sham (KS, blue) and quasiparticle (G_0W_0, red) dispersions are shown for $CsGeCl_3$, $CsGeBr_3$, and $CsGeI_3$, along with their Rb-substituted counterparts. The KS bands, computed within the GGA-PBE functional, provide the mean-field reference, while single-shot G_0W_0 corrections introduce self-energy shifts that systematically widen the band gaps by 0.6–2 eV across the series. All systems preserve a direct Γ-point gap, with the degree of dispersion and gap magnitude governed by halogen-dependent screening and Ge–X orbital hybridization. Rb substitution produces modest conduction-band upshifts and valence-band flattening, particularly in $CsGeCl_3$, signifying enhanced Ge *s*–X *p* coupling and increased lone-pair localization under chemical pressure. These refined quasiparticle dispersions form the foundation for subsequent Bethe–Salpeter Equation (BSE) analyses of excitonic behavior and dielectric response.

Across the halide sequence, all compounds maintain a direct band gap at the Γ point, consistent with their noncentrosymmetric *R3m* symmetry and three-dimensional Ge–X network. The G_0W_0 corrections substantially widen the KS band gaps from 2.070, 1.264, and 1.039 eV to 4.111, 2.424, and 1.704 eV for $CsGeCl_3$, $CsGeBr_3$, and $CsGeI_3$, respectively. These values are in close agreement with prior G_3W_0 calculations [1] and consistent with experimental optical data [2–4], confirming the reliability of the GGA starting point for quasiparticle refinement. The systematic reduction of the gap from Cl to I reflects the progressive increase in halogen polarizability and dielectric screening, which attenuates electron–hole exchange and enhances hybridization between Ge *s* and X *p* orbitals.

Rb substitution, which effectively applies chemical pressure by reducing the A-site ionic radius, acts as an isoelectronic but structurally active dopant. It preserves the direct-gap character while slightly modulating the gap energies to 4.059, 2.445, and 1.758 eV for Rb:$CsGeCl_3$, Rb:$CsGeBr_3$, and Rb:$CsGeI_3$, respectively. The subtle conduction-band upshift and valence-band flattening—most pronounced in Rb:$CsGeCl_3$—indicate enhanced localization of the Ge *s*–X *p* antibonding states and increased stereochemical activity of the Ge $4s^2$ lone pair. These electronic signatures mirror the real-space trends observed in the electron localization function (ELF) and Bader analyses (Sec. SM7), providing a consistent multiscale picture that links local bonding asymmetry to macroscopic polarization stability.

The halogen-dependent trends further clarify the interplay between orbital hybridization and dielectric screening: lighter halides (Cl) exhibit more ionic Ge–X bonding, stronger quasiparticle shifts, and steeper conduction-band curvature, while heavier halides (Br, I) display enhanced *p*–*p* overlap, smaller self-energy corrections, and reduced effective masses. This chemical sequence not only rationalizes the variation in optical gap renormalization but also establishes a microscopic link between halogen polarizability, excitonic binding energy, and polarization-driven charge separation.

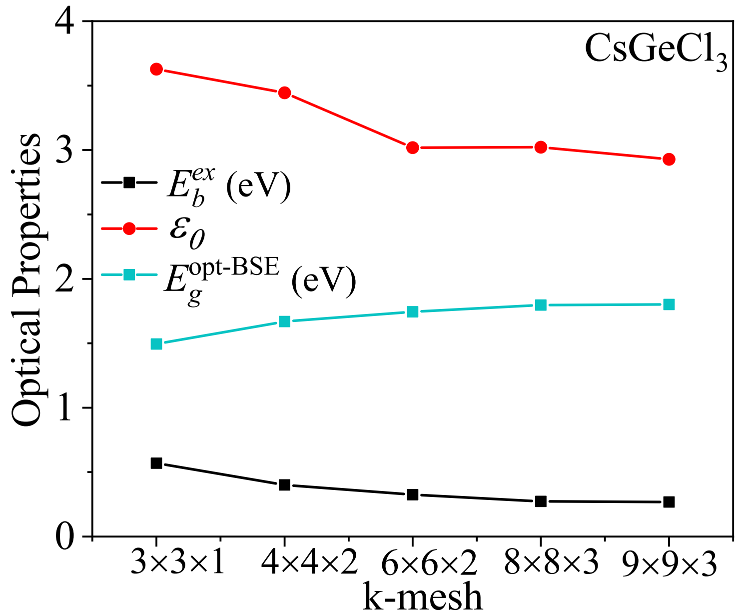

FIG. SM3. **Convergence of excitonic and dielectric properties with k-mesh sampling in $CsGeCl_3$.** The exciton binding energy (E_b^{ex}), optical gap ($E_g^{opt-BSE}$), and static dielectric constant (ε_0) are evaluated for progressively denser k-meshes within the GGA+BSE framework. As the sampling grid is refined from $3\times3\times1$ to $9\times9\times3$, both ε_0 and $E_g^{opt-BSE}$ exhibit smooth convergence, while E_b^{ex} decreases and stabilizes near 0.25 eV, consistent with the hydrogenic scaling relation $E_b^{ex} \propto \mu/\varepsilon_0^2$. A $6\times6\times2$ grid achieves quantitative convergence of the dielectric screening and excitonic response, and is therefore adopted for all subsequent BSE analyses across the $CsGeX_3$ series.

Overall, the G_0W_0 results quantitatively refine the GGA electronic structure while preserving its qualitative topology, providing self-consistent inputs for Bethe–Salpeter Equation (BSE) calculations of excitonic and dielectric properties. When combined with Berry-phase polarization and real-space lone-pair descriptors, these quasiparticle band structures reveal how chemical pressure, halogen chemistry, and electronic localization jointly dictate the optoelectronic behavior of lead-free $CsGeX_3$ photoferroelectrics.

SM3. CONVERGENCE OF OPTICAL PROPERTIES WITH *K*-MESH SAMPLING

Figure SM3 presents the convergence behavior of the exciton binding energy (E_b^{ex}), optical band gap ($E_g^{opt-BSE}$), and static dielectric constant (ε_0) of pristine $CsGeCl_3$ as a function of Brillouin-zone sampling density. These quantities, derived from fully converged GW quasiparticle energies and Bethe–Salpeter Equation (BSE) excitonic calculations, quantify how optical observables depend on the accuracy of momentum-space integration over the electronic states.

At coarse sampling ($3\times3\times1$), the reduced number of k-points artificially confines the exciton wavefunction in reciprocal space, leading to an overestimation of E_b^{ex} and an underestimation of both ε_0 and $E_g^{opt-BSE}$. As the grid density increases, finer sampling more accurately captures long-range electron–hole correlations and the dielectric screening response, causing ε_0 to rise and E_b^{ex} to drop toward its intrinsic limit. This inverse relation between exciton binding and screening strength reflects the hydrogenic scaling law $E_b^{ex} \propto \mu/\varepsilon_0^2$, where μ is the reduced effective mass of the quasiparticle pair. The optical gap, $E_g^{opt-BSE}$, saturates near 2.0 eV, in good agreement with the theoretically predicted excitonic transition energy of $CsGeCl_3$. When quasiparticle corrections are included at the G_0W_0 level, the resulting optical gap accurately reproduces the experimentally observed transition energy, as summarized in Table SM2.

The dielectric constant ε_0 converges gradually with increasing mesh density, plateauing around $6\times6\times2$, beyond which variations are below 2%. Meanwhile, E_b^{ex} decreases asymptotically and stabilizes near 0.25 eV, signifying that the exciton binding energy is quantitatively converged and largely insensitive to further sampling refinement. This value is in line with typical binding energies observed in halide perovskites, confirming that $CsGeCl_3$ supports moderately bound Wannier-type excitons rather than strongly localized Frenkel states.

From a computational standpoint, the $6\times6\times2$ k-grid represents the optimal balance between accuracy and efficiency, ensuring convergence of dielectric screening, optical spectra, and exciton energetics within a tolerance of 0.05 eV. This con-

TABLE SM1. **Formation energies and thermodynamic stability of Rb-alloyed $CsGeX_3$ halide perovskites.** Total, atomic, and formation energies of $Cs_{0.83}Rb_{0.17}GeCl_3$, $Cs_{0.83}Rb_{0.17}GeBr_3$, and $Cs_{0.83}Rb_{0.17}GeI_3$ are reported in Rydberg (Ry). All compounds exhibit negative formation energies (E_{form}), confirming their thermodynamic stability with respect to decomposition into the elemental reference phases. The decreasing magnitude of E_{form} from Cl to I reflects the progressive weakening of Ge–X bonding and increasing lattice softness along the halide sequence, consistent with enhanced ionic polarizability and reduced cohesive energy in the heavier anions.

	$Cs_{0.83}Rb_{0.17}GeCl_3$	$Cs_{0.83}Rb_{0.17}GeBr_3$	$Cs_{0.83}Rb_{0.17}GeI_3$
Total energy (Ry)	−125671.8008786	−202896.4969583	−365342.8367837
Sum of atomic energies (Ry)	−125665.2584360	−202891.0070720	−365338.8065900
Formation energy E_{form} (Ry)	−6.5424426	−5.4898863	−4.0301937

vergence threshold was therefore adopted uniformly for all BSE calculations—both with and without G_0W_0 quasiparticle corrections—across the $CsGeX_3$ and Rb:$CsGeX_3$ systems, ensuring consistent accuracy in comparative analyses of excitonic confinement, dielectric anisotropy, and halogen-dependent screening.

Overall, this convergence behavior highlights the delicate coupling between electronic structure resolution, dielectric response, and excitonic physics in these polar halide perovskites. Accurate k-mesh sampling is essential not only for obtaining reliable optical gaps but also for capturing the interplay between long-range polarization fields and the short-range hybridization effects that govern the photoferroelectric response of $CsGeX_3$-based compounds.

SM4. FORMATION ENERGIES AND THERMODYNAMIC STABILITY

Table SM1 summarizes the computed total, atomic, and formation energies for Rb-alloyed $Cs_{0.83}Rb_{0.17}GeX_3$ (X = Cl, Br, I) halide perovskites. The formation energy,

$$E_{\text{form}} = E_{\text{tot}}(Cs_{0.83}Rb_{0.17}GeX_3) - \sum_i n_i E_{\text{tot}}(i), \tag{SM1}$$

was evaluated relative to the energies of the constituent elemental reference phases, where n_i is the number of atoms of species i in the stoichiometric unit.

All three compounds exhibit negative E_{form} values ranging from −6.54 Ry (Cl) to −4.03 Ry (I), confirming their thermodynamic stability against spontaneous decomposition into elemental Cs, Rb, Ge, and X phases. The magnitude of E_{form} decreases systematically from Cl to I, following the established halogen trend of diminishing Ge–X bond strength and increasing lattice softness. This sequence reflects a gradual transition from a more covalent (Cl-rich) to a more ionic (I-rich) bonding regime, which reduces the cohesive energy and enhances the polarizability of the crystal lattice.

The substantial negative formation energies of $Cs_{0.83}Rb_{0.17}GeCl_3$ and $Cs_{0.83}Rb_{0.17}GeBr_3$ indicate that partial Rb incorporation—equivalent to ∼16.7% substitution on the Cs site—does not compromise thermodynamic stability. Instead, the smaller Rb^+ ion introduces a mild chemical pressure, leading to a contracted A-site environment that reinforces Ge off-centering and enhances the stereochemical activity of the Ge $4s^2$ lone pair. This alloy-induced internal strain preserves the perovskite lattice topology while modulating the energy landscape governing ferroelectric and excitonic coupling (see Sec. SM2 and SM3).

In contrast, the lower-magnitude E_{form} observed for $Cs_{0.83}Rb_{0.17}GeI_3$ highlights the thermodynamic softness of the iodide phase. The weaker Ge–I interactions and enhanced anion polarizability result in reduced lattice cohesion and a tendency toward larger dielectric response, as later manifested in the exciton binding and ELF analyses (Sec. SM7). Nevertheless, the negative E_{form} still ensures intrinsic stability under moderate temperature and pressure, confirming that Rb substitution remains chemically viable across the halide series.

These energetic trends, combined with the observed evolution of electronic gaps and polarization strength, establish that the thermodynamic stability of $Cs_{1-x}Rb_xGeX_3$ compounds arises from a delicate balance between ionic polarizability, Ge–X hybridization, and chemical pressure effects. The decreasing formation energy from Cl to I captures the underlying physics of softer lattice dynamics and increased dielectric screening, which in turn underpin the tunability of excitonic and ferroelectric responses in this class of lead-free photoferroelectric perovskites.

SM5. FERROELECTRIC SWITCHING PATHWAY BETWEEN CENTROSYMMETRIC AND POLAR PHASES

Figure SM4 illustrates the ferroelectric switching pathway in $CsGeX_3$ (X = Cl, Br, I), tracing the structural evolution from the centrosymmetric cubic $Pm\bar{3}m$ phase ($\lambda = 0$) to the polar rhombohedral $R3m$ ground state ($\lambda = 1$). The transformation follows a displacive mechanism driven primarily by off-centering of the Ge cation within its GeX_6 octahedron, accompanied

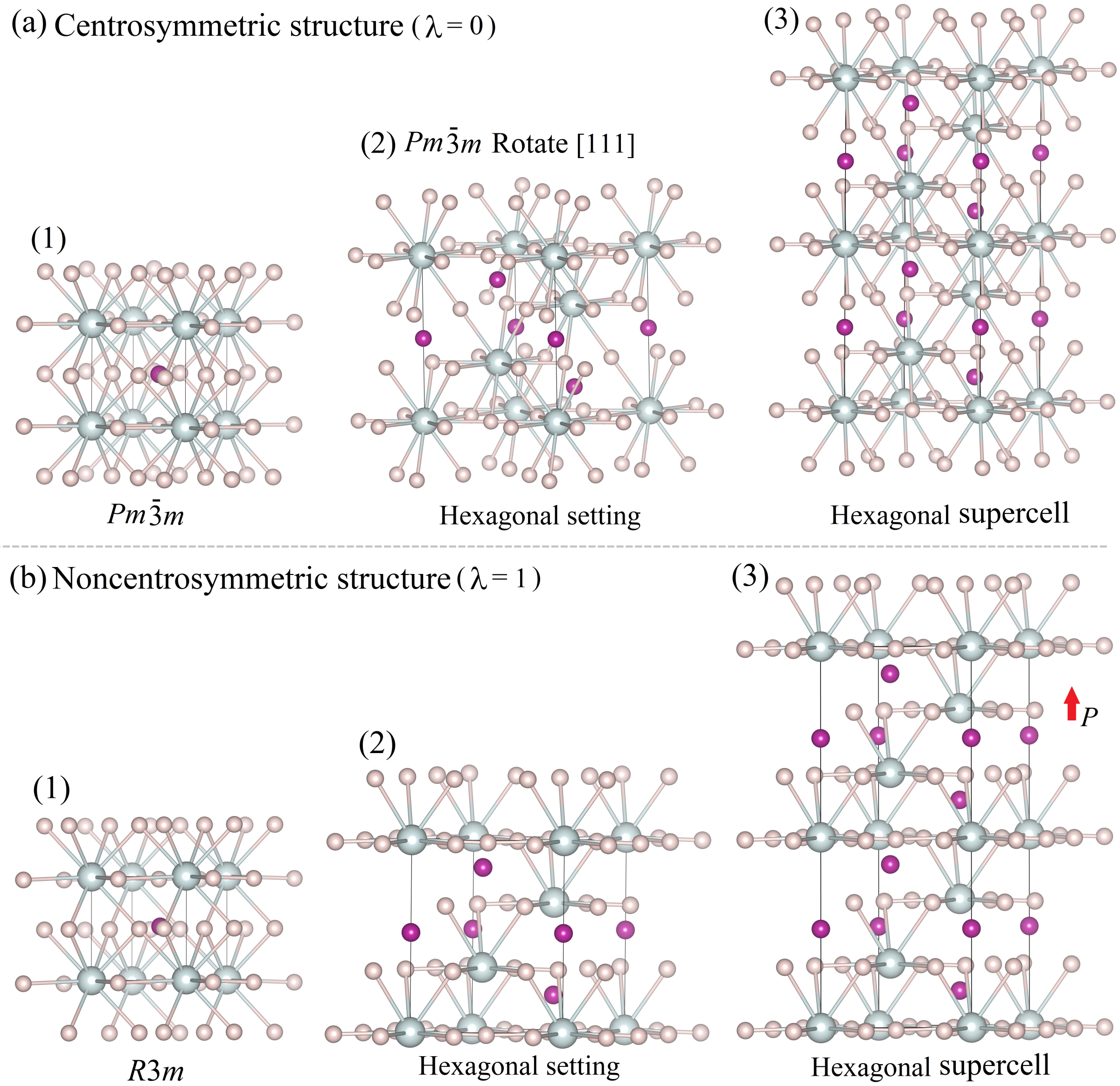

FIG. SM4. **Ferroelectric switching pathway in $CsGeX_3$ halide perovskites.** (a) Centrosymmetric configuration ($\lambda = 0$) and (b) polar configuration ($\lambda = 1$) are illustrated in their equivalent hexagonal representations. The $Pm\bar{3}$m reference structure (top row) is aligned along the cubic [111] axis and expanded to a $1 \times 1 \times 2$ hexagonal supercell, while the lower row presents the polar $R3m$ phase with spontaneous polarization $\boldsymbol{P}$ along the body-diagonal. Intermediate configurations ($0 < \lambda < 1$) are generated by linear interpolation of atomic coordinates, providing a continuous and symmetry-consistent switching coordinate for Berry-phase polarization and double-well energy calculations.

by cooperative distortions of the surrounding halide framework. These concerted displacements align along the cubic [111] axis, corresponding to the direction of spontaneous polarization, and preserve the overall rhombohedral symmetry throughout the interpolation pathway.

The centrosymmetric reference is constructed by rotating the ideal cubic lattice along [111] and replicating it into a $1 \times 1 \times 2$ hexagonal supercell to align the structural axis with the polarization direction. The polar endpoint corresponds to the experimentally observed $R3m$ configuration, characterized by a nonzero dipole moment arising from asymmetric Ge–X bond lengths and stereochemically active Ge $4s^2$ lone-pair electrons. This asymmetry induces a local crystal-field distortion that couples strongly with the macroscopic polarization $\boldsymbol{P}$, establishing a direct link between lattice geometry and electronic localization.

Intermediate configurations ($0 < \lambda < 1$) were generated using the automated Python-based interpolation framework described in Sec. SM6. The linear interpolation of fractional coordinates between the two limiting structures yields a sequence of geometries that continuously sample the ferroelectric switching coordinate λ, ensuring that atomic identities, lattice periodicity, and site symmetries are rigorously preserved. This approach produces a physically meaningful and reproducible mapping of the double-well potential $\Delta E(\lambda)$ and corresponding polarization pathway $\boldsymbol{P}(\lambda)$.

The total and spontaneous polarizations were evaluated using the modern Berry-phase formalism [5–7], as implemented in WIEN2k. This approach, complemented by Born effective charge (BEC) analysis, enables a rigorous decomposition of ionic and electronic polarization components while preserving gauge invariance under periodic boundary conditions. The computed spontaneous polarization $\boldsymbol{P}_s$ values obtained using the PBE-GGA and two meta-GGA functionals (mTASK and r2SCAN) exhibit close agreement with experimental data (Sec. SM11 B 3), confirming the reliability of the adopted exchange–correlation framework in capturing both the ionic displacement amplitude and the electronic polarization response.

From an energetic perspective, the resulting $\Delta E(\lambda)$ profile forms a symmetric double-well potential centered at $\lambda = 0$, characteristic of a second-order displacive ferroelectric transition. The well depth and barrier height decrease systematically from Cl to I substitution, reflecting the chemical-pressure-driven softening of the Ge–X bonds and enhanced dielectric screening in heavier halides. This trend directly mirrors the observed reduction in spontaneous polarization and exciton binding energy across the halide series, underscoring the intimate coupling between lattice polar distortions, lone-pair asymmetry, and optical dielectric response.

In summary, the pathway depicted in Fig. SM4 encapsulates the microscopic mechanism of ferroelectric switching in $CsGeX_3$: a collective off-centering of Ge atoms stabilized by asymmetric Ge–X hybridization and modulated by halogen chemistry. The smooth, symmetry-preserving interpolation ensures that the Berry-phase evaluation of polarization and total-energy profile provides a complete and self-consistent description of the structural–electronic interplay underlying the photoferroelectric functionality of these halide perovskites.

SM6. AUTOMATED GENERATION OF INTERMEDIATE FERROELECTRIC STRUCTURES

To efficiently construct the ferroelectric switching pathway, a dedicated Python-based automation framework was developed to update and interpolate atomic coordinates between the centrosymmetric (CS) and polar (FE) configurations. The workflow systematically generates a series of intermediate geometries that sample the collective switching coordinate λ ($0 \leq \lambda \leq 1$), providing a continuous, symmetry-consistent trajectory between the two energy minima.

The computational scheme reads the reference structural file (`original_structure.struct`), as given at the end of this section for $CsGeCl_3$, replaces the atomic coordinates with new fractional positions corresponding to the desired interpolation step, and writes the updated data into a new file (`new_structure.struct`). Each atomic site retains its chemical identity, labeling, and structural format to ensure compatibility with downstream *ab initio* packages and maintain reproducibility across all generated configurations.

The implementation, summarized in Listing 1, employs a structured read–modify–write procedure. After loading the reference file, the script verifies that the number of supplied fractional coordinates matches the number of atomic entries beginning with the keyword `AT`. This validation step prevents structural mismatches that could arise from inconsistent atom counts or manual editing errors. The script then iterates through each line, dynamically replacing the old coordinates with new interpolated ones while preserving non-atomic metadata such as lattice parameters, symmetry operations, and header information. The result is a fully updated structure file that reflects the target geometry along the ferroelectric switching path.

Python Script for Updating Atomic Positions. A custom Python routine was developed to automate the generation of intermediate structures used in the Berry-phase polarization and double-well energy calculations. The script reads an existing WIEN2k `.struct` file, replaces the atomic fractional coordinates with interpolated values between centrosymmetric ($\lambda = 0$) and polar ($\lambda = 1$) configurations, and writes a new `new_structure.struct` file. All non-atomic metadata—such as lattice parameters, species definitions, muffin–tin radii, and local rotation matrices—are preserved to ensure strict compatibility with downstream WIEN2k calculations. Only the atomic `AT` records are renumbered and updated, maintaining structural integrity while enabling fully automated generation of intermediate configurations for polarization-pathway analyses. This utility script performs a routine preprocessing task to ensure reproducibility and consistency across the ferroelectric switching simulations.

```python
# ================================================
# Replace Atomic Coordinates in a Structure File
# ================================================

# --- Read the original structure file ---
with open("original_structure.struct", "r") as f:
    lines = f.readlines()

# --- Define new atomic positions (fractional coordinates) ---
new_positions = [
    [0.00000000, 0.00000000, 0.49996977],
    [0.00000000, 0.00000000, 0.99996986],
    [0.33333333, 0.66666667, 0.33330338],
```

```python
    [0.33333333, 0.66666667, 0.83330296],
    [0.66666667, 0.33333333, 0.16663682],
    [0.66666667, 0.33333333, 0.66663629],
    [0.00000000, 0.00000000, 0.25073114],
    [0.00000000, 0.00000000, 0.75073128],
    [0.33333333, 0.66666667, 0.08406455],
    [0.33333333, 0.66666667, 0.58406469],
    [0.66666667, 0.33333333, 0.41739778],
    [0.66666667, 0.33333333, 0.91739778],
    [0.83481140, 0.66962279, 0.33237250],
    [0.83481140, 0.16518860, 0.33237250],
    [0.33037721, 0.16518860, 0.33237250],
    [0.83481116, 0.66962233, 0.83237248],
    [0.83481116, 0.16518884, 0.83237248],
    [0.33037767, 0.16518884, 0.83237248],
    [0.16814443, 0.33628886, 0.16570580],
    [0.16814443, 0.83185557, 0.16570580],
    [0.66371114, 0.83185557, 0.16570580],
    [0.16814367, 0.33628734, 0.66570579],
    [0.16814367, 0.83185633, 0.66570579],
    [0.66371266, 0.83185633, 0.66570579],
    [0.50147757, 1.00295513, 0.49903915],
    [0.50147757, 0.49852243, 0.49903915],
    [0.99704487, 0.49852243, 0.49903915],
    [0.50147799, 0.00295598, 0.99903917],
    [0.50147799, 0.49852201, 0.99903917],
    [0.99704402, 0.49852201, 0.99903917],
]

# --- Verify number of positions matches number of atomic lines ---
num_atoms = sum(1 for line in lines if line.strip().startswith("AT"))
assert len(new_positions) == num_atoms, (
    f"Number of new positions ({len(new_positions)}) does not match number of atoms ({num_atoms})"
)

# --- Replace atomic positions while preserving format ---
new_pos_index = 0
new_lines = []

for line in lines:
    if line.strip().startswith("AT"):
        new_pos = new_positions[new_pos_index]
        new_line = (
            f"AT {new_pos_index + 1:5d}: "
            f"X={new_pos[0]:.8f} Y={new_pos[1]:.8f} Z={new_pos[2]:.8f}\n"
        )
        new_pos_index += 1
    else:
        new_line = line  # Preserve non-atomic lines
    new_lines.append(new_line)

# --- Write updated structure to new file ---
with open("new_structure.struct", "w") as f:
    f.writelines(new_lines)

print("Successfully wrote new structure to 'new_structure.struct'")
```

Listing 1. Python Script for Updating Atomic Positions.

This scripting framework was integrated into the overall workflow for automated structural interpolation, ensuring that each intermediate configuration is generated with consistent atomic ordering, high numerical precision, and complete traceability. By embedding this procedure into the broader ferroelectric analysis pipeline, the evolution of ionic displacements, polarization, and electronic structure can be followed seamlessly along the switching coordinate, enabling a fully reproducible mapping of the energy landscape.

Reference structure. To anchor the interpolation scheme, we adopt a fixed WIEN2k `.struct` template as the reference geometry for generating the switching pathway. The listing below provides a representative $CsGeCl_3$ file; only the `AT`-prefixed fractional coordinates are updated by the Python routine in Listing 1 to realize prescribed values of the collective coordinate $\lambda \in [0, 1]$. All non-atomic metadata (cell parameters, species blocks, muffin–tin radii, and local rotation matrices) are preserved verbatim to ensure strict reproducibility and seamless compatibility with downstream calculations. Consequently, variations in total energy, polarization, and electronic structure reflect solely the intended ionic displacements along the ferroelectric path.

```
octavetmp
H                            30    1P1
MODE OF CALC=RELA unit=bohr
 14.683000 14.683000 36.528200 90.000000 90.000000120.000000
AT    -1: X=0.00000000 Y=0.00000000 Z=0.49969827
          M     1          ISPLIT= 8
Cs1        NPT=  781  R0=.000010000 RMT=   2.50000   Z:  55.00000
LOCAL ROT MATRIX:    1.0000000 0.0000000 0.0000000
                     0.0000000 1.0000000 0.0000000
                     0.0000000 0.0000000 1.0000000
AT    -2: X=0.00000000 Y=0.00000000 Z=0.99969827
          M     1          ISPLIT= 8
Cs2        NPT=  781  R0=.000010000 RMT=   2.50000   Z:  55.00000
LOCAL ROT MATRIX:    1.0000000 0.0000000 0.0000000
                     0.0000000 1.0000000 0.0000000
                     0.0000000 0.0000000 1.0000000
AT    -3: X=0.33333333 Y=0.66666667 Z=0.33303161
          M     1          ISPLIT= 8
Cs3        NPT=  781  R0=.000010000 RMT=   2.50000   Z:  55.00000
LOCAL ROT MATRIX:    1.0000000 0.0000000 0.0000000
                     0.0000000 1.0000000 0.0000000
                     0.0000000 0.0000000 1.0000000
AT    -4: X=0.33333333 Y=0.66666667 Z=0.83303160
          M     1          ISPLIT= 8
Cs4        NPT=  781  R0=.000010000 RMT=   2.50000   Z:  55.00000
LOCAL ROT MATRIX:    1.0000000 0.0000000 0.0000000
                     0.0000000 1.0000000 0.0000000
                     0.0000000 0.0000000 1.0000000
AT    -5: X=0.66666667 Y=0.33333333 Z=0.16636493
          M     1          ISPLIT= 8
Cs5        NPT=  781  R0=.000010000 RMT=   2.50000   Z:  55.00000
LOCAL ROT MATRIX:    1.0000000 0.0000000 0.0000000
                     0.0000000 1.0000000 0.0000000
                     0.0000000 0.0000000 1.0000000
AT    -6: X=0.66666667 Y=0.33333333 Z=0.66636494
          M     1          ISPLIT= 8
Cs6        NPT=  781  R0=.000010000 RMT=   2.50000   Z:  55.00000
LOCAL ROT MATRIX:    1.0000000 0.0000000 0.0000000
                     0.0000000 1.0000000 0.0000000
                     0.0000000 0.0000000 1.0000000
AT    -7: X=0.00000000 Y=0.00000000 Z=0.25731219
          M     1          ISPLIT= 8
Ge         NPT=  781  R0=.000050000 RMT=   2.38000   Z:  32.00000
LOCAL ROT MATRIX:    1.0000000 0.0000000 0.0000000
                     0.0000000 1.0000000 0.0000000
                     0.0000000 0.0000000 1.0000000
AT    -8: X=0.00000000 Y=0.00000000 Z=0.75731219
          M     1          ISPLIT= 8
Ge         NPT=  781  R0=.000050000 RMT=   2.38000   Z:  32.00000
LOCAL ROT MATRIX:    1.0000000 0.0000000 0.0000000
                     0.0000000 1.0000000 0.0000000
                     0.0000000 0.0000000 1.0000000
AT    -9: X=0.33333333 Y=0.66666667 Z=0.09064553
          M     1          ISPLIT= 8
Ge         NPT=  781  R0=.000050000 RMT=   2.38000   Z:  32.00000
LOCAL ROT MATRIX:    1.0000000 0.0000000 0.0000000
                     0.0000000 1.0000000 0.0000000
                     0.0000000 0.0000000 1.0000000
AT   -10: X=0.33333333 Y=0.66666667 Z=0.59064553
          M     1          ISPLIT= 8
Ge         NPT=  781  R0=.000050000 RMT=   2.38000   Z:  32.00000
LOCAL ROT MATRIX:    1.0000000 0.0000000 0.0000000
                     0.0000000 1.0000000 0.0000000
                     0.0000000 0.0000000 1.0000000
AT   -11: X=0.66666667 Y=0.33333333 Z=0.42397885
          M     1          ISPLIT= 8
Ge         NPT=  781  R0=.000050000 RMT=   2.38000   Z:  32.00000
```

```
LOCAL ROT MATRIX:    1.0000000 0.0000000 0.0000000
                     0.0000000 1.0000000 0.0000000
                     0.0000000 0.0000000 1.0000000
AT   -12: X=0.66666667 Y=0.33333333 Z=0.92397885
          M     1          ISPLIT= 8
Ge         NPT=  781  R0=.000050000 RMT=   2.38000   Z:  32.00000
LOCAL ROT MATRIX:    1.0000000 0.0000000 0.0000000
                     0.0000000 1.0000000 0.0000000
                     0.0000000 0.0000000 1.0000000
AT   -13: X=0.84810911 Y=0.69621821 Z=0.32372484
          M     1          ISPLIT= 8
Cl         NPT=  781  R0=.000100000 RMT=   2.15000   Z:  17.00000
LOCAL ROT MATRIX:    1.0000000 0.0000000 0.0000000
                     0.0000000 1.0000000 0.0000000
                     0.0000000 0.0000000 1.0000000
AT   -14: X=0.84810911 Y=0.15189089 Z=0.32372484
          M     1          ISPLIT= 8
Cl         NPT=  781  R0=.000100000 RMT=   2.15000   Z:  17.00000
LOCAL ROT MATRIX:    1.0000000 0.0000000 0.0000000
                     0.0000000 1.0000000 0.0000000
                     0.0000000 0.0000000 1.0000000
AT   -15: X=0.30378179 Y=0.15189089 Z=0.32372484
          M     1          ISPLIT= 8
Cl         NPT=  781  R0=.000100000 RMT=   2.15000   Z:  17.00000
LOCAL ROT MATRIX:    1.0000000 0.0000000 0.0000000
                     0.0000000 1.0000000 0.0000000
                     0.0000000 0.0000000 1.0000000
AT   -16: X=0.84810911 Y=0.69621821 Z=0.82372484
          M     1          ISPLIT= 8
Cl         NPT=  781  R0=.000100000 RMT=   2.15000   Z:  17.00000
LOCAL ROT MATRIX:    1.0000000 0.0000000 0.0000000
                     0.0000000 1.0000000 0.0000000
                     0.0000000 0.0000000 1.0000000
AT   -17: X=0.84810911 Y=0.15189089 Z=0.82372484
          M     1          ISPLIT= 8
Cl         NPT=  781  R0=.000100000 RMT=   2.15000   Z:  17.00000
LOCAL ROT MATRIX:    1.0000000 0.0000000 0.0000000
                     0.0000000 1.0000000 0.0000000
                     0.0000000 0.0000000 1.0000000
AT   -18: X=0.30378179 Y=0.15189089 Z=0.82372484
          M     1          ISPLIT= 8
Cl         NPT=  781  R0=.000100000 RMT=   2.15000   Z:  17.00000
LOCAL ROT MATRIX:    1.0000000 0.0000000 0.0000000
                     0.0000000 1.0000000 0.0000000
                     0.0000000 0.0000000 1.0000000
AT   -19: X=0.18144244 Y=0.36288488 Z=0.15705818
          M     1          ISPLIT= 8
Cl         NPT=  781  R0=.000100000 RMT=   2.15000   Z:  17.00000
LOCAL ROT MATRIX:    1.0000000 0.0000000 0.0000000
                     0.0000000 1.0000000 0.0000000
                     0.0000000 0.0000000 1.0000000
AT   -20: X=0.18144244 Y=0.81855756 Z=0.15705818
          M     1          ISPLIT= 8
Cl         NPT=  781  R0=.000100000 RMT=   2.15000   Z:  17.00000
LOCAL ROT MATRIX:    1.0000000 0.0000000 0.0000000
                     0.0000000 1.0000000 0.0000000
                     0.0000000 0.0000000 1.0000000
AT   -21: X=0.63711512 Y=0.81855756 Z=0.15705818
          M     1          ISPLIT= 8
Cl         NPT=  781  R0=.000100000 RMT=   2.15000   Z:  17.00000
LOCAL ROT MATRIX:    1.0000000 0.0000000 0.0000000
                     0.0000000 1.0000000 0.0000000
                     0.0000000 0.0000000 1.0000000
AT   -22: X=0.18144244 Y=0.36288488 Z=0.65705818
          M     1          ISPLIT= 8
Cl         NPT=  781  R0=.000100000 RMT=   2.15000   Z:  17.00000
LOCAL ROT MATRIX:    1.0000000 0.0000000 0.0000000
                     0.0000000 1.0000000 0.0000000
                     0.0000000 0.0000000 1.0000000
AT   -23: X=0.18144244 Y=0.81855756 Z=0.65705818
```

```
          M     1          ISPLIT= 8
Cl         NPT=  781  R0=.000100000 RMT=   2.15000   Z:  17.00000
LOCAL ROT MATRIX:    1.0000000 0.0000000 0.0000000
                     0.0000000 1.0000000 0.0000000
                     0.0000000 0.0000000 1.0000000
AT   -24: X=0.63711512 Y=0.81855756 Z=0.65705818
          M     1          ISPLIT= 8
Cl         NPT=  781  R0=.000100000 RMT=   2.15000   Z:  17.00000
LOCAL ROT MATRIX:    1.0000000 0.0000000 0.0000000
                     0.0000000 1.0000000 0.0000000
                     0.0000000 0.0000000 1.0000000
AT   -25: X=0.51477577 Y=0.02955155 Z=0.49039152
          M     1          ISPLIT= 8
Cl         NPT=  781  R0=.000100000 RMT=   2.15000   Z:  17.00000
LOCAL ROT MATRIX:    1.0000000 0.0000000 0.0000000
                     0.0000000 1.0000000 0.0000000
                     0.0000000 0.0000000 1.0000000
AT   -26: X=0.51477577 Y=0.48522423 Z=0.49039152
          M     1          ISPLIT= 8
Cl         NPT=  781  R0=.000100000 RMT=   2.15000   Z:  17.00000
LOCAL ROT MATRIX:    1.0000000 0.0000000 0.0000000
                     0.0000000 1.0000000 0.0000000
                     0.0000000 0.0000000 1.0000000
AT   -27: X=0.97044845 Y=0.48522423 Z=0.49039152
          M     1          ISPLIT= 8
Cl         NPT=  781  R0=.000100000 RMT=   2.15000   Z:  17.00000
LOCAL ROT MATRIX:    1.0000000 0.0000000 0.0000000
                     0.0000000 1.0000000 0.0000000
                     0.0000000 0.0000000 1.0000000
AT   -28: X=0.51477577 Y=0.02955155 Z=0.99039152
          M     1          ISPLIT= 8
Cl         NPT=  781  R0=.000100000 RMT=   2.15000   Z:  17.00000
LOCAL ROT MATRIX:    1.0000000 0.0000000 0.0000000
                     0.0000000 1.0000000 0.0000000
                     0.0000000 0.0000000 1.0000000
AT   -29: X=0.51477577 Y=0.48522423 Z=0.99039152
          M     1          ISPLIT= 8
Cl         NPT=  781  R0=.000100000 RMT=   2.15000   Z:  17.00000
LOCAL ROT MATRIX:    1.0000000 0.0000000 0.0000000
                     0.0000000 1.0000000 0.0000000
                     0.0000000 0.0000000 1.0000000
AT   -30: X=0.97044845 Y=0.48522423 Z=0.99039152
          M     1          ISPLIT= 8
Cl         NPT=  781  R0=.000100000 RMT=   2.15000   Z:  17.00000
LOCAL ROT MATRIX:    1.0000000 0.0000000 0.0000000
                     0.0000000 1.0000000 0.0000000
                     0.0000000 0.0000000 1.0000000
   0      NUMBER OF SYMMETRY OPERATIONS
```

Listing 2. WIEN2k structure file for $CsGeCl_3$, as the input file, i.e., `original_structure.struct`, for the Python Script for Updating Atomic Positions.

Output structure. The file below is the direct product of the Python routine in Listing 1, written as `new_structure.struct` for a chosen interpolation step λ. Only the `AT` records are modified: atomic entries are renumbered consecutively $(1, 2, \dots)$, the fractional coordinates are updated to eight decimal places, and the original ordering is preserved. All non-atomic metadata (cell parameters, species blocks, muffin–tin radii, and local rotation matrices) remain unchanged to ensure strict reproducibility and compatibility with downstream WIEN2k calculations. Note that fractional components may fall slightly outside $[0, 1)$ near periodic boundaries (e.g., $y > 1$); WIEN2k interprets these modulo the lattice, but optional wrapping to $[0, 1)$ can be applied post hoc without affecting the physical results.

```
octavetmp
H                          30    1P1
MODE OF CALC=RELA unit=bohr
 14.683000 14.683000 36.528200 90.000000 90.000000120.000000
AT     1: X=0.00000000 Y=0.00000000 Z=0.49996977
          M     1          ISPLIT= 8
Cs1        NPT=  781  R0=.000010000 RMT=   2.50000   Z:  55.00000
LOCAL ROT MATRIX:    1.0000000 0.0000000 0.0000000
                     0.0000000 1.0000000 0.0000000
                     0.0000000 0.0000000 1.0000000
```

```
AT     2: X=0.00000000 Y=0.00000000 Z=0.99996986
          M     1          ISPLIT= 8
Cs2        NPT=  781  R0=.000010000 RMT=   2.50000   Z:  55.00000
LOCAL ROT MATRIX:    1.0000000 0.0000000 0.0000000
                     0.0000000 1.0000000 0.0000000
                     0.0000000 0.0000000 1.0000000
AT     3: X=0.33333333 Y=0.66666667 Z=0.33330338
          M     1          ISPLIT= 8
Cs3        NPT=  781  R0=.000010000 RMT=   2.50000   Z:  55.00000
LOCAL ROT MATRIX:    1.0000000 0.0000000 0.0000000
                     0.0000000 1.0000000 0.0000000
                     0.0000000 0.0000000 1.0000000
AT     4: X=0.33333333 Y=0.66666667 Z=0.83330296
          M     1          ISPLIT= 8
Cs4        NPT=  781  R0=.000010000 RMT=   2.50000   Z:  55.00000
LOCAL ROT MATRIX:    1.0000000 0.0000000 0.0000000
                     0.0000000 1.0000000 0.0000000
                     0.0000000 0.0000000 1.0000000
AT     5: X=0.66666667 Y=0.33333333 Z=0.16663682
          M     1          ISPLIT= 8
Cs5        NPT=  781  R0=.000010000 RMT=   2.50000   Z:  55.00000
LOCAL ROT MATRIX:    1.0000000 0.0000000 0.0000000
                     0.0000000 1.0000000 0.0000000
                     0.0000000 0.0000000 1.0000000
AT     6: X=0.66666667 Y=0.33333333 Z=0.66663629
          M     1          ISPLIT= 8
Cs6        NPT=  781  R0=.000010000 RMT=   2.50000   Z:  55.00000
LOCAL ROT MATRIX:    1.0000000 0.0000000 0.0000000
                     0.0000000 1.0000000 0.0000000
                     0.0000000 0.0000000 1.0000000
AT     7: X=0.00000000 Y=0.00000000 Z=0.25073114
          M     1          ISPLIT= 8
Ge         NPT=  781  R0=.000050000 RMT=   2.38000   Z:  32.00000
LOCAL ROT MATRIX:    1.0000000 0.0000000 0.0000000
                     0.0000000 1.0000000 0.0000000
                     0.0000000 0.0000000 1.0000000
AT     8: X=0.00000000 Y=0.00000000 Z=0.75073128
          M     1          ISPLIT= 8
Ge         NPT=  781  R0=.000050000 RMT=   2.38000   Z:  32.00000
LOCAL ROT MATRIX:    1.0000000 0.0000000 0.0000000
                     0.0000000 1.0000000 0.0000000
                     0.0000000 0.0000000 1.0000000
AT     9: X=0.33333333 Y=0.66666667 Z=0.08406455
          M     1          ISPLIT= 8
Ge         NPT=  781  R0=.000050000 RMT=   2.38000   Z:  32.00000
LOCAL ROT MATRIX:    1.0000000 0.0000000 0.0000000
                     0.0000000 1.0000000 0.0000000
                     0.0000000 0.0000000 1.0000000
AT    10: X=0.33333333 Y=0.66666667 Z=0.58406469
          M     1          ISPLIT= 8
Ge         NPT=  781  R0=.000050000 RMT=   2.38000   Z:  32.00000
LOCAL ROT MATRIX:    1.0000000 0.0000000 0.0000000
                     0.0000000 1.0000000 0.0000000
                     0.0000000 0.0000000 1.0000000
AT    11: X=0.66666667 Y=0.33333333 Z=0.41739778
          M     1          ISPLIT= 8
Ge         NPT=  781  R0=.000050000 RMT=   2.38000   Z:  32.00000
LOCAL ROT MATRIX:    1.0000000 0.0000000 0.0000000
                     0.0000000 1.0000000 0.0000000
                     0.0000000 0.0000000 1.0000000
AT    12: X=0.66666667 Y=0.33333333 Z=0.91739778
          M     1          ISPLIT= 8
Ge         NPT=  781  R0=.000050000 RMT=   2.38000   Z:  32.00000
LOCAL ROT MATRIX:    1.0000000 0.0000000 0.0000000
                     0.0000000 1.0000000 0.0000000
                     0.0000000 0.0000000 1.0000000
AT    13: X=0.83481140 Y=0.66962279 Z=0.33237250
          M     1          ISPLIT= 8
Cl         NPT=  781  R0=.000100000 RMT=   2.15000   Z:  17.00000
LOCAL ROT MATRIX:    1.0000000 0.0000000 0.0000000
```

```
                     0.0000000 1.0000000 0.0000000
                     0.0000000 0.0000000 1.0000000
AT    14: X=0.83481140 Y=0.16518860 Z=0.33237250
          M     1          ISPLIT= 8
Cl         NPT=  781  R0=.000100000 RMT=   2.15000   Z:  17.00000
LOCAL ROT MATRIX:    1.0000000 0.0000000 0.0000000
                     0.0000000 1.0000000 0.0000000
                     0.0000000 0.0000000 1.0000000
AT    15: X=0.33037721 Y=0.16518860 Z=0.33237250
          M     1          ISPLIT= 8
Cl         NPT=  781  R0=.000100000 RMT=   2.15000   Z:  17.00000
LOCAL ROT MATRIX:    1.0000000 0.0000000 0.0000000
                     0.0000000 1.0000000 0.0000000
                     0.0000000 0.0000000 1.0000000
AT    16: X=0.83481116 Y=0.66962233 Z=0.83237248
          M     1          ISPLIT= 8
Cl         NPT=  781  R0=.000100000 RMT=   2.15000   Z:  17.00000
LOCAL ROT MATRIX:    1.0000000 0.0000000 0.0000000
                     0.0000000 1.0000000 0.0000000
                     0.0000000 0.0000000 1.0000000
AT    17: X=0.83481116 Y=0.16518884 Z=0.83237248
          M     1          ISPLIT= 8
Cl         NPT=  781  R0=.000100000 RMT=   2.15000   Z:  17.00000
LOCAL ROT MATRIX:    1.0000000 0.0000000 0.0000000
                     0.0000000 1.0000000 0.0000000
                     0.0000000 0.0000000 1.0000000
AT    18: X=0.33037767 Y=0.16518884 Z=0.83237248
          M     1          ISPLIT= 8
Cl         NPT=  781  R0=.000100000 RMT=   2.15000   Z:  17.00000
LOCAL ROT MATRIX:    1.0000000 0.0000000 0.0000000
                     0.0000000 1.0000000 0.0000000
                     0.0000000 0.0000000 1.0000000
AT    19: X=0.16814443 Y=0.33628886 Z=0.16570580
          M     1          ISPLIT= 8
Cl         NPT=  781  R0=.000100000 RMT=   2.15000   Z:  17.00000
LOCAL ROT MATRIX:    1.0000000 0.0000000 0.0000000
                     0.0000000 1.0000000 0.0000000
                     0.0000000 0.0000000 1.0000000
AT    20: X=0.16814443 Y=0.83185557 Z=0.16570580
          M     1          ISPLIT= 8
Cl         NPT=  781  R0=.000100000 RMT=   2.15000   Z:  17.00000
LOCAL ROT MATRIX:    1.0000000 0.0000000 0.0000000
                     0.0000000 1.0000000 0.0000000
                     0.0000000 0.0000000 1.0000000
AT    21: X=0.66371114 Y=0.83185557 Z=0.16570580
          M     1          ISPLIT= 8
Cl         NPT=  781  R0=.000100000 RMT=   2.15000   Z:  17.00000
LOCAL ROT MATRIX:    1.0000000 0.0000000 0.0000000
                     0.0000000 1.0000000 0.0000000
                     0.0000000 0.0000000 1.0000000
AT    22: X=0.16814367 Y=0.33628734 Z=0.66570579
          M     1          ISPLIT= 8
Cl         NPT=  781  R0=.000100000 RMT=   2.15000   Z:  17.00000
LOCAL ROT MATRIX:    1.0000000 0.0000000 0.0000000
                     0.0000000 1.0000000 0.0000000
                     0.0000000 0.0000000 1.0000000
AT    23: X=0.16814367 Y=0.83185633 Z=0.66570579
          M     1          ISPLIT= 8
Cl         NPT=  781  R0=.000100000 RMT=   2.15000   Z:  17.00000
LOCAL ROT MATRIX:    1.0000000 0.0000000 0.0000000
                     0.0000000 1.0000000 0.0000000
                     0.0000000 0.0000000 1.0000000
AT    24: X=0.66371266 Y=0.83185633 Z=0.66570579
          M     1          ISPLIT= 8
Cl         NPT=  781  R0=.000100000 RMT=   2.15000   Z:  17.00000
LOCAL ROT MATRIX:    1.0000000 0.0000000 0.0000000
                     0.0000000 1.0000000 0.0000000
                     0.0000000 0.0000000 1.0000000
AT    25: X=0.50147757 Y=1.00295513 Z=0.49903915
          M     1          ISPLIT= 8
```

```
Cl         NPT=  781  R0=.000100000 RMT=   2.15000   Z:  17.00000
LOCAL ROT MATRIX:    1.0000000 0.0000000 0.0000000
                     0.0000000 1.0000000 0.0000000
                     0.0000000 0.0000000 1.0000000
AT    26: X=0.50147757 Y=0.49852243 Z=0.49903915
          M     1          ISPLIT= 8
Cl         NPT=  781  R0=.000100000 RMT=   2.15000   Z:  17.00000
LOCAL ROT MATRIX:    1.0000000 0.0000000 0.0000000
                     0.0000000 1.0000000 0.0000000
                     0.0000000 0.0000000 1.0000000
AT    27: X=0.99704487 Y=0.49852243 Z=0.49903915
          M     1          ISPLIT= 8
Cl         NPT=  781  R0=.000100000 RMT=   2.15000   Z:  17.00000
LOCAL ROT MATRIX:    1.0000000 0.0000000 0.0000000
                     0.0000000 1.0000000 0.0000000
                     0.0000000 0.0000000 1.0000000
AT    28: X=0.50147799 Y=0.00295598 Z=0.99903917
          M     1          ISPLIT= 8
Cl         NPT=  781  R0=.000100000 RMT=   2.15000   Z:  17.00000
LOCAL ROT MATRIX:    1.0000000 0.0000000 0.0000000
                     0.0000000 1.0000000 0.0000000
                     0.0000000 0.0000000 1.0000000
AT    29: X=0.50147799 Y=0.49852201 Z=0.99903917
          M     1          ISPLIT= 8
Cl         NPT=  781  R0=.000100000 RMT=   2.15000   Z:  17.00000
LOCAL ROT MATRIX:    1.0000000 0.0000000 0.0000000
                     0.0000000 1.0000000 0.0000000
                     0.0000000 0.0000000 1.0000000
AT    30: X=0.99704402 Y=0.49852201 Z=0.99903917
          M     1          ISPLIT= 8
Cl         NPT=  781  R0=.000100000 RMT=   2.15000   Z:  17.00000
LOCAL ROT MATRIX:    1.0000000 0.0000000 0.0000000
                     0.0000000 1.0000000 0.0000000
                     0.0000000 0.0000000 1.0000000
   0      NUMBER OF SYMMETRY OPERATIONS
```

Listing 3. WIEN2k structure file for $CsGeCl_3$, as the output file, i.e., `new_structure.struct`, of the Python Script for Updating Atomic Positions.

SM7. PYTHON-BASED ELF IMAGE PROCESSING PIPELINE

The electron localization function (ELF) offers a powerful real-space descriptor of bonding and electronic localization, directly linking the distribution of valence electrons to stereochemical lone-pair activity and ferroelectric distortion. In the $CsGeX_3$ halide perovskites, where ferroelectricity emerges from the asymmetric hybridization of Ge $4s^2$ and X p orbitals, the ELF provides a direct visualization of the nonbonding charge density that drives lattice polarization. To extract these features quantitatively, we developed a fully automated Python-based image processing pipeline (Listing 4), which complements the Berry-phase polarization framework described in Sec. SM6. Together, these analyses establish a unified structure–electronic correlation between local charge asymmetry, lattice instability, and macroscopic polarization.

High-resolution ELF isosurfaces, computed via WIEN2k and exported as two-dimensional color maps, serve as the input data for the Python workflow. Using the OpenCV computer-vision library, the pipeline performs (i) image import and color-space conversion, (ii) color-based segmentation of lone-pair-rich regions, (iii) morphological refinement to remove pixel-level noise, and (iv) statistical quantification of electron localization over distinct halide compositions.

First, the RGB ELF images are converted into both grayscale and HSV (Hue–Saturation–Value) color representations. The HSV mapping enables precise color-based isolation of the characteristic *purple* hue (Hue range $\sim$120–160°) that corresponds to strongly localized nonbonding s^2 electron density around the Ge centers. A binary mask is generated within this hue window using the `cv2.inRange()` function, effectively isolating regions of high localization probability. Morphological "opening" (erosion followed by dilation) with a 3×3 kernel is then applied to remove scattered noise and to refine the shape of contiguous ELF domains, ensuring that only physically significant lone-pair regions are retained for analysis.

Following refinement, the image is automatically partitioned into three equal-width vertical segments, corresponding to the $CsGeCl_3$, $CsGeBr_3$, and $CsGeI_3$ subdomains. Within each segment, two key quantities are evaluated: (i) the total lone-pair ELF area (A_{lp}) and (ii) the total ELF-active area (A_{ELF}). These areas are used to define a normalized localization index,

$$\eta_{lp} = \frac{A_{lp}}{A_{ELF}}, \tag{SM2}$$

which provides a dimensionless metric of the degree of lone-pair localization. The parameter η_{lp} quantitatively captures the relative contribution of stereochemically active lone pairs to the overall electron localization landscape. High η_{lp} values indicate stronger charge anisotropy and enhanced off-centering tendencies of Ge, directly correlating with increased ferroelectric polarization and reduced dielectric screening.

In the present analysis, $CsGeCl_3$ exhibits the largest η_{lp}, consistent with its pronounced Ge–Cl covalency and stronger s–p rehybridization that amplifies the local dipole moment. In contrast, $CsGeI_3$ shows the smallest η_{lp}, reflecting its softer, more ionic bonding character and enhanced electronic screening due to the highly polarizable I^- anions. This compositional trend mirrors the evolution of polarization and exciton binding energies observed in Secs. SM2 and SM3, confirming the intimate coupling between lone-pair localization, dielectric response, and optoelectronic confinement.

The computed η_{lp} values are consolidated into a structured `pandas` DataFrame for tabular output and statistical comparison. This automated analysis framework ensures reproducibility and removes the subjective bias inherent in manual region selection, allowing consistent quantification of ELF-derived lone-pair activity across the halide series. In essence, the Python-based ELF pipeline translates complex real-space electronic textures into interpretable, quantitative descriptors of ferroelectric and optoelectronic functionality, bridging atomistic electron localization with macroscopic polarization behavior in lead-free halide perovskites.

```python
# Import necessary libraries
import cv2  # OpenCV for image processing
import numpy as np  # NumPy for numerical computations
import pandas as pd  # Pandas for tabular data representation

# Load the input image
image_path = "image.png"  # Path to the ELF image
image = cv2.imread(image_path)  # Read the image using OpenCV

# Convert the image to grayscale for further processing
image_gray = cv2.cvtColor(image, cv2.COLOR_BGR2GRAY)  # Convert from BGR to grayscale

# Convert the image to HSV format for color-based segmentation
image_hsv = cv2.cvtColor(image, cv2.COLOR_BGR2HSV)  # Convert from BGR to HSV

# Define HSV range for detecting purple ELF regions
# Purple in HSV has a Hue (H) around 120-160, with moderate Saturation (S) and Value (V)
lower_purple = np.array([120, 50, 50])  # Lower bound for purple
upper_purple = np.array([160, 255, 255])  # Upper bound for purple

# Create a binary mask to isolate the purple ELF regions
mask_purple = cv2.inRange(image_hsv, lower_purple, upper_purple)  # Threshold the image

# Apply morphological operations to refine the ELF mask
# "Opening" (erosion followed by dilation) removes small noise
kernel = np.ones((3,3), np.uint8)  # Define a small kernel for morphology
mask_purple = cv2.morphologyEx(mask_purple, cv2.MORPH_OPEN, kernel)  # Apply morphological opening

# Extract ELF values by applying the mask on the grayscale image
elf_lone_pair_values = cv2.bitwise_and(image_gray, image_gray, mask=mask_purple)

# Get the dimensions of the image
height, width = image_gray.shape  # Extract image height and width
third_width = width // 3  # Divide the width into three equal parts for segmentation

# Segment the three regions corresponding to different CsGeX$_3$ compounds
region_a_lone = elf_lone_pair_values[:, :third_width]  # Left segment for CsGeCl$_3$
region_b_lone = elf_lone_pair_values[:, third_width:2*third_width]  # Center segment for CsGeBr$_3$
region_c_lone = elf_lone_pair_values[:, 2*third_width:]  # Right segment for CsGeI$_3$

# Compute ELF area for lone pairs by counting non-zero pixels in each region
elf_lone_area_a = np.count_nonzero(region_a_lone)  # Lone pair ELF in CsGeCl$_3$
elf_lone_area_b = np.count_nonzero(region_b_lone)  # Lone pair ELF in CsGeBr$_3$
elf_lone_area_c = np.count_nonzero(region_c_lone)  # Lone pair ELF in CsGeI$_3$

# Compute total ELF area in each region (for normalization)
elf_area_a = np.count_nonzero(image_gray[:, :third_width])  # Total ELF in CsGeCl$_3$
elf_area_b = np.count_nonzero(image_gray[:, third_width:2*third_width])  # Total ELF in CsGeBr$_3$
elf_area_c = np.count_nonzero(image_gray[:, 2*third_width:])  # Total ELF in CsGeI$_3$

# Normalize the ELF values within the targeted lone pair region for each compound
# This step ensures that ELF values are compared as a fraction of the total ELF in each region
```

```python
normalized_lone_elf_a = elf_lone_area_a / elf_area_a  # Normalized ELF for CsGeCl$_3$
normalized_lone_elf_b = elf_lone_area_b / elf_area_b  # Normalized ELF for CsGeBr$_3$
normalized_lone_elf_c = elf_lone_area_c / elf_area_c  # Normalized ELF for CsGeI$_3$

# Store the results in a dictionary for tabular representation
lone_elf_results = {
    "CsGeCl3 (a)": [elf_lone_area_a, normalized_lone_elf_a],
    "CsGeBr3 (b)": [elf_lone_area_b, normalized_lone_elf_b],
    "CsGeI3 (c)": [elf_lone_area_c, normalized_lone_elf_c],
}

# Convert the results into a Pandas DataFrame for better visualization
lone_elf_df = pd.DataFrame.from_dict(lone_elf_results, orient='index',
                                     columns=["Lone Pair ELF Area (pixels)", "Normalized Lone Pair ELF"])

# Display the final computed ELF values
print(lone_elf_df)
```

Listing 4. Complete Python Script for ELF Analysis.

This Python-based ELF analysis pipeline provides a transparent, reproducible, and extensible framework for correlating real-space electron localization with macroscopic ferroelectric behavior. By integrating image segmentation, morphological analysis, and data normalization into a single automated routine, it enables a quantitative connection between lone-pair stereochemical activity and the emergent polarization phenomena in lead-free halide perovskites.

SM8. THEORY AND METHODS

To characterize the optoelectronic and ferroic properties of halide perovskites, we employ three complementary first-principles approaches. Optical excitations are treated using MBPT via the green's function (GW) approximation [8, 9] and Bethe–Salpeter equation (BSE) [10–13], as detailed in Sec. SM8 A, enabling accurate prediction of QP band gaps and excitonic effects. Ferroelectric polarization is quantified using the Berry phase (Bp) formalism in Sec. SM8 B, which accounts for both ionic displacements and electronic contributions. Finally, the ELF, introduced in Sec. SM8 D, is used to visualize bonding and identify regions of electron pairing or delocalization, providing insight into the chemical environment and hybridization.

A. Many-Body Perturbation Theory for Optical Excitations

To accurately describe the optical response of halide perovskites—semiconductors known for their pronounced excitonic effects, low dielectric screening, and localized electronic states—we adopt the framework of MBPT, combining the GW approximation with the BSE. This methodology systematically addresses the shortcomings of DFT, which, though adequate for ground-state energetics, fails to QP corrections and neutral excitations such as bound electron-hole pairs (excitons), which dominate the optical spectrum in these materials.

Fig. SM5 schematically summarizes the hierarchical progression of theoretical treatments. In the DFT + RPA (random phase approximation) level (left panel), optical excitations are modeled as vertical transitions between valence and conduction Kohn-Sham (KS) [14] states, ignoring both QP renormalization and Coulomb attraction between the excited electron and the hole. Consequently, this approximation yields underestimated band gaps and misses bound excitonic features. The DFT + G_0W_0 + RPA approach (middle panel) corrects single-particle energies using the self-energy operator $\Sigma = iGW$, replacing the local exchange-correlation potential V_{XC} with a nonlocal, energy-dependent form, where G is the single-particle Green's function and W the dynamically screened Coulomb interaction [8, 9, 15]. The corrected QP eigenvalues $\epsilon_{n\mathbf{k}}^{QP}$ are obtained self-consistently as [11]:

$$\epsilon_{n\mathbf{k}}^{QP} = \epsilon_{n\mathbf{k}}^{KS} + \langle \psi_{n\mathbf{k}} | \Sigma(\epsilon_{n\mathbf{k}}^{QP}) - V_{XC} | \psi_{n\mathbf{k}} \rangle, \tag{SM3}$$

where $\psi_{n\mathbf{k}}$ is the KS single-particle wavefunction for band index n and crystal momentum $\mathbf{k}$, obtained from a DFT calculation. This step produces a realistic electronic structure and improves the band gap, but still treats the excited electron and hole as uncorrelated particles. Only the full DFT + GW + BSE formalism (right panel of Fig. SM5) captures the key ingredient missing in lower levels of theory: the attractive interaction between the photoexcited electron and hole, giving rise to excitons—discrete bound states located below the QP band edge.

The BSE describes neutral excitations through a correlated two-particle wavefunction $|A_\lambda\rangle$ and its associated excitation energy E_λ, governed by the effective two-particle Hamiltonian [11, 16]:

$$H^{(\text{eff})} |A_\lambda\rangle = E_\lambda |A_\lambda\rangle, \tag{SM4}$$

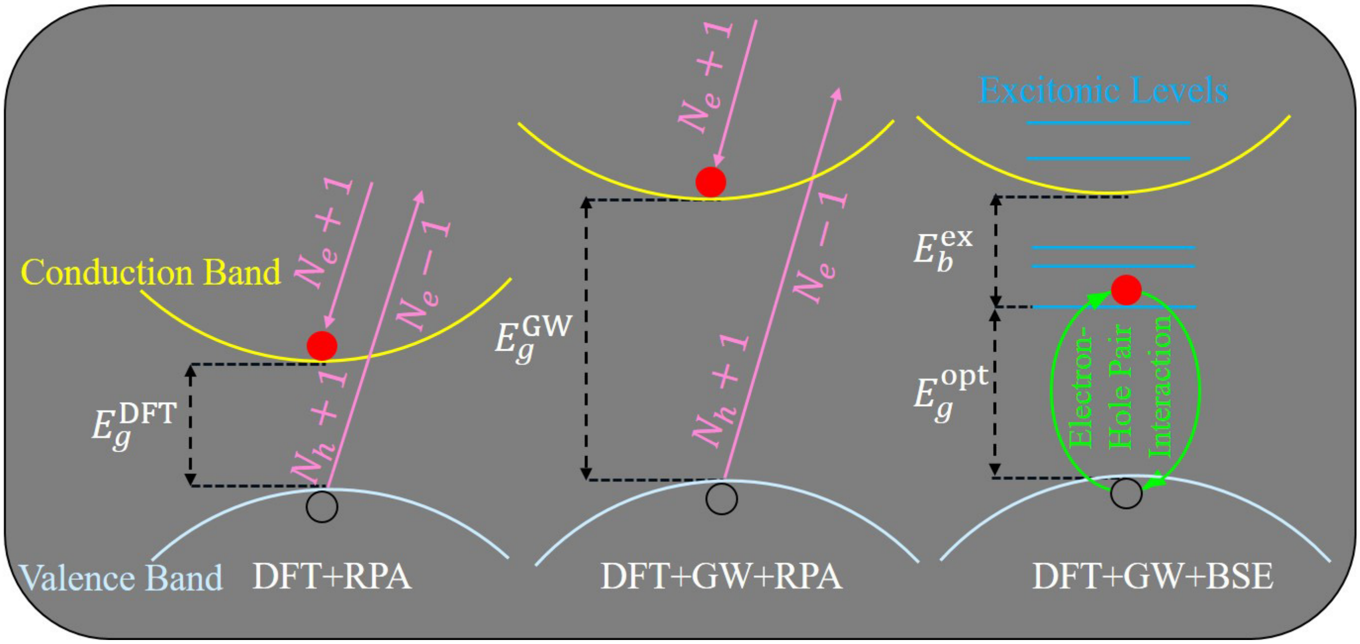

FIG. SM5. Hierarchical progression of theoretical treatments for optical excitations in solids, highlighting the role of many-body effects. The left panel (DFT + RPA) shows a simplified picture of vertical electronic transitions between valence and conduction bands without QP or excitonic corrections, capturing only independent-particle transitions. The middle panel (DFT + GW + RPA) introduces QP corrections via the G_0W_0 approximation, yielding more accurate electronic gaps but still neglecting electron-hole interactions. Only in the right panel (DFT + GW + BSE) is the screened Coulomb attraction between the excited electron and the hole explicitly included, resulting in the formation of bound excitonic states. This level of theory captures discrete absorption features below the QP band edge, as observed experimentally in low-screening materials such as halide perovskites. The diagram illustrates how each successive step adds essential physics: from electronic structure correction to electron-hole correlation, culminating in a quantitatively accurate and predictive description of the optical spectrum.

with the Hamiltonian decomposed as:

$$H^{(\mathrm{eff})} = H^{(\mathrm{diag})} + 2\gamma_{\mathrm{x}} H^{(\mathrm{x})} + \gamma_{\mathrm{c}} H^{(\mathrm{c})}. \tag{SM5}$$

The diagonal term $H^{(\mathrm{diag})}$ contains the QP transition energies between valence and conduction states:

$$H^{(\mathrm{diag})}_{\alpha\beta} = \left(\epsilon^{\mathrm{QP}}_{c_\alpha \mathbf{k}_\alpha} - \epsilon^{\mathrm{QP}}_{v_\alpha \mathbf{k}_\alpha}\right)\delta_{\alpha\beta}, \tag{SM6}$$

where α denotes a transition from valence band v_α to conduction band c_α at crystal momentum $\mathbf{k}_\alpha$, and the Kronecker delta $\delta_{\alpha\beta}$ ensures diagonal coupling between identical transitions. The diagonal term $H^{(\mathrm{diag})}$ defines the fundamental excitation energies of non-interacting QPs, representing vertical transitions from valence to conduction bands in the absence of any electron-hole coupling. This forms the baseline of the Bethe–Salpeter Hamiltonian and corresponds to the so-called independent-particle (IP) approximation [11]. In this limit, the excited electron and the residual hole evolve as uncorrelated particles, and the resulting optical spectrum lacks any signature of many-body interactions, such as bound excitonic states. The BSE offers a hierarchy of approximations that progressively introduce electron-hole interactions, each revealing a distinct layer of physical insight. Starting from the IP limit with only $H^{(\mathrm{diag})}$ [17], the inclusion of the exchange interaction term $H^{(\mathrm{x})}$ introduces short-range electron-hole repulsion. This accounts for local-field effects and enforces the fermionic antisymmetry of the wavefunction, modifying the spatial character of excitations. When $H^{(\mathrm{x})}$ is present but the direct attraction $H^{(\mathrm{c})}$ is omitted, the resulting approximation is often associated with the RPA, which incorporates exchange-driven corrections but still omits excitonic binding [11]. Conversely, retaining only the screened direct term $H^{(\mathrm{c})}$ captures the long-range Coulomb attraction between the electron and hole—a central force driving exciton formation. This regime becomes particularly relevant for spin-triplet excitations, where the exchange interaction vanishes due to the Pauli exclusion principle. A full description of neutral excitations, however, requires the simultaneous inclusion of all three contributions: the single-particle energies ($H^{(\mathrm{diag})}$), the repulsive exchange ($H^{(\mathrm{x})}$), and the attractive screened interaction ($H^{(\mathrm{c})}$) [12]. This complete BSE formulation enables the emergence of correlated two-particle states—excitons—manifesting as discrete optical resonances below the QP gap. It is this many-body treatment that provides a quantitatively accurate and physically grounded prediction of optical spectra in materials exhibiting electron-hole pairs with significant correlation, such as halide perovskites and other low-dimensional semiconductors. In this work, we refer to “RPA” as the approximation including exchange ($H^{(\mathrm{x})}$) but excluding screened direct interaction ($H^{(\mathrm{c})}$), and reserve “BSE” for the full singlet formulation including all terms ($H^{(\mathrm{diag})}$, $H^{(\mathrm{x})}$, $H^{(\mathrm{c})}$). For details, see the last paragraph of page 20 through the first column of page 21 in Ref. [18].

The short-range exchange term $H^{(\mathrm{x})}_{\alpha\beta}$ arises from the bare Coulomb interaction and imposes the fermionic antisymmetry of the excitonic wavefunction. It is given by [11, 16]:

$$H^{(\mathrm{x})}_{\alpha\beta}(\mathbf{q}) = \iint \Phi^{(r)*}_{\alpha}(\mathbf{r}_e, \mathbf{r}_e)\, v(\mathbf{r}_e, \mathbf{r}_h)\, \Phi^{(r)}_{\beta}(\mathbf{r}_h, \mathbf{r}_h)\, d^3r_e\, d^3r_h, \tag{SM7}$$

where $v(\mathbf{r}_e, \mathbf{r}_h) = 1/|\mathbf{r}_e - \mathbf{r}_h|$ is the bare Coulomb potential between an electron at $\mathbf{r}_e$ and a hole at $\mathbf{r}_h$; $\Phi^{(r)*}_{\alpha}(\mathbf{r}_e, \mathbf{r}_e)$ and $\Phi^{(r)}_{\beta}(\mathbf{r}_h, \mathbf{r}_h)$ are the complex conjugate and direct resonant two-particle wavefunctions, respectively, evaluated at coinciding electron and hole positions.

In contrast, the direct term $H^{(\mathrm{c})}$ encodes the long-range statically screened Coulomb attraction between the excited electron and the hole it leaves behind [11, 16]:

$$H^{(\mathrm{c})}_{\alpha\beta}(\mathbf{q}) = -\iint \Phi^{(r)*}_{\alpha}(\mathbf{r}_e, \mathbf{r}_h)\, W(\mathbf{r}_e, \mathbf{r}_h)\, \Phi^{(r)}_{\beta}(\mathbf{r}_e, \mathbf{r}_h)\, d^3r_e\, d^3r_h, \tag{SM8}$$

with the screened interaction defined as:

$$W(\mathbf{r}_e, \mathbf{r}_h) = \int v(\mathbf{r}_e, \mathbf{r})\, \varepsilon^{-1}(\mathbf{r}, \mathbf{r}_h)\, d^3r, \tag{SM9}$$

where ε^{-1} is the inverse dielectric function of the material, capturing its screening response; in Eq. (SM8), $\Phi^{(r)*}_{\alpha}(\mathbf{r}_e, \mathbf{r}_h)$ and $\Phi^{(r)}_{\beta}(\mathbf{r}_e, \mathbf{r}_h)$ are the complex conjugate and direct resonant two-particle wavefunctions, respectively, evaluated at distinct electron and hole positions $\mathbf{r}_e$ and $\mathbf{r}_h$.

The BSE Hamiltonian can be block-decomposed into resonant and anti-resonant sectors in the basis of two-particle electron–hole states, corresponding respectively to excitation and de-excitation processes. In this formalism, the total effective Hamiltonian is written as:

$$H^{(\mathrm{eff})} = \begin{pmatrix} H^{\mathrm{rr}} & H^{\mathrm{ra}} \\ H^{\mathrm{ar}} & H^{\mathrm{aa}} \end{pmatrix}, \tag{SM10}$$

where H^{rr} and H^{aa} describe the resonant (excitation) and anti-resonant (de-excitation) channels, while H^{ra} and H^{ar} encode the coupling between them. Each block contains contributions from the terms in the effective Hamiltonian defined in Eq. (SM5), such that all four blocks receive additive components from the diagonal QP energies $H^{(\mathrm{diag})}$, the short-range exchange term $H^{(\mathrm{x})}$, and the long-range screened direct term $H^{(\mathrm{c})}$. In particular, the off-diagonal couplings H^{ra} and H^{ar} arise from the same interaction kernels $H^{(\mathrm{x})}$ and $H^{(\mathrm{c})}$ that enter H^{rr} and H^{aa}, but couple resonant and anti-resonant configurations. Consequently, the choice to neglect H^{ra} and H^{ar} in the Tamm–Dancoff approximation (TDA) implies an approximation in the structure of the Hamiltonian—not the removal of interaction terms themselves [19]. The associated eigenvalue equation reads:

$$H^{(\mathrm{eff})} \begin{pmatrix} X^{\lambda} \\ Y^{\lambda} \end{pmatrix} = E_{\lambda} \begin{pmatrix} X^{\lambda} \\ Y^{\lambda} \end{pmatrix}, \tag{SM11}$$

where X^{λ} and Y^{λ} are the expansion coefficients of the excitonic wavefunction $|A_{\lambda}\rangle$ in the resonant and anti-resonant basis states, respectively. In this representation, each resonant basis function corresponds to the excitation of an electron from a valence band to a conduction band, described as a product of a valence state evaluated at crystal momentum $\mathbf{k}^{+}_{\alpha} = \mathbf{k}_{\alpha} + \mathbf{q}/2$ and a conduction state at $\mathbf{k}^{-}_{\alpha} = \mathbf{k}_{\alpha} - \mathbf{q}/2$ [19]. Specifically,

$$\Phi^{(\mathrm{r})}_{\alpha}(\mathbf{r}_e, \mathbf{r}_h) = \psi_{v_{\alpha}\mathbf{k}^{+}_{\alpha}}(\mathbf{r}_h)\, \psi^{*}_{c_{\alpha}\mathbf{k}^{-}_{\alpha}}(\mathbf{r}_e), \tag{SM12}$$

and the anti-resonant basis function, which corresponds to de-excitation, is given by the reversed product:

$$\Phi^{(\mathrm{a})}_{\alpha}(\mathbf{r}_e, \mathbf{r}_h) = \psi_{c_{\alpha}\mathbf{k}^{+}_{\alpha}}(\mathbf{r}_e)\, \psi^{*}_{v_{\alpha}\mathbf{k}^{-}_{\alpha}}(\mathbf{r}_h). \tag{SM13}$$

These functions represent the two-particle product states that form the basis of the BSE, where α indexes the electron-hole transition defined by $(v_{\alpha}, c_{\alpha}, \mathbf{k}_{\alpha})$. In the optical limit $\mathbf{q} = 0$, the transitions are vertical in momentum space and the same crystal momentum $\mathbf{k}_{\alpha}$ is used for both valence and conduction states. The resonant state $\Phi^{(\mathrm{r})}_{\alpha}$ corresponds to the excitation of an electron from a valence band to a conduction band, while the anti-resonant state $\Phi_\alpha^{(\mathrm{a})}$ represents the de-excitation process. These basis functions span the space in which the BSE Hamiltonian operates and define the structure of its resonant and anti-resonant sectors. To reduce computational cost, the TDA is often employed. This approximation neglects the off-diagonal coupling blocks H^{ra} and H^{ar}, and retains only the resonant–resonant block H^{rr}:

$$H_{\mathrm{TDA}}^{(\mathrm{eff})} = H^{\mathrm{rr}}. \tag{SM14}$$

This simplification is justified for optical absorption near the band edge, where the influence of the anti-resonant transitions is minimal. The TDA yields accurate exciton energies while significantly reducing the dimensionality and computational complexity of the BSE problem.

In the long-wavelength (optical) limit $\mathbf{q} \to 0$, the imaginary part of the macroscopic dielectric function governs the optical absorption and is computed from the BSE eigenstates as [11, 16]:

$$\begin{aligned} \Im[\varepsilon_M^{\mu\nu}(\omega)] = \frac{4\pi^2}{V}\sum_\lambda t_{\lambda,\mu}^* t_{\lambda,\nu}\frac{1}{\pi\delta}\Bigg(&\frac{\delta^2}{(\omega-E_\lambda)^2+\delta^2} \\ &-\frac{\delta^2}{(\omega+E_\lambda)^2+\delta^2}\Bigg), \end{aligned} \tag{SM15}$$

where V is the unit cell volume, δ is a phenomenological broadening parameter. The index λ labels the excitonic eigenstates of the BSE, and E_λ is the excitation energy associated with state λ. The Lorentzian lineshape in the parentheses represents the optical transition broadening centered at $\pm E_\lambda$, accounting for finite lifetimes and instrumental resolution. The dielectric tensor $\varepsilon_M^{\mu\nu}(\omega)$ describes the macroscopic optical response, with μ and ν denoting Cartesian components of the electric field and polarization directions, respectively. The dipole transition strength $t_{\lambda,\mu}$ in Cartesian direction μ is given by [11, 16]:

$$t_{\lambda,\mu} = i\sum_\alpha X_\alpha^\lambda \langle c_\alpha \mathbf{k}_\alpha | \hat{r}_\mu | v_\alpha \mathbf{k}_\alpha\rangle, \tag{SM16}$$

where $i = \sqrt{-1}$ is the imaginary unit. The summation index α labels electron–hole transitions, each defined by a valence band v_α, a conduction band c_α, and a crystal momentum $\mathbf{k}_\alpha$. The coefficient X_α^λ is the excitonic eigenvector component (or amplitude) for exciton λ, projected onto the transition α. The matrix element $\langle c_\alpha \mathbf{k}_\alpha | \hat{r}_\mu | v_\alpha \mathbf{k}_\alpha\rangle$ represents the dipole transition between valence and conduction states in direction μ, and $\hat{r}_\mu$ is the position operator along that Cartesian direction. In the general BSE formalism (beyond the TDA), the full transition coefficient includes both the resonant (X_α^λ) and anti-resonant (Y_α^λ) contributions:

$$t_{\lambda,\mu}^* = i\sum_\alpha \left(X_\alpha^\lambda + Y_\alpha^\lambda\right)\langle c_\alpha \mathbf{k}_\alpha | \hat{r}_\mu | v_\alpha \mathbf{k}_\alpha\rangle. \tag{SM17}$$

However, within the TDA, the anti-resonant coefficients vanish ($Y_\alpha^\lambda = 0$), reducing Eq. (SM17) to Eq. (SM16). The squared magnitude of $t_{\lambda,\mu}$ determines the oscillator strength of the exciton and thus the intensity of the corresponding peak in the optical absorption spectrum. The dielectric function's imaginary part is constructed from these dipole transition strengths and Lorentzian broadenings centered at $\pm E_\lambda$. Each excitonic state contributes a positive and negative Lorentzian peak, scaled by $|t_{\lambda,\mu}|^2$, and with a broadening width δ. This representation captures the excitation spectrum in terms of resonant light–matter coupling. To avoid ambiguities in periodic systems, the dipole matrix element is often expressed using the momentum operator:

$$\langle c|\hat{r}_\mu|v\rangle = \frac{1}{im_e(\epsilon_c-\epsilon_v)}\langle c|\hat{p}_\mu|v\rangle, \tag{SM18}$$

where $\mu \in \{x, y, z\}$ denotes the Cartesian direction, m_e is the electron mass, and $(\epsilon_c - \epsilon_v)$ is the energy difference between conduction and valence states. Equation (SM18) follows from the commutator identity $[\hat{H}, \hat{r}_\mu] = \frac{i\hbar}{m_e}\hat{p}_\mu$, evaluated between eigenstates $|v\rangle$ and $|c\rangle$ of the single-particle Hamiltonian $\hat{H} = \frac{\hat{\mathbf{p}}^2}{2m_e} + V(\mathbf{r})$. Using $\hat{H}|v\rangle = \epsilon_v|v\rangle$ and $\hat{H}|c\rangle = \epsilon_c|c\rangle$, one obtains $(\epsilon_c - \epsilon_v)\langle c|\hat{r}_\mu|v\rangle = \langle c|[\hat{H}, \hat{r}_\mu]|v\rangle = \frac{i\hbar}{m_e}\langle c|\hat{p}_\mu|v\rangle$. Adopting atomic units where $\hbar = 1$ recovers Eq. (SM18). This identity is particularly useful in periodic systems, where the position operator $\hat{\mathbf{r}}$ is ill-defined, while the momentum operator $\hat{\mathbf{p}}$ remains well-defined for Bloch states.

In Eq. (SM7), the arguments of the resonant two-particle wavefunctions are set equal, i.e., $\Phi_\alpha^{(r)*}(\mathbf{r}_e, \mathbf{r}_e)$ and $\Phi_\beta^{(r)}(\mathbf{r}_h, \mathbf{r}_h)$, signifying that the exchange interaction contributes only when the electron and hole spatially coincide. This restriction underscores the inherently short-range nature of exchange interactions and manifests as a repulsive force between the particles. Crucially, it also enforces the required antisymmetry of the excitonic wavefunction under particle exchange, in accordance with the Pauli exclusion principle—a defining characteristic of fermions. As a result, this term gives rise to local-field effects that shape the optical response at short wavelengths. In spin-triplet excitations, where the electron and hole possess parallel spins, the exchange interaction identically vanishes ($\gamma_{\mathrm{x}} = 0$), since such configurations are Pauli-forbidden from overlapping. The inclusion of exchange and correlation in the BSE is thus controlled by the spin-dependent prefactors γ_{x} and γ_{c}, as expressed in Eq. (SM5), both are unity for spin-singlet states, while only the direct Coulomb attraction ($\gamma_{\mathrm{c}} = 1$) remains active in spin-triplet cases.

The exciton binding energy, defined as the difference between the QP gap and the lowest bright exciton energy, is given by:

$$E_b^{\mathrm{ex}} = E_g^{\mathrm{GW}} - E_g^{\mathrm{opt}}, \tag{SM19}$$

where E_g^{GW} is the QP band gap obtained from $\mathrm{G_0W_0}$ calculations, and E_g^{opt} denotes the lowest bright exciton energy computed from the BSE. As illustrated in Fig. SM5, this binding energy E_b^{ex} corresponds to the energy separation between the onset of the QP continuum and the discrete excitonic levels that appear below it due to electron-hole interactions.

For reference, a hydrogenic model approximates this binding energy as:

$$E_b^{\mathrm{hydro}} = \frac{\mu e^4}{2(4\pi\varepsilon_0\varepsilon_r)^2\hbar^2}, \tag{SM20}$$

where μ is the reduced effective mass and ε_r the relative static dielectric constant of the material. The term ε_0 denotes the vacuum permittivity, and their product defines the absolute static dielectric permittivity: $\varepsilon = \varepsilon_0\varepsilon_r$. This quantity governs the strength of Coulomb interactions and thus controls the degree of exciton binding in insulators and semiconductors. In atomic units, or when working with dimensionless screening properties, it is common to absorb ε_0 into the unit system and treat $\varepsilon \equiv \varepsilon_r$. While instructive, the hydrogenic model fails to capture the anisotropic screening, local-field effects, and complex band dispersion characteristic of halide perovskites. As such, Eq. (SM20) serves primarily as a scaling guideline, motivating the simplified proportionality relation:

$$E_b^{\mathrm{ex}} \propto \frac{\mu}{\varepsilon^2}, \tag{SM21}$$

which we frequently use this proportionality in Sec. SM11 A 2 to interpret trends in exciton binding across chemically related materials and to rationalize the competing roles of band curvature (via μ) and dielectric screening (via ε).

In essence, the GW + BSE framework, as schematically illustrated in Fig. SM5, forms a physically complete and quantitatively accurate approach for modeling the correlated optical response in these complex semiconductors. In this work, we adopt a consistent terminology to distinguish between different levels of approximation within the BSE framework. Specifically, we use the term RPA to denote the configuration in which the exchange interaction $H^{(\mathrm{x})}$ is retained but the screened direct electron–hole attraction $H^{(\mathrm{c})}$ is neglected. This approximation captures short-range local-field effects but omits excitonic binding. By contrast, we refer to the BSE as the full singlet formulation, in which all three components of the effective Hamiltonian—the independent-particle excitation energies ($H^{(\mathrm{diag})}$), the exchange repulsion ($H^{(\mathrm{x})}$), and the screened direct attraction ($H^{(\mathrm{c})}$)—are included. This complete treatment is essential for accurately describing bound excitonic states and the correlated optical response. By reserving the term BSE for the singlet case and using "RPA" for its partially interacting limit, we make explicit the level of many-body physics accounted for in each calculation and facilitate a clear comparison of their impact on optical spectra.

B. Quantifying Spontaneous Polarization via the Berry Phase Formalism

Spontaneous electric polarization, a key feature of ferroelectric materials, emerges from inversion-symmetry-breaking lattice distortions. We evaluate this property within the framework of DFT, using the mTASK meta-GGA functional [20] alongside the `VX_HCTH407` local potential [21].

The total electric polarization $\boldsymbol{P}^{(\lambda)}$ for a structure λ consists of both ionic and electronic contributions:

$$\begin{aligned} \boldsymbol{P}^{(\lambda)} = {} & \frac{e}{\Omega^{(\lambda)}} \sum_{s=1}^{N} Z_s^{\mathrm{ion}(\lambda)} \mathbf{r}_s^{(\lambda)} \\ & + \frac{2e}{(2\pi)^3} \sum_{n=1}^{M} \int_{\mathrm{1BZ}^{(\lambda)}} d\mathbf{k}\, \langle u_{n\mathbf{k}}^{(\lambda)} | -i\nabla_{\mathbf{k}} | u_{n\mathbf{k}}^{(\lambda)} \rangle, \end{aligned} \tag{SM22}$$

where, Z_s^{ion} and $\mathbf{r}_s$ denote the ionic charge and position of atom s, respectively; $\Omega^{(\lambda)}$ is the unit cell volume; and $u_{n\mathbf{k}}^{(\lambda)}$ are the cell-periodic Bloch functions. The first term captures the classical ionic contribution, while the second term represents the Berry-phase-derived electronic polarization.

The spontaneous polarization is defined as the difference between the polar and reference (centrosymmetric) structures:

$$\boldsymbol{P}_s = \boldsymbol{P}^{(1)} - \boldsymbol{P}^{(0)}. \tag{SM23}$$

This formulation, grounded in the modern theory of polarization [5–7, 22, 23], ensures gauge invariance and physical consistency in periodic systems. For additional context and numerical details, see also Ref. [18, 24].

C. Theoretical Framework for Bader Charge Analysis

To evaluate the distribution of electron density and quantify charge transfer in solids, we employ Bader charge analysis, rooted in the quantum theory of atoms in molecules (QTAIM) [25, 26]. This method partitions the total electron density $\rho(\mathbf{r})$ into non-overlapping atomic basins Ω_i, bounded by zero-flux surfaces that satisfy:

$$\nabla\rho(\mathbf{r}) \cdot \hat{n}(\mathbf{r}) = 0, \tag{SM24}$$

where $\hat{n}(\mathbf{r})$ is the unit normal vector to the surface at position $\mathbf{r}$. These surfaces define the spatial extent of each atom in a molecule or solid, enabling calculation of Bader charges. The Bader charge q_i of atom i is computed as the integral of the electron density over its atomic basin:

$$q_i = \int_{\Omega_i} \rho(\mathbf{r})\, d\mathbf{r}. \tag{SM25}$$

To understand the deviation from formal ionic character, we define the charge transfer or deviation of an atom's Bader charge from its nominal (free-space) oxidation state:

$$\Delta q_i = q_i^{\text{crystal}} - q_i^{\text{nominal}}, \tag{SM26}$$

and its absolute value:

$$|\Delta q_i| = |q_i^{\text{crystal}} - q_i^{\text{nominal}}|. \tag{SM27}$$

In this context, larger deviations Larger $|\Delta q_i|$—the deviation of Bader charge from the nominal ionic charge—indicate stronger covalent character, whereas smaller $|\Delta q_i|$ indicate a more ionic character. The nominal charges used in this work are $+1e$ for Cs and Rb, $+2e$ for Ge, and $-1e$ for Cl, Br, and I. To verify charge conservation within the unit cell, we also compute the stoichiometric neutralization (SN), defined as the deviation from total valence neutrality:

$$\text{SN} = \sum_i q_i - N_e, \tag{SM28}$$

where N_e is the total number of electrons in the unit cell based on chemical stoichiometry. All Bader charge calculations were performed on all-electron DFT charge densities obtained using WIEN2k [14, 27] and post-processed with the Critic2 package [28, 29], ensuring a consistent and high-resolution partitioning of the electronic density. More detailed discussions of charge density features and the definitions of critical points can be found in Refs. [30, 31].

D. Visualizing Bonding Through the Electron Localization Function (ELF)

To elucidate real-space features of bonding and electron pairing in halide perovskites, we employ the ELF [32]. ELF provides a quantitative measure of the probability of locating a same-spin electron near a reference electron, thereby revealing regions of chemical bonding, lone pairs, and electronic delocalization. Values of ELF close to unity indicate strong localization, typically associated with covalent bonds or non-bonding electron pairs, whereas values near 0.5 reflect delocalized or metallic-like electronic distributions.

The ELF is defined as:

$$\text{ELF}(\mathbf{r}) = \frac{1}{1 + \chi(\mathbf{r})}, \tag{SM29}$$

where the dimensionless localization index $\chi(\mathbf{r})$ is expressed as:

$$\chi(\mathbf{r}) = \frac{D(\mathbf{r})}{D_h(\mathbf{r})}, \tag{SM30}$$

with $D_h(\mathbf{r})$ denoting the kinetic energy density of a homogeneous electron gas and

$$D(\mathbf{r}) = \frac{1}{2}\sum_{i=1}^{N} |\nabla\psi_i(\mathbf{r})|^2 - \frac{1}{8}\frac{|\nabla\rho(\mathbf{r})|^2}{\rho(\mathbf{r})}, \tag{SM31}$$

representing the Pauli excess kinetic energy density. Here, $\rho(\mathbf{r})$ is the electron density, and $\psi_i(\mathbf{r})$ are the KS orbitals.

This framework enables chemically intuitive visualizations of bonding environments and lone-pair distributions, particularly relevant in structurally distorted, polar phases of halide perovskites.

SM9. COMPUTATIONAL DETAILS

To capture the QP electronic structure and excitonic optical response of Rb-doped $CsGeX_3$ (X = Cl, Br, I) perovskites, we employed the all-electron, full-potential linearized augmented plane wave (FP-LAPW) method, as implemented in the EXCITING code [33, 34]. This approach avoids pseudopotentials and ensures high fidelity in treating core-valence interactions and orbital hybridization—an appropriate feature for systems with heavy halogens and stereochemically active lone-pair cations such as Ge^{2+}. The KS ground-state was obtained within the generalized gradient approximation (GGA) using the Perdew–Burke–Ernzerhof (PBE) exchange-correlation functional [35], providing a reference for subsequent many-body corrections. For Brillouin zone sampling, we used k-point meshes of $2 \times 2 \times 1$ for GW-level calculations and $3 \times 3 \times 1$ for GGA-level optimizations. The plane-wave cutoffs were set via rgkmax = 5.0 (7.0) and gmaxvr = 12 (14) for calculations with (without) GW corrections, where rgkmax = $R_{\mathrm{MT}}K_{\mathrm{max}}$ defines the product of the smallest muffin-tin radius R_{MT} and the maximum reciprocal lattice vector K_{max} entering the basis set. The QP energy corrections $\epsilon^{\mathrm{QP}}_{n\mathbf{k}}$ were obtained via the single-shot G_0W_0 approximation [9], evaluating the non-Hermitian, energy-dependent self-energy $\Sigma(\omega) = iGW(\omega)$ on top of the PBE starting point. The frequency-dependent dielectric function $W(\mathbf{r}, \mathbf{r}'; \omega)$ was constructed using 30 unoccupied bands to ensure convergence of screening in the polarizable medium. This setup captures dynamical screening effects and enables accurate corrections to the KS eigenvalues through Eq. (SM3), which is suitable for quantitatively reliable predictions of optical gaps and exciton binding energies, as outlined in Sec. SM8 A. Excitonic effects were explicitly included by solving the BSE for singlet neutral excitations, using the QP energies $\epsilon^{\mathrm{QP}}_{n\mathbf{k}}$ as input. The BSE Hamiltonian $H^{(\mathrm{eff})}$ was constructed according to Eq. (SM5), incorporating the independent-particle term $H^{(\mathrm{diag})}$, the repulsive bare exchange kernel $H^{(\mathrm{x})}$ [Eq. (SM7)], and the attractive screened direct term $H^{(\mathrm{c})}$ [Eq. (SM8)]. To reduce computational expense while retaining accuracy, we applied the TDA, neglecting off-diagonal blocks H^{ra} and H^{ar} in Eq. (SM10), a valid simplification near the absorption onset [19]. For the lowest-energy optical excitations, we included the top six valence and bottom six conduction bands in the transition space (e.g., `nstlbse = "157 162 1 6"` for $CsGeCl_3$). However, to compute the full dielectric response and capture the high-energy continuum, we extended the number of valence bands up to 50 while maintaining six conduction bands (e.g., `nstlbse = "109 162 1 6"`). BSE matrix elements were sampled on a $6 \times 6 \times 2$ k-point grid, ensuring accurate resolution of excitonic fine structure and convergence of exciton binding energies as defined in Eq. (SM19). Optical absorption spectra were calculated via Eq. (SM15), using a Lorentzian broadening $\delta = 0.007$ Ha and an energy mesh spanning 0 to 1.0 Ha with 1200 points. Benchmark spectra at the RPA level, omitting the screened interaction term $H^{(\mathrm{c})}$ but retaining $H^{(\mathrm{x})}$, were also computed to contrast the effects of excitonic binding. The dipole matrix elements entering the BSE oscillator strengths were evaluated in both real-space and momentum-space forms using Eqs. (SM16) and (SM18), respectively, ensuring gauge-invariant results in periodic systems.

Ferroelectric and ground-state electronic properties were calculated using the WIEN2k package [36], an all-electron code based on the FP-(L)APW+lo formalism within the framework of DFT [14, 27]. This method provides a numerically precise, basis-set-complete treatment of core and valence states, essential for resolving fine structural distortions and anisotropic charge distributions in polar halide perovskites. To assess exchange-correlation functional dependence, we adopted both the semi-local PBE-GGA functional [35] and the strongly constrained and appropriately normed (SCAN) meta-GGA functional [20], which captures intermediate-range correlation and inhomogeneous charge localization more accurately. Notably, the SCAN functional has been shown to yield improved structural predictions and more accurate spontaneous polarization values for ferroelectric systems compared to semi-local approaches. The spontaneous electric polarization was computed using the modern theory of polarization, implemented via the Bp formalism [5–7, 22, 23]. Within this framework, the total macroscopic polarization vector $\boldsymbol{P}^{(\lambda)}$ of a structure λ is decomposed into an ionic contribution—proportional to the product of atomic charges and displacements—and an electronic term expressed as the Brillouin zone integral of the Berry connection over occupied cell-periodic Bloch states. This formulation is given explicitly in Eq. (SM22) in Sec. SM8 B. To evaluate the spontaneous polarization $\boldsymbol{P}_s$, we computed the difference in total polarization between the polar and a suitably chosen centrosymmetric reference structure, as defined by Eq. (SM23). This subtraction inherently accounts for the polarization lattice and branch-dependent phase discontinuities, ensuring gauge invariance and compatibility with periodic boundary conditions. Computational parameters were tightly converged: the product $R_{\mathrm{MT}}K_{\mathrm{max}}$ was set to 7.0, and the Fourier expansion of the charge density included reciprocal vectors up to 14 Bohr^{-1}. Brillouin zone sampling was carried out using a dense Monkhorst-Pack grid with approximately 2000 irreducible k-points, ensuring convergence of total energy and polarization to better than 10^{-5} Ha and 0.001 eÅ,

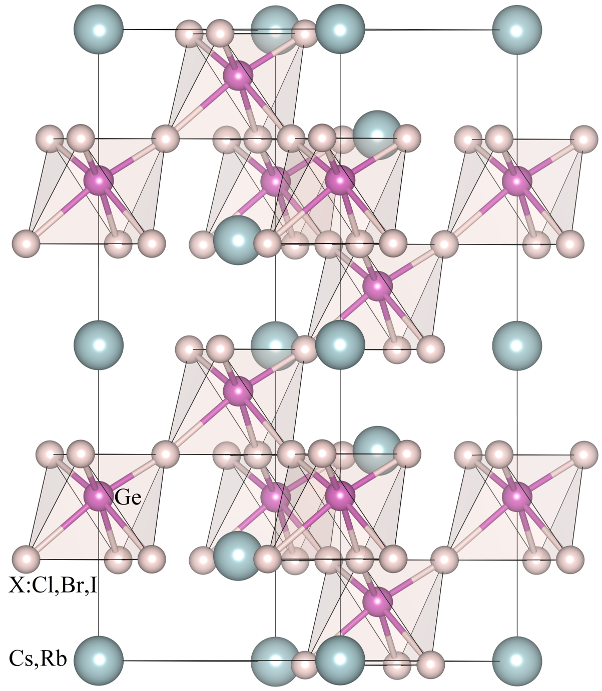

FIG. SM6. Crystallographic structure of the 1×1×2 supercell of Rb-doped $CsGeX_3$ (X = Cl, Br, I) in the hexagonal setting of the rhombohedral *R3m* space group. Ge atoms (purple spheres) form a framework of corner-sharing GeX_6 octahedra with halogen ligands (light pink spheres), while Cs and Rb atoms (large blue spheres) occupy the 12-fold coordinated A-site cavities. The doping level corresponds to a nominal 16.67% substitution of Cs by Rb. The structure highlights polar distortions along the *c*-axis and the three-dimensional connectivity of the perovskite lattice, which underlie the material's ferroelectric and optoelectronic properties.

respectively. This resolution is essential for quantifying subtle off-centering of Ge atoms, octahedral tilts, and A-site size effects arising from Rb doping. In addition to the Berry-phase-derived polarization, structural distortions were correlated with lone-pair localization features extracted from the ELF, described in Sec. SM8 D. The real-space ELF patterns—sensitive to the Pauli repulsion and curvature of the KS orbitals—provide complementary insight into the electronic driving forces behind ferroelectricity. The combination of Berry-phase polarization and ELF topological analysis allows for a chemically intuitive and physically rigorous interpretation of structure–property relationships in this class of materials. In Rb-substituted $CsGeX_3$, the interplay between A-site chemical pressure, octahedral framework flexibility, and lone-pair stereochemistry emerges as a key mechanism underpinning the observed polarization trends.

To complement the electronic structure and polarization analysis, we implemented a Python-based image processing pipeline to quantitatively assess lone-pair localization in the ELF, as introduced in Sec. SM8 D. This analysis offers a visual and statistical measure of the stereochemical activity of the Ge $4s^2$ lone pair, which plays a pivotal role in breaking inversion symmetry and inducing polar displacements. ELF visualizations—generated in WIEN2k—were exported as high-resolution images and converted to grayscale and HSV (hue-saturation-value) formats using the OpenCV computer vision library. Purple regions, indicative of strong same-spin electron localization associated with non-bonding s^2 electron pairs, were extracted via color segmentation with calibrated HSV thresholds (Hue: 120–160). Morphological operations (e.g., erosion, dilation) were applied to eliminate noise and enhance feature clarity. Each segmented ELF map was partitioned into subregions corresponding to distinct halide compositions ($CsGeCl_3$, $CsGeBr_3$, $CsGeI_3$), allowing for compositionally resolved quantification. For each subregion, the number of lone-pair pixels was counted and normalized by the total number of ELF-active pixels, yielding a dimensionless localization index $\eta_{\mathrm{lp}} = A_{\mathrm{lp}}/A_{\mathrm{ELF}}$ comparable across chemical environments. This metric correlates directly with the degree of electronic asymmetry and complements the Berry-phase polarization $\boldsymbol{P}_s$ computed in Sec. SM8 B. In $CsGeCl_3$, large η_{lp} values reflect pronounced lone-pair activity and strong polarization, while in $CsGeI_3$, the enhanced dielectric screening suppresses localization, reducing both η_{lp} and $\boldsymbol{P}_s$. These trends highlight the synergy between real-space ELF-based descriptors and reciprocal-space Berry-phase theory in capturing the fundamental interplay between stereochemistry, dielectric screening, and emergent ferroelectric behavior.

SM10. CRYSTAL STRUCTURE AND DOPING-INDUCED DISTORTIONS IN Rb-SUBSTITUTED $CsGeX_3$ PEROVSKITES

To investigate the effects of Rb doping in halide perovskites, we constructed supercells based on the hexagonal representation of the rhombohedral phase (space group $R3m$) of pristine $CsGeX_3$ (X = Cl, Br, I). The primitive unit cell comprises three inequivalent atoms, with one occupying a triply degenerate Wyckoff position. To enable doping and capture the associated structural response, the unit cell was replicated along the c-axis to form a $1\times1\times2$ supercell, resulting in a 30-atom configuration containing 6 Cs, 6 Ge, and 18 halogen atoms, as illustrated in Fig. SM6. The structure consists of a network of corner-sharing GeX_6 octahedra, where Ge atoms (purple spheres) reside at the octahedral centers and are coordinated by six halogen atoms (light pink spheres). The larger blue spheres represent Cs and Rb atoms occupying the A-sites in the perovskite framework.

Rb doping was modeled by substituting a single Cs atom, corresponding to a nominal concentration of 16.67%. Full atomic relaxations were performed to accommodate the local lattice distortions induced by the smaller ionic radius of Rb^+ (1.52 Å) compared to Cs^+ (1.67 Å). The resulting chemical pressure alters the local bonding environment, shifts the effective tolerance factor $t = \frac{r_A+r_X}{\sqrt{2}(r_B+r_X)}$, and perturbs the symmetry of the octahedral framework. These effects contribute to the emergence or modulation of polar displacements, octahedral tilting, and local electronic polarization.

The hexagonal setting explicitly emphasizes the polar stacking direction along $[001]_{\text{hex}}$, enabling a direct visualization of dipolar distortions and spontaneous symmetry breaking that underlie the material's ferroelectricity. The asymmetric displacements of Ge atoms and the cooperative tilting of GeX_6 octahedra break inversion symmetry and support a net polarization along the trigonal axis. Such distortions are central to the manifestation of ferroelectricity and result from second-order Jahn–Teller effects associated with the stereochemically active s^2 lone pair on Ge^{2+}.

This structural framework, especially under A-site substitutional doping, is not only critical for understanding the emergent dielectric and optical properties of halide perovskites but also provides a realistic basis for high-fidelity first-principles simulations. The supercell in Fig. SM6 offers a quantitatively calibrated and chemically consistent model for exploring dopant-induced modifications to the physical properties of lead-free perovskites within the many-body and lattice-dynamics frameworks.

SM11. RESULTS AND DISCUSSION

Our investigation unfolds in three stages within a unified multiscale framework aimed at elucidating the photoferroelectric behavior of $CsGeX_3$ (X = Cl, Br, I) halide perovskites and their Rb-doped counterparts, with a particular focus on identifying the primary origin of spontaneous electric polarization in these materials. In Part I, many-body perturbation theory reveals how Rb incorporation and hydrostatic compression jointly reconfigure the excitonic landscape—enhancing exciton localization and modulating band-edge transitions. These effects signal pathways for integrating ferroelectric and optoelectronic functionalities. Part II examines macroscopic ferroelectricity and shows that spontaneous polarization decreases with increasing tetragonality (c/a)—a surprising deviation from conventional expectations. Rb substitution amplifies polar bistability, as evidenced by double-well energy profiles, while Bp and Born effective charge (BEC) analyses track the evolution of spontaneous polarization and polar displacements across the series. In Part III, we aim to resolve the fundamental origin of spontaneous polarization by disentangling the microscopic mechanisms that drive it. By combining Bader charge analysis with ELF mapping, we interrogate the interplay between structural distortions and the stereochemically active lone pairs on Ge atoms. This analysis reveals how geometric anisotropy and localized electronic asymmetry interact—sometimes cooperatively, sometimes competitively—to stabilize long-range polar order in these halide perovskites. Together, these findings establish design principles for tuning structural and electronic interactions in next-generation photoferroelectric materials.

A. Part I: Quantum Optics

This part presents a systematic analysis of the optical response in $CsGeX_3$ perovskites and their Rb-doped counterparts, combining many-body theory with electronic structure insights. Starting with the identification of excitonic signatures and dielectric anisotropy in pristine compounds (Sec. SM11 A 1), we then explore how Rb doping and external strain modulate exciton binding, band gaps, and light–matter coupling for device-relevant applications (Sec. SM11 A 2 and Sec. SM11 A 3). The dielectric screening behavior is further examined via the energy loss function (ELOSS), revealing strain-tunable dissipation and ferroelectric stability (Sec. SM11 A 4). Finally, projected density of states (DOS) analyses provide the orbital-level understanding of optical transitions and establish the electronic roots of spontaneous polarization (Sec. SM11 A 5). Together, these five subsections build a unified picture of how compositional and structural tuning governs the interplay between excitonic phenomena, dielectric properties, and ferroelectric tendencies in lead-free halide perovskites.

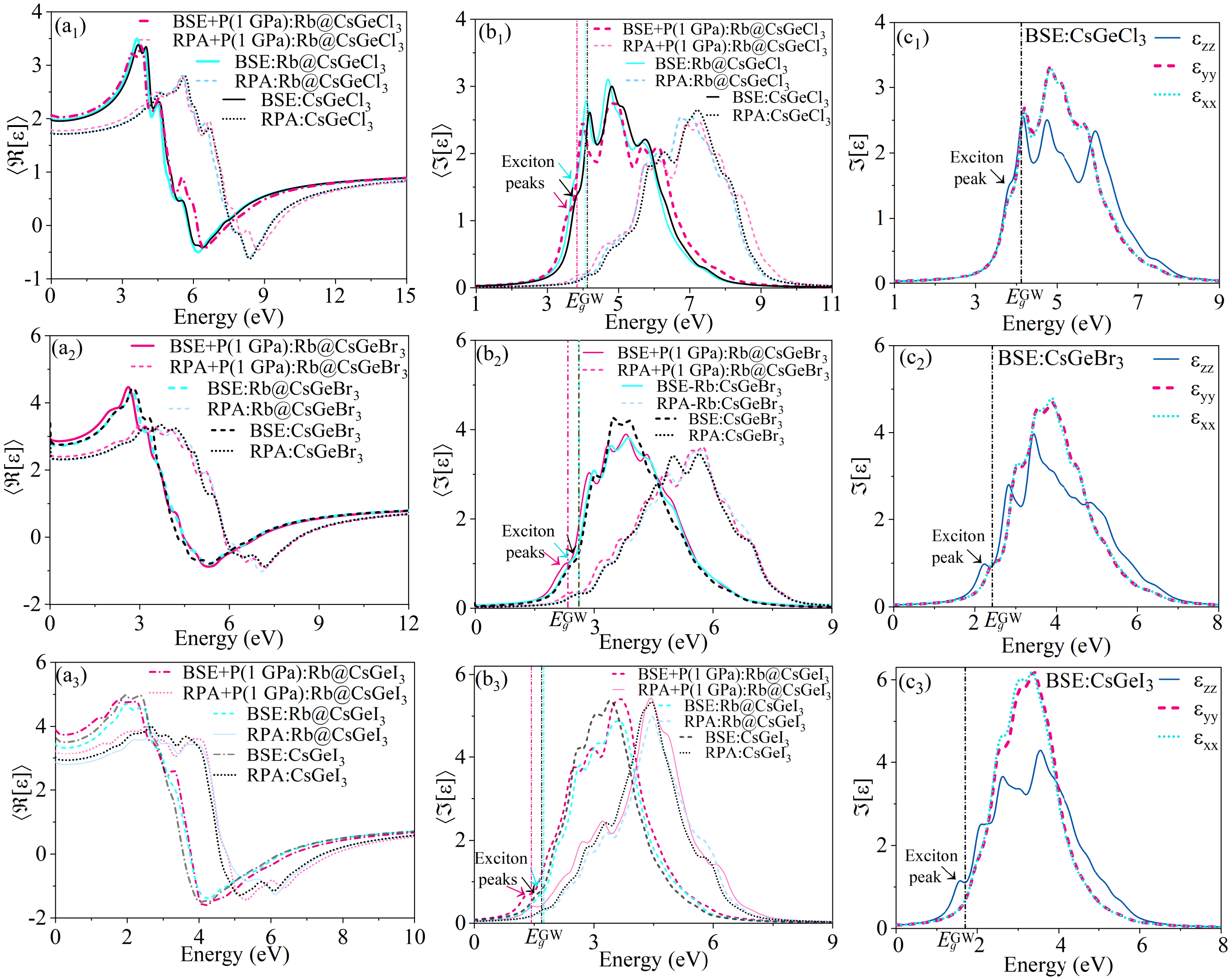

FIG. SM7. Macroscopic optical response of pristine and Rb-doped $CsGeX_3$ (X = Cl, Br, I) perovskites, computed using the GGA+GW+BSE framework. Panels (a_i, $i = 1, 2, 3$) show the real part of the dielectric function, $\langle \Re[\varepsilon(\omega)] \rangle$, averaged over in-plane and out-of-plane components. Panels (b_i) display the corresponding imaginary parts, $\langle \Im[\varepsilon(\omega)] \rangle$, capturing absorption spectra with and without excitonic effects via BSE and RPA, respectively. Clear excitonic resonances emerge below the QP band gap E_g^{GW} (indicated by vertical green dashed lines), especially in $CsGeCl_3$ and $CsGeBr_3$, reflecting strong electron–hole interactions in low-screening environments. Doping with Rb and applying hydrostatic pressure systematically modulate the dielectric response by altering the electronic structure and screening. Panels (c_i) present the polarization-resolved components ε_{xx}, ε_{yy}, and ε_{zz} of $\Im[\varepsilon(\omega)]$ for the pristine compounds, highlighting dielectric anisotropy and directionally dependent excitonic absorption. These results demonstrate the crucial role of many-body effects in accurately predicting optical spectra and guiding the design of halide perovskites for optoelectronic and excitonic applications.

1. *Excitonic Signatures and Anisotropic Dielectric Response in $CsGeX_3$ Perovskites*

To accurately capture the optical response of $CsGeX_3$ perovskites (X = Cl, Br, I), especially the excitonic features central to optoelectronic functionality, we utilize the G_0W_0+BSE framework introduced in Sec. SM8 A and illustrated in Fig. SM5. This many-body approach incorporates both QP renormalization and correlated electron–hole dynamics, enabling a predictive description of bound optical excitations. Fig. SM7 presents the calculated macroscopic dielectric function for pristine, Rb-doped, and pressure-tuned $CsGeX_3$ systems, derived using the QP energies obtained from the G_0W_0 approximation [Eq. (SM3)], and optical spectra computed from both the full singlet BSE and its partially interacting RPA limit, as defined through the components of Eq. (SM5). Panels (a_i, $i = 1, 2, 3$) display the real part $\Re[\varepsilon(\omega)]$, averaged over in-plane and out-of-plane components. Panels (b_i) and (c_i) depict the imaginary part $\Im[\varepsilon(\omega)]$, either averaged or polarization-resolved along crystallographic axes. The vertical dashed lines in (b_i) and (c_i) indicate the QP band gaps E_g^{GW}, obtained from G_0W_0 theory. These spectra encode the effects of excitonic binding, which manifest as discrete low-energy resonances below E_g^{GW}, consistent with the formation of correlated two-particle states governed by the effective Hamiltonian in Eq. (SM4). The energy difference between the QP band gap and the lowest bright exciton, corresponding to the peak onset in $\Im[\varepsilon(\omega)]$, directly yields the exciton binding energy E_b^{ex}, as defined in Eq. (SM19). This framework provides a robust foundation for analyzing optical anisotropy, electron–hole correlation strength, and tunability of light–matter interactions in polar, low-screening semiconductors.

The dielectric screening behavior, as depicted in Fig. SM7(a$_i$), reveals the profound influence of many-body correlations on the static and low-frequency optical response of $\mathrm{CsGeX_3}$ (X = Cl, Br, I). In the absence of excitonic effects, the BSE-RPA approximation yields static dielectric constants (ε_0) of 1.72, 2.20, and 3.01 for $\mathrm{CsGeCl_3}$, $\mathrm{CsGeBr_3}$, and $\mathrm{CsGeI_3}$, respectively. Upon including the screened electron–hole attraction via the full BSE kernel, these values increase to 1.98, 2.43, and 3.53, underscoring the crucial role of Coulomb-correlated excitations in enhancing dielectric response. This enhancement, visualized by the zero-frequency intercepts of $\Re[\varepsilon(\omega)]$ in Fig. SM7(a$_i$), connects directly to the excitonic binding discussed in Sec. SM8 A and Eq. (SM19), where reduced band gaps and weak screening increase the exciton binding energy E_b^{ex}. The observed monotonic increase in ε_0 across the halogen series from Cl to I reflects the trend in orbital diffuseness and polarizability, with heavier halogens contributing to stronger interband dipole transitions. This also mirrors the decreasing QP band gaps E_g^{GW} shown by the leftward shift of the green dashed lines in Fig. SM7(b$_i$), which are consistent with the energy differences $\epsilon_c - \epsilon_v$ in Eq. (SM18). Importantly, the dielectric enhancement is not merely a static screening effect but originates from the summation over low-energy dipole-allowed excitons with large oscillator strengths, as encoded in Eq. (SM16). This underscores the technological importance of $\mathrm{CsGeX_3}$ perovskites in next-generation photonic and excitonic devices, where the tunability of the dielectric function $\varepsilon(\omega)$ governs key performance metrics including light–matter coupling strength, exciton–polariton dispersion, and the capacitive response of layered heterostructures. Notably, the lower static dielectric constants ε_0 reported here contrast with previous $\mathrm{G_3W_0}$+BSE results [1], which yield systematically higher values. This discrepancy primarily stems from methodological distinctions in the many-body treatment. Specifically, the present $\mathrm{G_0W_0}$+BSE calculations employ a single-shot update of QP energies, while the $\mathrm{G_3W_0}$ approach iteratively refines G over three cycles, thereby introducing additional QP renormalization that tends to increase screening. Moreover, variations in the construction of the BSE Hamiltonian—including the number of QP transitions retained in $H^{(\mathrm{diag})}$ [see Eq. (SM6)], the density of $\mathbf{q}$-point sampling, and the treatment of the screened Coulomb kernel $W(\mathbf{r}_e, \mathbf{r}_h)$ in Eq. (SM8)—contribute significantly to the observed shifts in ε_0. These factors collectively highlight the sensitivity of dielectric predictions to computational protocol and reinforce the need for carefully benchmarked many-body methodologies in materials design. These factors influence not only the exciton binding energies but also the low-energy dielectric response, highlighting the necessity of methodological consistency and parameter convergence in predictive many-body simulations of optical properties in low-screening semiconductors.

The observed increase in the static dielectric constant ε_0 with the atomic number of the halogen (Cl $\longrightarrow$ Br $\longrightarrow$ I) and the concomitant narrowing of the QP band gap E_g^{GW} (Fig. SM7(a$_i$–b$_i$)) reflect a fundamental interplay between lattice polarizability and electronic structure. This behavior, while qualitatively consistent with earlier $\mathrm{G_3W_0}$+BSE calculations [1], differs quantitatively due to distinct methodological frameworks. For instance, while our $\mathrm{G_0W_0}$+BSE results yield $\varepsilon_0 \approx 1.98$, 2.43, and 3.53 for $\mathrm{CsGeCl_3}$, $\mathrm{CsGeBr_3}$, and $\mathrm{CsGeI_3}$, respectively, the corresponding values reported in Ref. [1] are 2.45, 2.85, and 4.19. Such deviations may arise from differences in the treatment of the self-energy operator, $\Sigma = iGW$ (Sec. SM8 A, Eq. (SM3)), as well as from the specific form of the excitonic kernel employed in the BSE Hamiltonian (Eq. (SM5)).

This halogen-dependent dielectric enhancement can be understood in terms of the increased polarizability and heavier atomic mass of the halide ion, both of which affect the screening behavior $\varepsilon^{-1}(\mathbf{r}, \mathbf{r}')$ (Eq. (SM9)) and the spatial extent of excitonic wavefunctions. From a microscopic perspective, moving from Cl to I, the X-p contribution at the valence-band maximum becomes increasingly delocalized and exhibits stronger X-p–Ge-s hybridization (see Fig. 3 and the band-decomposed charge densities in Fig. 4 of Ref.[1]), which enhances electronic polarizability and increases the dipole matrix elements—and hence the oscillator strength $|t_{\lambda\mu}|^2$—of excitonic transitions (Eqs. (SM16)–(SM17)). This increased polarizability not only shifts absorption onsets to lower energies (as seen from the leftward movement of the vertical dashed lines in Fig. SM7(b$_i$)), but also reduces the exciton binding energy E_b^{ex} (Eq. (SM19)), owing to stronger dielectric screening of the electron–hole Coulomb attraction (Eq. (SM8)). Technologically, these trends underscore the tunability of optical absorption and excitonic resonances via halide substitution, providing a chemically tractable strategy for band gap engineering and dielectric tailoring. Notably, the I-based compound, with its higher ε_0 and lower E_b^{ex}, is more suited for photovoltaic applications where efficient charge separation is desired. In contrast, the Cl- and Br-based compounds, exhibiting sharper and more tightly bound excitonic features, may be advantageous for exciton-based optoelectronics such as polariton lasers or quantum light sources, where strong light–matter coupling and long exciton lifetimes are required. The accurate prediction of such structure–property relationships, rooted in many-body theory and dielectric anisotropy, validates the use of $\mathrm{G_0W_0}$+BSE as an essential computational protocol for material design in halide perovskites.

As illustrated in Figs. SM7(b$_i$, $i = 1, 2, 3$), incorporating electron–hole interactions via the BSE-singlet formalism introduces a significant redshift in the spectral onset and absorption maxima of $\Im[\varepsilon_M(\omega)]$, relative to the BSE-RPA spectra. This shift, observable across all $\mathrm{CsGeX_3}$ compositions, is a hallmark of exciton formation and confirms the emergence of correlated two-particle states below the QP gap E_g^{GW}. These low-energy features, highlighted by arrows in Fig. SM7(b$_i$), represent the optical activation of bound excitonic states and originate from solutions of the BSE eigenvalue problem given in Eq. (SM11). Each peak corresponds to an excitonic excitation with binding energy E_b^{ex}, defined rigorously via Eq. (SM19) as the energy difference between the QP band edge and the lowest bright exciton. The redshifted peaks manifest strong dipole transition strengths $|t_{\lambda,\mu}|^2$ as introduced in Eq. (SM16), indicating not only the presence but also the radiative nature of these excitons. Furthermore, the consistent appearance of such features across all halogen variants and doping/pressure conditions highlights their robustness and tunability, thus offering a promising handle for targeted engineering of excitonic processes in optoelectronic architectures. In low-dimensional or polar semiconductors such as halide perovskites, this behavior stems from suppressed dielectric screening (as inferred from the values in Fig. SM7(a$_i$)) and enhanced localization of electronic wavefunctions—factors that promote strong Coulomb binding, consistent with the screened interaction $W(\mathbf{r}_e, \mathbf{r}_h)$ in Eq. (SM9). Importantly, this excitonic enhancement of the optical absorption onset implies that photon energies well below the QP gap can be efficiently harvested, making these materials excellent candidates for low-energy photodetection, sub-bandgap photovoltaics, and quantum light emission. As we shall explore in Table SM2, the quantitative comparison of E_g^{opt} and E_g^{GW} across pristine and Rb-doped systems further elucidates how compositional and external perturbations modulate exciton binding strengths and thereby the device-relevant spectral window.

The exciton binding energy, defined as the energy required to dissociate a photoexcited electron–hole pair into free carriers, is given by Eq. (SM19) as the difference $E_b^{\text{ex}} = E_g^{\text{GW}} - E_g^{\text{opt}}$ between the QP gap and the lowest bright exciton energy. This energetic separation is directly visible in the spectra of Fig. SM7(b$_i$), where the vertical dashed lines denote E_g^{GW} and the sharp low-energy features marked by arrows correspond to the first optically allowed excitonic states computed from the BSE. These discrete states lie below the continuum onset, signifying strongly bound excitons—a hallmark of materials with low dielectric screening and moderate effective masses. Within the BSE framework (see Sec. SM8 A), these excitonic states emerge from the full two-particle Hamiltonian of Eq. (SM4), which combines the QP electronic structure ($H^{(\text{diag})}$) with both short-range exchange repulsion ($H^{(\text{x})}$) and long-range screened Coulomb attraction ($H^{(\text{c})}$). The magnitude of E_b^{ex} is highly sensitive to the screening properties encoded in $\varepsilon^{-1}(\mathbf{r}, \mathbf{r}')$ [see Eq. (SM9)], which determine the strength of $H^{(\text{c})}$ and thus the degree of electron–hole binding. As shown in Fig. SM7(b$_i$), $CsGeCl_3$ exhibits the largest exciton binding energy, with the BSE peak located significantly below the QP edge, consistent with its low dielectric constant and relatively flat conduction bands. This is in contrast to $CsGeI_3$, where the increased dielectric screening—originating from the more polarizable I^- anions—reduces the Coulomb attraction and shifts the exciton closer to the continuum, yielding a smaller E_b^{ex}. The quantitative trends extracted from these spectra align with the systematic increase in $\langle \Re[\varepsilon(0)] \rangle$ reported in Fig. SM7(a$_i$), confirming the inverse correlation between screening strength and exciton binding. Furthermore, the excitonic peaks correspond to transitions with enhanced oscillator strength $|t_{\lambda,\mu}|^2$ [see Eq. (SM16)], reflecting strong dipole coupling in the optical limit. These transitions dominate the low-energy absorption and are governed by both band dispersion and transition matrix elements, which in turn depend on orbital symmetry and hybridization. While orbital character will be rigorously analyzed in Sec. SM11 A 5, the presence of tightly bound excitons in $CsGeCl_3$ and $CsGeBr_3$ already points to pronounced orbital localization and strong Ge–X bonding. Such properties are technologically relevant, as large E_b^{ex} values can stabilize excitonic features at room temperature, enabling efficient light–matter coupling in optoelectronic applications such as photodetectors and solar cells, particularly in low-dimensional or quantum-confined architectures where dielectric mismatch can enhance excitonic effects even further. Thus, the combined influence of QP corrections, dielectric screening, and many-body Coulomb interactions—each rigorously accounted for in the GW+BSE formalism—converge to yield a physically complete and spectroscopically accurate description of excitonic phenomena in $CsGeX_3$ perovskites. These insights form the foundation for interpreting and engineering optical responses in halide-based semiconductors and heterostructures.

To elucidate the anisotropic nature of excitonic absorption in $CsGeX_3$, we now turn to the polarization-resolved components of the macroscopic dielectric function, as shown in panels (c$_i$) of Fig. SM7. These plots display $\Im[\varepsilon_{\mu\mu}(\omega)]$ for $\mu = x, y, z$ in pristine compounds, computed using the full BSE formalism. Strikingly, for all halides, the out-of-plane (ε_{zz}) component dominates the excitonic peak intensity, particularly in $CsGeBr_3$ and $CsGeI_3$, where the low-energy resonances below E_g^{GW} (see Fig. SM5) are sharply pronounced and spectrally isolated. This behavior indicates that the dipole transition matrix element $\langle c_\alpha \mathbf{k} | \hat{r}_z | v_\alpha \mathbf{k} \rangle$ in Eq. (SM16) carries significantly more oscillator strength than its in-plane counterparts, pointing to a strongly polarized excitonic wavefunction along the crystallographic c-axis. The emergence of this anisotropy is intimately connected to the rhombohedral $R3m$ structure and the stacking of GeX_6 octahedra along z, which induces directional orbital overlap and reduced dielectric screening along the out-of-plane axis. The weak response in ε_{xx} and ε_{yy}, especially for heavier halogens, highlights the confinement of optical activity to the interlayer axis, further reinforced by the ELF analysis in Sec. SM8 D, where lone-pair electrons on Ge are localized in a quasi-two-dimensional fashion. In $CsGeCl_3$, the spectral weight in ε_{xx} and ε_{yy} remains appreciable, suggesting more isotropic bonding and reduced structural anisotropy. This evolution from isotropic to anisotropic exciton character aligns with the increasing static dielectric constants observed in Fig. SM7(a$_i$) and quantified via BSE in previous paragraphs, confirming that excitonic features intensify and polarize as dielectric screening and lattice distortion grow more directional. From a practical perspective, such out-of-plane exciton orientation offers distinct technological advantages for designing polarization-sensitive optoelectronic devices, such as anisotropic photodetectors and out-of-plane light-emitting diodes (LEDs). These results emphasize that accurate modeling of $\varepsilon_{\mu\mu}(\omega)$ using Eq. (SM15), and the full inclusion of many-body effects, is crucial to capturing the directional light–matter interactions that govern excitonic processes in halide perovskites.

As shown in Fig. SM7(c_i), the dielectric anisotropy intensifies with increasing halogen atomic number, as evidenced by the dominant contribution of ε_{zz} to the excitonic peak in $CsGeBr_3$ and $CsGeI_3$, whereas in $CsGeCl_3$, the lower-energy resonances maintain measurable in-plane components ε_{xx} and ε_{yy}. This directional selectivity reflects the underlying orbital hybridization along the crystallographic z-axis, which becomes increasingly prominent as the heavier halogens deepen the Ge−p−X−p overlap and narrow the valence bandwidth. In light of the BSE-derived transition dipoles $t_{\lambda,\mu}$ [Eq. (SM16)], the optical anisotropy signifies a real-space polarization of the excitonic envelope function along z, corresponding to stronger oscillator strengths for interband transitions mediated by $\hat{r}_z$. Such anisotropy is a natural consequence of the layered distortion in the *R3m* phase, where the ferroelectric displacement (quantified in Sec. SM8 B) lifts inversion symmetry and enhances out-of-plane dielectric response. From a practical standpoint, this implies that polarization-resolved absorption or photoluminescence measurements can be used to probe exciton alignment and confinement. Moreover, the out-of-plane-dominated excitonic behavior in $CsGeBr_3$ and $CsGeI_3$ paves the way for directionally selective excitonic devices, such as anisotropic light-harvesting layers and vertically integrated photodetectors. The evolution from isotropic to quasi-one-dimensional dielectric behavior underscores the interplay between crystallographic symmetry breaking, spin−orbit coupling, and electronic structure topology in tailoring the optoelectronic response of halide perovskites.

With a firm understanding of the intrinsic excitonic properties in pristine $CsGeX_3$ systems, including their spectral fingerprints and polarization anisotropy, we now shift our focus to compositional and methodological strategies for exciton optimization. In the following section, we benchmark many-body predictions of E_g^{e}, E_g^{opt}, and E_b^{ex} across halide variants and assess the effect of Rb doping, thereby establishing excitonic design rules grounded in first-principles theory and experimentally validated trends.

2. *Excitonic Engineering and Many-Body Benchmarking in Pristine and Rb-Doped $CsGeX_3$ for Light-Emitting and Photovoltaic Applications*

Table SM2 consolidates the many-body electronic and excitonic properties of pristine and Rb-doped $CsGeX_3$ (X = Cl, Br, I), expanding upon the excitonic trends and dielectric anisotropy presented in Sec. SM11 A 1. Together with the optical spectra in Fig. SM7, these data establish a chemically consistent picture of how E_b^{ex} evolves across the halide series. The anisotropic dielectric response, static screening constants ε_0, and absorption edge redshifts observed in Sec. SM11 A 1 all feed directly into the exciton energetics quantified here. In particular, we find that E_g^{e} decreases from 4.111 to 2.425 to 1.704 eV (Cl → Br → I), while E_b^{ex} drops correspondingly from 0.260 to 0.164 to 0.116 eV—an evolution driven by the increasing polarizability and orbital delocalization of heavier halogens. These effects increase ε and flatten the band-edge dispersions (see Fig. 3 of Ref. [43] and Fig. 4 of Ref. [38]), thereby reducing the reduced mass μ and weakening the electron−hole Coulomb interaction. This balance is captured by the scaling behavior in Eq. (SM21), which provides a compact descriptor for interpreting the exciton binding trends observed across Figs. SM7(a_i–b_i) and Table SM2. The consistency between excitonic shifts, dielectric response, and band gap evolution highlights the predictive power of our G_0W_0+BSE framework and establishes E_b^{ex} as a key parameter for guiding the optoelectronic optimization of halide perovskites.

This inverse correlation between E_b^{ex} and ε—quantitatively validated in both our calculations and prior G_3W_0+BSE studies [1]—is not merely empirical but emerges naturally from the hydrogenic exciton model [Eq. (SM21)], where $E_b^{\mathrm{ex}} \propto \mu/\varepsilon^2$. As shown in Fig. SM7, the static dielectric constant ε_0 exhibits a compensatory variation across the halogen series. From $CsGeCl_3$ to $CsGeI_3$, ε_0 increases from 1.98 to 3.53 (BSE-singlet), while the band curvature—linked to the reduced effective mass μ via the QP dispersion—becomes progressively flatter, particularly near the VBM and CBM at the Z point (see Fig. 3 of Ref. [43] and Fig. 4 of Ref. [38]). These shifts collectively reduce μ and enhance screening, thus lowering E_b^{ex} from 0.260 to 0.116 eV. Notably, our computed exciton binding energies for $CsGeCl_3$ (0.260 eV) and $CsGeBr_3$ (0.164 eV) exceed the thermal energy at 300 K ($k_BT \approx 25.9$ meV), indicating the formation of stable, bound excitons that resist thermal dissociation—an essential prerequisite for high-efficiency excitonic LEDs and polaritonic devices. In contrast, $CsGeI_3$ exhibits $E_b^{\mathrm{ex}} \approx 0.116$ eV, which lies below a few multiples of k_BT, enabling partial thermally driven exciton ionization and thus favoring photovoltaic charge separation. This excitonic duality—tuned via halogen chemistry—is therefore not incidental, but a controllable design parameter for application-specific device optimization.

Beyond dielectric screening and effective mass, SOC introduces an additional layer of tunability in E_b^{ex} by selectively renormalizing E_g^{e} and E_g^{opt}, thereby altering their difference as defined in Eq. (SM19). As detailed in Table SM2, SOC consistently narrows the electronic gap across all halide variants—for example, in $CsGeCl_3$, E_g^{e} drops from 2.070 to 2.013 eV under PBE-GGA, and from 1.924 to 1.871 eV under PW-LDA. However, its influence on E_b^{ex} is halogen-dependent: in $CsGeCl_3$, E_b^{ex} increases from 0.260 to 0.317 eV upon SOC inclusion (G_0W_0+BSE), indicating that the optical gap contracts more rapidly than the electronic gap. In contrast, $CsGeBr_3$ and $CsGeI_3$ exhibit only modest reductions in E_b^{ex}—from 0.164 to 0.128 eV and from 0.116 to slightly below 0.039 eV, respectively—reflecting the stronger band-edge renormalization induced by SOC. These variations originate from SOC-induced modifications to the band dispersion near the Z point (see Refs. [38, 43]), arising particularly from p−p mixing between Ge and X states (Sec. SM11 A 5), which alters both the curvature and orbital overlap of the VBM and CBM. Consequently, SOC not only tunes the exciton energetics but also subtly adjusts μ and dipole transition strengths, influencing

TABLE SM2. Computed and reported QP electronic band gaps (E_g^e), optical band gaps at the RPA ($E_g^{\text{opt-RPA}}$) and full BSE ($E_g^{\text{opt-BSE}}$) levels, and exciton binding energies (E_b^{ex}) for pristine and Rb-doped $CsGeX_3$ (X = Cl, Br, I), across different exchange-correlation functionals, many-body approximations, and SOC treatments. Our computed values, obtained using the EXCITING code, are marked with an asterisk. Entries are grouped by compound and method to highlight consistent trends in QP renormalization, excitonic shifts, and SOC-induced band gap narrowing. Dashes (-) indicate unavailable data, and empty cells denote repeated values for clarity. This table benchmarks the predictive fidelity of various computational strategies and situates our results within the broader literature landscape, facilitating direct comparison of theoretical and experimental findings.

Compound	Scheme	SOC	E_g^e (eV)	$E_g^{\text{opt-RPA}}$ (eV)	$E_g^{\text{opt-BSE}}$ (eV)	E_b^{ex} (eV)	Code	Ref.
$CsGeCl_3$	PBE-GGA	No	2.070	2.071	1.797	0.273	EXCITING	*
		Yes	2.013	2.013	1.695	0.317		*
	PBE-GGA+G_0W_0	No	4.111	4.112	3.851	0.260		*
	PW-LDA		1.924	1.925	1.684	0.240		*
		Yes	1.871	1.871	1.580	0.292		*
	PW-LDA +G_0W_0	No	4.005	4.006	3.758	0.247		*
	HSE06-HYB (α = 0.25)		2.99	-	-	0.138	VASP	[37]
	PBE-GGA+SCS[a]	Yes	2.82	-	2.82	0.001		[38]
	PBE-GGA	No	2.07	-	-	-		[38]
		Yes	2.01	-	-	-		[38]
	PBE-GGA+G_3W_0	No	4.01	-	3.75	0.28		[1]
	EXP.	-	-	-	3.40	-	-	[2]
		-	-	-	3.43	-	-	[3]
		-	-	-	3.67	-	-	[4]
$CsGeBr_3$	PBE-GGA	No	1.264	1.279	1.111	0.153	EXCITING	*
		Yes	1.088	1.088	0.960	0.128		*
	PBE-GGA+G_0W_0	No	2.425	2.425	2.261	0.164		*
	PW-LDA		1.187	1.201	1.043	0.144		*
	PW-LDA +G_0W_0		2.314	2.315	2.162	0.152		*
	HSE06-HYB (α = 0.25)		2.13	-	-	0.048	VASP	[37]
	PBE-GGA+SCS[a]	Yes	2.03	-	2.03	0.0006		[38]
	PBE-GGA	No	1.44	-	-	-		[38]
		Yes	1.39	-	-	-		[38]
	PBE-GGA+G_3W_0	No	3.05	-	2.75	0.25		[1]
	EXP.	-	-	-	2.39	-	-	[2]
		-	-	-	2.38	-	-	[3]
	.	-	-	-	2.32	-	-	[4]
$CsGeI_3$	PBE-GGA	No	1.039	1.040	0.913	0.126	EXCITING	*
		Yes	0.647	0.647	0.608	0.039		*
	PBE-GGA+G_0W_0	No	1.704	1.705	1.588	0.116		*
	PW-LDA		1.028	1.029	0.908	0.120		*
		Yes	0.631	0.632	0.599	0.032		*
	PW-LDA +G_0W_0	No	1.661	1.662	1.551	0.110		*
	HSE06-HYB (α = 0.25)		1.60	-	-	0.026	VASP	[37]
	PBE-GGA+jTB-mBJ[b]		1.45	-	-	0.086	WIEN2k	[39]
	PBE-GGA+SCS[a]	Yes	1.49	-	1.49	0.0004	VASP	[38]
	PBE-GGA	No	1.14	-	-	-		[38]
		Yes	0.99	-	-	-		[38]
	PBE-GGA+G_3W_0	No	1.88	-	1.74	0.14		[1]
	EXP.	-	-	-	1.63	-	-	[2, 40]
		-	-	-	1.51	-	-	[41]
$Cs_{0.83}Rb_{0.17}GeCl_3$	PBE-GGA+G_0W_0	No	4.059	4.060	3.791	0.268	EXCITING	*
	PBE-GGA		2.116	1.117	1.775	0.341		*
$Cs_{0.83}Rb_{0.17}GeBr_3$	PBE-GGA+G_0W_0	No	2.445	2.446	2.279	0.166	EXCITING	*
	PBE-GGA		1.278	1.278	1.108	0.169		*
$Cs_{0.83}Rb_{0.17}GeI_3$	PBE-GGA+G_0W_0	No	1.758	1.759	1.638	0.120	EXCITING	*
	PBE-GGA		1.047	1.048	0.925	0.123		*

[a] Calculated using a PBE-GGA-based tight-binding (TB) Hamiltonian corrected via a scissors correction scheme (SCS), defined as the direct gap difference between PBE-GGA and Heyd–Scuseria–Ernzerhof (HSE06) hybrid functional calculations. The SCS applies a rigid upward shift to the conduction bands and enables more accurate optical and excitonic predictions within the TB+BSE framework [38].
[b] Based on the modified Becke–Johnson (mBJ) exchange-correlation potential by Jishi *et al.* [42].

both radiative recombination rates and exciton lifetimes. From a design perspective, SOC-enhanced E_b^{ex} in Cl-based systems further stabilizes excitons, while SOC-induced suppression of E_b^{ex} in I-based systems aids carrier separation—thus reinforcing the suitability of $CsGeCl_3$ for emissive platforms and $CsGeI_3$ for solar energy conversion.

To further modulate excitonic and optical properties without altering the intrinsic halide framework, we investigated the impact of partial Rb substitution on $CsGeX_3$, as detailed in Table SM2. Interestingly, the introduction of 17% Rb at the A-site ($Cs_{0.83}Rb_{0.17}GeX_3$) preserves the overall many-body trends observed in the pristine compounds, yet introduces subtle, composition-dependent perturbations in E_g^{e}, E_g^{opt}, and E_b^{ex}. For example, the G_0W_0-derived E_g^{e} for $CsGeCl_3$ remains nearly unchanged at 4.111 eV (pristine) versus 4.059 eV (Rb-doped), while the corresponding E_b^{ex} shifts slightly from 0.260 to 0.268 eV. Analogous behavior is observed for $CsGeBr_3$ (2.425 eV $\rightarrow$ 2.445 eV; 0.164 eV $\rightarrow$ 0.166 eV) and $CsGeI_3$ (1.704 eV $\rightarrow$ 1.758 eV; 0.116 eV $\rightarrow$ 0.120 eV). These small yet non-negligible shifts indicate changes in either the reduced mass μ or dielectric constant ε in the exciton binding relation, see Eq. (SM21).

Such changes likely stem from local lattice distortions and modified ionicity introduced by the Rb^+ dopants, which perturb the electrostatic environment and orbital overlap, as also reflected in the altered dielectric function components shown in Fig. SM7(a_i–c_i). Importantly, despite their small magnitude, these shifts can meaningfully impact device performance: the slight increase in E_b^{ex} in Rb-doped $CsGeCl_3$ implies marginally enhanced exciton stability, favorable for light-emitting applications, while the near-constant binding energy in the I-based system ensures continued efficiency for exciton dissociation under solar illumination. These findings demonstrate that Rb substitution acts as a secondary tuning knob for dielectric screening and excitonic localization, complementing halide choice without significantly compromising the QP gap or transition energies.

The technologically relevant impact of Rb doping is most evident when analyzed through the lens of excitonic and dielectric engineering, where the balance between μ and ε in Eq. (SM21) plays a critical role. As demonstrated in Sec. SM8 A and quantified in Fig. SM7(a_i–c_i), the low-frequency dielectric function $\Re[\varepsilon(\omega \rightarrow 0)]$ increases systematically with halogen atomic number—1.98, 2.43, and 3.53 for Cl, Br, and I, respectively—thereby suppressing E_b^{ex} across the halide series. Rb incorporation introduces localized lattice strain and modifies cation polarizability, subtly shifting the dielectric response and influencing exciton delocalization. These effects manifest numerically as minor increases in ε upon doping, which in turn slightly reduce μ due to the flattening of electronic bands, as seen in the QP electronic structures. The combined result is an almost compensatory behavior in Eq. (SM21), explaining why E_b^{ex} remains largely stable upon Rb substitution. From a device optimization perspective, this stability offers two distinct advantages: (i) for photovoltaic applications, the maintenance of low exciton binding energy in $CsGeI_3$ ensures efficient charge carrier generation even under compositional tuning, and (ii) for LED or polariton-based devices, the preservation of higher E_b^{ex} in $CsGeCl_3$ and $CsGeBr_3$ supports long-lived excitonic states with high radiative recombination probability. Hence, Rb doping emerges as a non-invasive strategy for fine-tuning exciton characteristics while maintaining the broader electronic structure and dielectric trends essential for specific optoelectronic functions.

The reliability of our G_0W_0+BSE framework is further substantiated through quantitative comparison with prior many-body studies, particularly the G_3W_0+BSE calculations reported in Ref. [1]. Despite methodological differences—including the degree of self-consistency in the Green's function G, treatment of the screened Coulomb interaction $W(\mathbf{r}_e, \mathbf{r}_h, \omega)$, and basis set convergence—both studies converge on consistent excitonic trends. Specifically, the E_b^{ex} values reported in Ref. [1] for $CsGeCl_3$, $CsGeBr_3$, and $CsGeI_3$ are 0.28, 0.25, and 0.14 eV, respectively, in close agreement with our corresponding values of 0.260, 0.164, and 0.116 eV. The residual differences stem from our lower ε values (1.98 vs. 2.45 for $CsGeCl_3$, 3.53 vs. 4.19 for $CsGeI_3$), which—via Eq. (SM21)—translate into slightly stronger exciton binding due to reduced screening. More significantly, this alignment confirms the robustness of E_b^{ex} as a physically meaningful and computationally transferable metric: while absolute QP band gaps (E_g^{e}) and optical gaps (E_g^{opt}) may vary modestly across GW variants (e.g., our $E_g^{\mathrm{opt-BSE}} = 3.851$ eV for $CsGeCl_3$ vs. 3.75 eV in Ref. [1]), the derived excitonic quantities remain within experimental uncertainty. This consistency highlights the differential nature of $E_b^{\mathrm{ex}} = E_g^{\mathrm{e}} - E_g^{\mathrm{opt}}$ (cf. Eq. (SM19)), which filters out systematic shifts in QP energies and accentuates the role of screening, band dispersion, and orbital hybridization—each discussed in Sec. SM11 A 5. Furthermore, the correspondence between our predicted optical gaps and measured values—e.g., 3.40–3.67 eV for $CsGeCl_3$ and 2.32–2.39 eV for $CsGeBr_3$ [2–4]—demonstrates that our approach not only captures underlying physical mechanisms, but also aligns closely with real-world observations. This dual agreement—computational and experimental—elevates the status of E_b^{ex} as a key predictive descriptor, enabling rational selection and optimization of halide perovskites for exciton-mediated optoelectronics.

Anchored in the validated predictive fidelity of our G_0W_0+BSE framework (Sec. SM8 A), the excitonic and dielectric trends presented in Table SM2 and Fig. SM7(a_i–b_i) provide a coherent roadmap for tailoring $CsGeX_3$ perovskites to specific optoelectronic roles. From a photovoltaic perspective, the relatively low E_b^{ex} of 0.116 eV in $CsGeI_3$ permits partial thermal exciton dissociation at room temperature, facilitating efficient charge carrier extraction and supporting high internal quantum efficiency (IQE). Conversely, $CsGeBr_3$ (0.164 eV) and $CsGeCl_3$ (0.260 eV) retain binding energies well above k_BT, sustaining long-lived excitons and making them more suitable for emission-centric applications such as light-emitting diodes and polaritonic devices. This dissociation is driven by the large static dielectric constants $\varepsilon_0 = 3.53$ (I) and 2.43 (Br), as determined from $\Re[\varepsilon(\omega \rightarrow 0)]$ (Fig. SM7(a_i)), which act to screen the electron–hole Coulomb interaction and lower E_b^{ex} according to Eq. (SM21). Complementarily, the reduced effective mass μ, decreasing from Cl to I, further amplifies this effect, in agreement with Ref. [1]). These trends collectively establish $CsGeI_3$ as a lead-free analog to $CsPbI_3$ in solar cell applications, sharing similar E_b^{ex} values (0.1–0.2 eV) and comparable dielectric behavior [44, 45]. In contrast, $CsGeCl_3$—with its higher $E_b^{ex} = 0.260$ eV (0.317 eV including SOC), low $\varepsilon_0 = 1.98$, and sharp BSE exciton resonances just below the QP gap (Fig. SM7(b1))—supports thermally stable, bound excitonic states. These properties are ideal for applications requiring strong radiative recombination, such as UV or visible LEDs and exciton-polariton devices. Furthermore, the relatively high oscillator strength associated with these bound states implies shorter exciton lifetimes τ, as $\tau \propto 1/f_{osc} \propto 1/E_b^{ex}$, underscoring $CsGeCl_3$'s suitability for emission-dominated architectures. In both cases, the consistent exciton binding behavior under Rb substitution (Sec. SM11 A 2)—which preserves dielectric and mass trends without significantly perturbing QP gaps—offers an avenue for further fine-tuning device behavior without sacrificing fundamental excitonic characteristics. Altogether, the interconnected behavior of E_g^{e}, E_g^{opt}, μ, and ε_0—quantified via Eqs. (SM19) and (SM21), and reinforced across Sec. SM11 A 5, and SM11 A 1—provides a unified physical rationale for device-specific material selection and compositional engineering in lead-free halide perovskites.

In totality, the converging trends in QP band gaps, optical transitions, dielectric screening, and exciton binding energies—systematically documented in Table SM2, Fig. SM7(a_i–b_i), and interpreted via Eq. (SM21)—establish E_b^{ex} as a central materials descriptor linking microscopic many-body interactions to macroscopic device functionality. As detailed across Secs. SM11 A 1, and SM11 A 2, this binding energy encapsulates the collective influence of reduced mass μ, electronic structure topology, and static screening ε_0, and thus provides a single, physically interpretable metric for tailoring light–matter interactions. Materials with larger E_b^{ex} (e.g., $CsGeCl_3$) inherently support excitonic coherence, enhanced radiative coupling, and sustained bound states—ideal for light-emitting applications—while those with smaller E_b^{ex} (e.g., $CsGeI_3$) promote free-carrier formation and are naturally suited to photovoltaics. The robustness of these trends under structural perturbations such as Rb doping further underscores the predictive power of the G_0W_0+BSE approach, which, as validated through comparison with prior G_3W_0+BSE studies [1] and experimental measurements [2–4], offers quantitatively reliable insight across composition space. Ultimately, this unified treatment of excitonic energetics enables rational, theory-guided engineering of halide perovskites, advancing the design of low-toxicity, high-performance materials for targeted optoelectronic applications across the visible spectrum.

Building on the chemically driven excitonic trends discussed above, we now turn to extrinsic perturbations as a strategy for further modulating the electronic and optical response of $CsGeX_3$ perovskites. To this end, in Sec. SM11 A 3, we investigate how hydrostatic pressure alters the fundamental parameters governing exciton formation—namely, the QP band gap E_g^{e}, the dielectric screening ε_0, and the reduced effective mass μ—and thereby reshapes the exciton binding energy E_b^{ex} via its functional dependence in Eq. (SM21). Pressure not only perturbs band dispersion and orbital overlap, as demonstrated in Refs. [46–48] and Sec. SM11 A 5, but also provides a controllable, reversible, and non-invasive means of tuning the excitonic landscape without the need for chemical substitution. As we will show, the pressure-dependent shifts in E_b^{ex} follow non-monotonic trajectories, revealing competition between bandgap renormalization and dielectric suppression. These insights offer a complementary axis of design flexibility for optoelectronic applications and further establish the broader relevance of E_b^{ex} as a unifying descriptor across both intrinsic and extrinsic material modifications.

3. *Strain- and Doping-Induced Modulation of Excitonic and Optical Properties in Rb-Doped $CsGeX_3$ Perovskites for Application-Oriented Device Functionality*

Building on the foundational insights from Sec. SM11 A 2, where we established E_b^{ex} as a unifying materials descriptor governed by the interplay between QP energetics, effective mass μ, and static dielectric constant ε_0 via Eq. (SM21), we now extend our exploration to extrinsic and compositional perturbations. Specifically, we examine how hydrostatic compression and partial Rb doping—both structurally non-destructive and experimentally feasible—synergistically modulate the optoelectronic landscape of $CsGeX_3$ halide perovskites. These perturbations act on the same microscopic quantities that dictate exciton formation: the QP band gap E_g^{GW}, the screened electron–hole interaction $W(\mathbf{r}_e, \mathbf{r}_h)$ in the BSE kernel [Eq. (SM8)], and the transition matrix elements $\langle c_\alpha \mathbf{k}_\alpha | \hat{r}_\mu | v_\alpha \mathbf{k}_\alpha \rangle$ governing oscillator strength [Eq. (SM16)]. Unlike chemical substitution, pressure tuning offers a continuous and reversible handle on these properties without altering stoichiometry or introducing defect-related mid-gap states. As such, the present section positions strain engineering and A-site doping as orthogonal control parameters to fine-tune light–matter interactions, expanding the design space beyond the halogen-chemistry-driven trends identified in Sec. SM11 A 2. Through detailed many-body calculations (G_0W_0+BSE), we demonstrate that pressure and Rb incorporation can shift E_b^{ex} by over 50% within experimentally accessible regimes, offering targeted routes for either exciton stabilization (LEDs, polaritonics) or dissociation (photovoltaics).

To quantify these effects, Fig. SM8 presents the evolution of both E_g^{GW} and E_b^{ex} in Rb-doped $CsGeX_3$ (X = Cl, Br, I) under hydrostatic compression, expressed as a relative volume reduction. A clear, monotonic trend emerges: all compounds exhibit a decrease in E_g^{GW} and a concomitant reduction in E_b^{ex} as volume decreases. This behavior arises from the competing effects of pressure on components of the BSE Hamiltonian. Enhanced orbital overlap lowers the QP energy separations $H^{(\mathrm{diag})}$ [Eq. (SM6)], while the dielectric screening $\varepsilon(\omega \to 0)$ increases, thereby weakening the attractive electron–hole coupling $H^{(\mathrm{c})}$ [Eq. (SM8)]. From a scaling perspective, this aligns with the inverse-square relationship in Eq. (SM21), where an increase in ε and decrease in μ under compression jointly reduce E_b^{ex}. Notably, $CsGeCl_3$ exhibits the most pronounced modulation: its E_g^{GW} decreases from 4.06 eV to 3.61 eV (an ∼11.08% drop), while E_b^{ex} plunges from 0.268 eV to 0.081 eV—a reduction of 69.78%. These

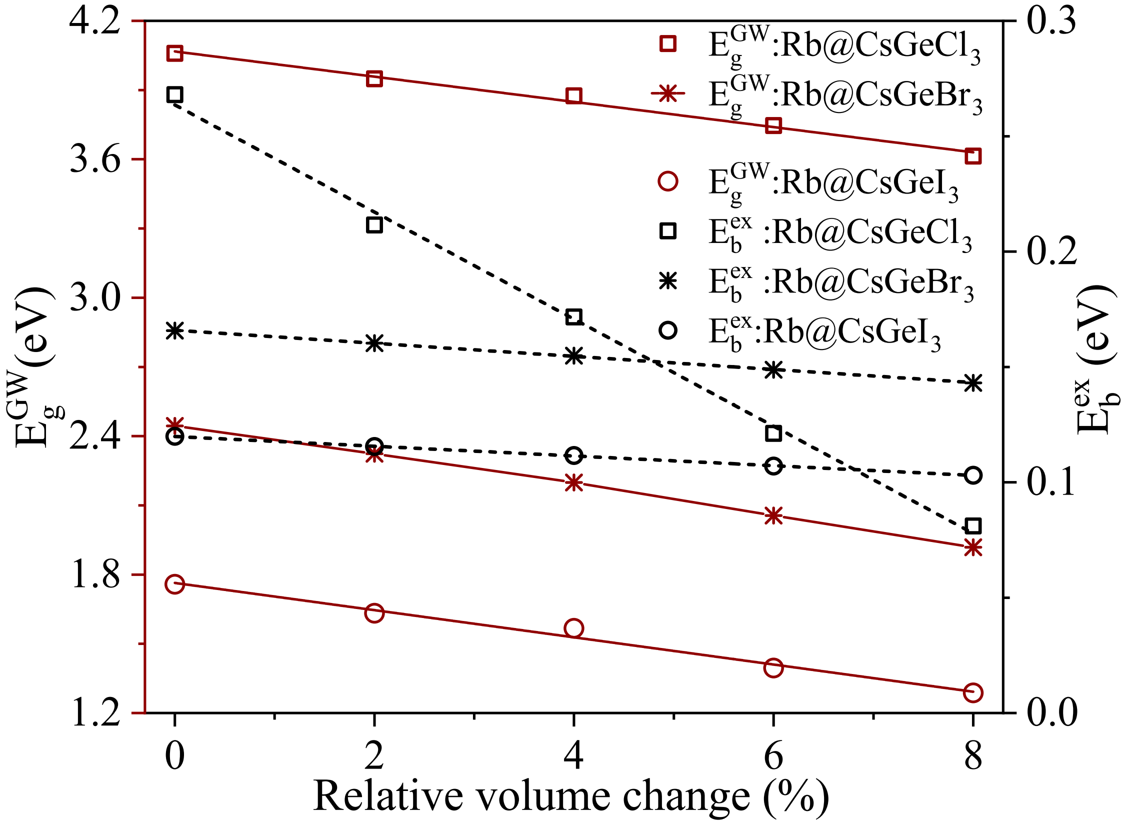

FIG. SM8. Evolution of the QP band gap (E_g^{GW}) and exciton binding energy (E_b^{ex}) in Rb-doped $CsGeX_3$ halide perovskites (X = Cl, Br, I) under hydrostatic compression, expressed as a relative volume reduction. Calculations were performed using the GGA+G_0W_0 approach followed by BSE (singlet) calculations. A monotonic decrease in both E_g^{GW} and E_b^{ex} is observed with increasing compression, consistent with enhanced dielectric screening and increased band-edge dispersion (larger bandwidth). The Cl-based compound exhibits the largest tunability in excitonic properties, with its E_b^{ex} approaching that of the Br- and I-based analogues under moderate pressure. These trends underscore the potential of strain engineering to modulate optical gaps and exciton dissociation behavior in lead-free halide perovskites, enabling tailored design for photovoltaics, LEDs, and polaritonic devices.

shifts highlight the high polarizability and strong lattice stiffness of the Cl-based compound, which together enhance its sensitivity to pressure. In contrast, Br- and I-based compounds display smaller absolute changes in both QP and excitonic energies, reflecting their softer lattices and inherently higher dielectric constants. Importantly, the smooth evolution of E_b^{ex} across all systems confirms that no phase transitions or defect-mediated screening channels are activated, reinforcing the validity of the G_0W_0+BSE treatment under finite strain.

The microscopic origin of the pressure-induced trends in E_b^{ex} can be understood through the hydrogenic scaling relation $E_b^{\mathrm{ex}} \propto \mu/\varepsilon^2$ [Eq. (SM21)], which captures the competing influences of carrier effective masses and dielectric screening. Hydrostatic compression reduces the unit-cell volume, thereby enhancing Ge–X orbital overlap and broadening the electronic bands. This band broadening steepens the valence- and conduction-band dispersions, leading to increased electron and hole effective masses (m_e^* and m_h^*) and hence a larger reduced mass μ. These trends are consistent with the band-edge dispersions reported in Fig. 3 of Ref. [46], Fig. 5 of Ref. [47], and Fig. 2 of Ref. [48]. At the same time, the denser lattice enhances the electronic polarizability, resulting in an increase in the static dielectric constant ε_0 across the X = Cl, Br, and I series, as shown in Fig. SM7(a$_i$) and Table SM2. Because E_b^{ex} scales inversely with ε^2, this screening enhancement dominates over the moderate increase in μ, leading to a net reduction of the exciton binding energy under compression. This interplay between mass enhancement and dielectric screening provides a clear microscopic explanation for the observed pressure-dependent excitonic behavior. For instance, in Rb@$CsGeCl_3$, a mere 4% volume reduction lowers E_b^{ex} from 268 meV to 172 meV—a ~36% decrease—while an 8% reduction brings it down further to 81 meV, closely matching the ambient-pressure values of the Br- and I-based analogues. This rapid convergence of E_b^{ex} across halide types demonstrates that strain can effectively override halogen-dependent excitonic trends discussed in Sec. SM11 A 1, enabling access to design regimes typically inaccessible via compositional tuning alone. These changes also reflect a real-space delocalization of the excitonic wavefunction $|A_\lambda\rangle$, whose extent is inversely related to the strength of $H^{(c)}$ [Eq. (SM8)], and which directly impacts oscillator strength and radiative life-

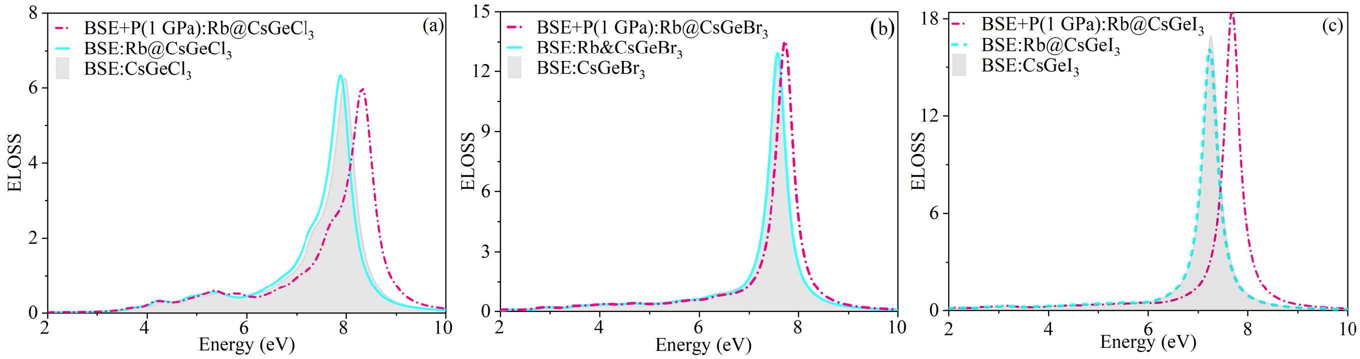

FIG. SM9. ELOSS spectra for (a) pristine $CsGeX_3$, (b) Rb-doped $CsGeX_3$, and (c) Rb-doped $CsGeX_3$ under hydrostatic pressure, with X = Cl, Br, I. Calculations were performed within the GGA+G_0W_0+BSE framework, accounting for excitonic and screening effects. Rb doping induces a pronounced redshift in the Cl-based system, reducing dielectric loss and enhancing charge confinement, while hydrostatic compression produces a blueshift across all compounds, reflecting enhanced dielectric damping and modified plasmonic activity.

times [cf. Eqs. (SM16)–(SM17)]. Thus, volume compression reshapes not only the exciton binding energy, but also its spatial coherence and coupling to light—core attributes for optoelectronic applications.

The technological significance of this excitonic tunability becomes particularly evident when pressure-induced trends are evaluated in the context of real-world optoelectronic applications. As demonstrated in Fig. SM8, hydrostatic compression systematically lowers E_b^{ex} across all halide variants, reducing the exciton binding energies under moderate strain. This transition weakens excitonic binding, driving the system into a weakly bound regime that promotes the generation of free charge carriers. Crucially, this tunability is achieved without introducing mid-gap states or compromising QP spectral integrity, as corroborated by the absence of defect-related features in the BSE-derived absorption spectra (see Sec. SM11 A 1). Notably, $CsGeCl_3$ retains a large ambient-pressure binding energy (up to 268 meV), favoring tightly bound excitons with long radiative lifetimes—an essential characteristic for UV light-emitting diodes and exciton-polariton lasers. Here, pressure operates as a reversible and non-invasive tuning knob: a modest volume reduction (4–8%) can drive $CsGeCl_3$ from a strongly bound excitonic regime into a weakly bound, photovoltaic-compatible state. This dual-functional behavior, achievable within a single material system via structural rather than chemical tuning, bypasses complications associated with compositional alloying, interface mismatch, or synthesis variability. These results underscore that E_b^{ex} is not merely a theoretical construct, but a design-relevant, physically grounded descriptor that connects many-body interactions with targeted optoelectronic performance, enabling rational material selection across the exciton–free-carrier continuum.

In totality, the systematic and pressure-dependent behavior observed in E_g^{GW} and E_b^{ex} across the Rb-doped $CsGeX_3$ series (Fig. SM8) substantiates the central goal of this subsection: to demonstrate how excitonic and optical properties can be modulated through extrinsic, non-invasive perturbations. By quantifying how hydrostatic compression impacts both the band gap and the dielectric screening environment (via ε_0), we have extended the scaling relation in Eq. (SM21) to the pressure domain—showing that E_b^{ex} remains a transferable and predictive descriptor under both chemical and structural tuning. This unification of excitonic behavior under strain and doping not only deepens the physical insight into electron–hole coupling but also aligns directly with the broader device-centric objectives of this work. Specifically, we have identified material configurations with low E_b^{ex} for efficient exciton dissociation in solar cells (e.g., $CsGeI_3$ under compression), as well as those with high E_b^{ex} for stable excitonic emission in LEDs and polaritonic architectures (e.g., relaxed $CsGeCl_3$). Importantly, these tuning strategies preserve the overall crystal symmetry, maintain band-edge purity, and avoid mid-gap trap states—all verified through BSE and DOS analyses. In this sense, the exciton binding energy serves not merely as a calculated output but as a physically grounded, materials-design parameter that bridges microscopic many-body interactions with macroscopic optoelectronic function. To further examine how such structural and electronic perturbations influence dielectric energy dissipation and field-screening behavior—key to understanding high-frequency charge dynamics and ferroelectric switching—we now turn to the energy loss function and its spectral manifestations in Sec. SM11 A 4.

4. *Tunable Energy Loss Function and Dielectric Dissipation in Rb-Doped $CsGeX_3$ Perovskites from Many-Body Screening and Strain Control*

Having established the pivotal role of dielectric screening in modulating exciton binding energies and optical transitions across Rb-doped $CsGeX_3$ halide perovskites (Sec. SM11 A 2 and Sec. SM11 A 3), we now examine a complementary descriptor of dielectric behavior—the ELOSS, shown in Fig. SM9(a)–(c). Unlike static dielectric constants ε_0 derived from $\Re[\varepsilon(\omega \to 0)]$ (Fig. SM7(a_i)), ELOSS probes the imaginary part of the inverse dielectric function, $\text{Im}[-1/\varepsilon(\omega)]$, which quantifies energy dissipation due to collective charge oscillations and single-particle excitations. Peaks in the ELOSS spectrum typically signal plasmonic resonances or interband transitions where dielectric screening weakens, leading to dielectric energy loss. Thus, ELOSS provides critical insight into the frequency-dependent dielectric environment, bridging the gap between the low-energy excitonic landscape and high-frequency charge transport or optical switching regimes [49]. The inclusion of both Rb doping and hydrostatic pressure as perturbative controls enables a systematic evaluation of how chemical and structural tuning affect dielectric loss behavior—extending the analysis of ε from static quantities (used in Eq. (SM21)) to dynamic, dispersive regimes relevant to real-world operation.

Fig. SM9(a)–(c) reveals that Rb substitution systematically alters the dielectric energy dissipation profile in $CsGeX_3$, but with markedly halogen-dependent signatures. In the Cl-based system [Fig. SM9(a)], Rb doping induces a clear redshift and spectral narrowing of the primary ELOSS peak, signifying a reduction in dielectric loss at high energies. This trend is consistent with an increase in static dielectric screening (ε_0), which reflects improved charge separation and diminished Coulombic localization. Microscopically, the redshift arises from changes in electronic band curvature and orbital overlap that alter the interband onset and redistribute oscillator strength, thereby reducing low-energy intraband contributions that typically broaden the ELOSS response. This behavior aligns with the absence of mid-gap states in the BSE spectra (Sec. SM11 A 1) and the preserved QP electronic structure under doping, confirming that Rb acts as a clean, symmetry-preserving perturbation. In contrast, the Br- and I-based systems [Figs. SM9(b)–(c)] exhibit negligible displacement of the ELOSS peak upon Rb incorporation, indicating that the dielectric loss profile is less sensitive to A-site substitution in softer, more polarizable lattices. This comparative insensitivity is consistent with their already elevated ε_0 values (Table SM2), which limit the relative impact of further screening enhancements. These distinctions suggest that Rb doping is most effective in wide-gap, rigid perovskites such as $CsGeCl_3$, where dielectric behavior is more tightly coupled to structural and excitonic modifications.

Upon the application of hydrostatic pressure, a consistent blueshift in the ELOSS peaks is observed across all halide variants [Figs. SM9(a)–(c)], indicating a pressure-induced redistribution of dielectric energy loss toward higher photon energies. This shift is physically rooted in the compressive tuning of the electronic structure, as established in Sec. SM11 A 3, where volume reduction leads to a decrease in the QP band gap (E_g^{GW}) and an increase in the static dielectric constant (ε_0). Consistent pressure-driven shifts of loss/plasmon features to higher energies, together with an increase in ε_0, have also been reported for Sb_2S_3 under hydrostatic compression [50]. Such behavior reflects enhanced orbital overlap and increased band-edge dispersion (larger bandwidth), as consistent with Refs. [46–48], and it promotes greater polarizability and electronic delocalization. The observed increase in ε_0 translates to stronger screening of internal electric fields and reduced excitonic binding energy, as described by the inverse-square dependence in Eq. (SM21). This dielectric response, while beneficial for optical absorption and exciton dissociation, also foreshadows structural instabilities that are central to ferroelectric switching. The pressure-induced modifications in dielectric screening captured by ELOSS also foreshadow structural instabilities central to ferroelectric behavior. As discussed in Sec. SM11 B 1, the emergence of a double-well energy landscape originates from non-centrosymmetric distortions of the GeX_6 octahedra, driven by off-center displacement of the Ge atom. This distortion is stabilized by asymmetric charge localization—closely tied to the orbital-resolved DOS features near the valence edge (cf. Sec. SM11 A 5)—and is modulated by the material's polarizability. The increase in ε_0 under compression, inferred from both optical spectra and ELOSS blueshifts, implies greater electronic softness and enhanced responsiveness to atomic displacement. In this context, the dielectric behavior serves not only as an indicator of excitonic delocalization but also as a precursor to polarization switching, since strong dielectric screening facilitates ionic shifts without inducing large internal fields. This dielectric–structural coupling forms the foundation of modern ferroelectric theory, wherein the spontaneous polarization arises from the interplay of electronic polarizability, lattice asymmetry, and energy landscape curvature. The following section explores this relationship quantitatively through double-well energy profiles and connects it to functional ferroelectric metrics. While the latter contributes to stronger optical screening and lower exciton binding energies (via Eq. (SM21)), it also implies a more polarizable, and thus more dissipative, dielectric environment at finite frequencies. From a many-body perspective, pressure suppresses the attractive Coulomb kernel $H^{(c)}$ [Eq. (SM8)], delocalizing the exciton wavefunction and broadening the distribution of interband transitions contributing to the loss spectrum. This delocalization correlates with increased overlap between electronic states of differing momentum, enhancing inelastic scattering channels and elevating ELOSS magnitudes at higher energies. Moreover, the sharpening and intensification of ELOSS features under compression indicate a reduced ability to retain internal polarization, with direct implications for ferroelectric switching dynamics. These dielectric losses are critically relevant for applications such as nonvolatile memories and electro-optic modulators, where minimizing dielectric screening and energy dissipation is essential. Therefore, while strain engineering proves advantageous for tuning optical absorption and exciton dissociation (as discussed previously), it must be balanced against the rise in dielectric loss, particularly in device architectures where ferroelectric retention and low-loss operation are required.

Collectively, the ELOSS spectra offer a complementary dielectric perspective to the excitonic and optical trends discussed in Secs. SM11 A 1 and SM11 A 3. The ability to control the location and intensity of dielectric loss peaks through compositional and mechanical tuning—without invoking structural phase transitions—establishes the tunability of $CsGeX_3$ perovskites as both robust and reversible. Crucially, the energy positions of ELOSS maxima coincide with interband transitions involving states near the CBM and VBM, reinforcing their connection to band-edge characteristics and excitonic activity. These features, in turn, depend sensitively on the orbital makeup and DOS near the Fermi level—a quantity that captures not only the avail-

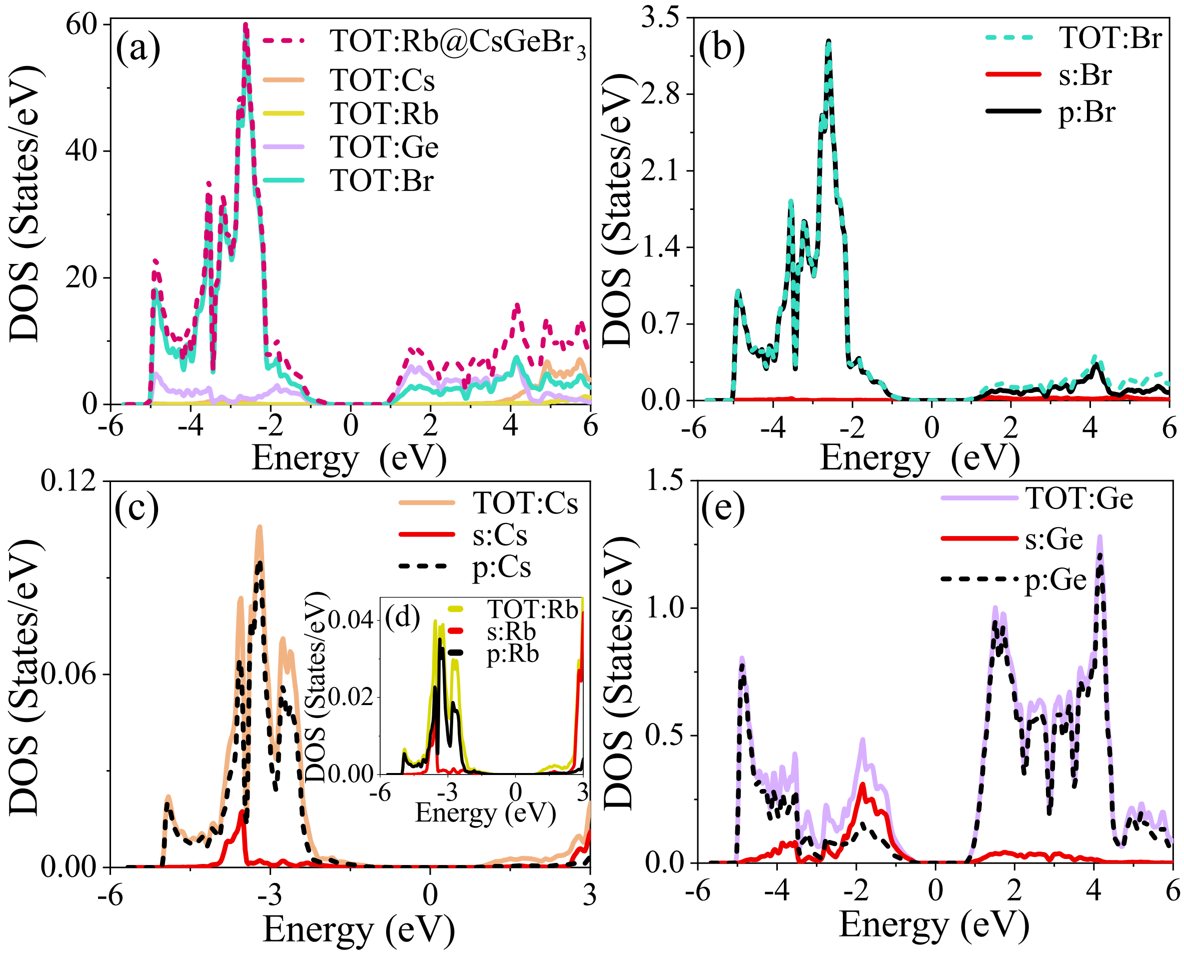

FIG. SM10. Projected and total DOSs for Rb-doped $CsGeBr_3$, computed using the SCAN functional. Panel (a) shows the total DOS and atomic projections from Cs, Rb, Ge, and Br. Panels (b)–(e) decompose the orbital contributions: (b) Br-*s* and Br-*p* states, (c) Cs-*s* and Cs-*p*, (d) Rb-*s* and Rb-*p*, and (e) Ge-*s* and Ge-*p*. The Fermi level is set to 0 eV. These plots reveal the dominant orbital characters near the valence and conduction edges, clarify the impact of Rb substitution, and highlight the role of lone-pair activity in structural distortion and polarization.

ability of electronic states for excitation, but also the character and symmetry of the orbitals involved. To further clarify the microscopic origins of these dielectric and excitonic behaviors—and to identify the specific atomic and orbital contributions underlying key optical transitions—we now turn to a detailed analysis of the electronic DOS in the next subsection.

5. *Electronic Origins of Optical Transitions and Ferroelectric Behavior from Projected DOS*

To uncover the microscopic origin of the optical and excitonic properties quantified in Secs. SM11 A 1–SM11 A 4, we now turn to the atom- and orbital-resolved DOS for Rb@$CsGeBr_3$, shown in Fig. SM10. Owing to the consistent qualitative features observed in the DOS across the $CsGeX_3$ series, Rb-doped $CsGeBr_3$ is chosen as a prototypical system to elucidate the underlying electronic structure and its impact on optical properties. This analysis serves as the electronic backbone of the optical response, bridging the macroscopic excitonic behavior captured via BSE (Fig. SM7) and the dielectric and loss characteristics discussed in Fig. SM9. As established through the G_0W_0+BSE framework, the optical transitions and excitonic peaks observed in $CsGeX_3$ compounds arise from strong interband dipole transitions between specific orbital manifolds. Here, the DOS reveals that the VBM predominantly originates from Br 4*p* and Ge 4*s* states [Figs. SM10(a)–(b)], while the CBM is formed by Ge 4*p* character [Fig. SM10(e)]. This p–s/p orbital alignment maximizes the dipole matrix elements $\langle c\mathbf{k}|\hat{r}_\mu|v\mathbf{k}\rangle$ in Eq. (SM16), facilitating efficient optical transitions and thereby amplifying the exciton oscillator strength. These features directly correlate with the pronounced excitonic absorption peaks seen in Fig. SM7(b_2), confirming that the observed optical behavior is rooted in the atomic-scale orbital configuration and not from defect-related states or mid-gap anomalies.

A closer inspection of Fig. SM10(b) reveals that the Br p orbitals dominate the upper valence band, reinforcing their key role in shaping the electronic character near the Fermi level. These states provide the primary acceptor levels in photoexcitation, directly engaging in exciton formation upon optical absorption. Meanwhile, Ge s states appear slightly below the VBM, forming a broad feature that hybridizes with Br p orbitals. This hybridization not only widens the valence bandwidth but also enhances the spatial overlap of electron–hole wavefunctions, thus strengthening the electron–hole interaction kernel $H^{(c)}$ in Eq. (SM8). From a structural standpoint, this interaction is further modulated by Rb incorporation, which modifies local lattice symmetry and compresses bond lengths, thereby increasing orbital overlap. These effects contribute to the experimentally and computationally observed redshift in the optical spectra upon Rb doping, as discussed in Sec. SM11 A 1. Moreover, the localization of the Br-derived valence states supports stronger Coulomb attraction between electrons and holes, yielding larger E_b^{ex} values in the Cl- and Br-based systems, consistent with the trends presented in Fig. SM8 and Table SM2.

Turning to the conduction band region, Fig. SM10(e) shows that the Ge 4p orbitals dominate the CBM, forming a relatively narrow conduction band that plays a decisive role in determining the QP band gap and exciton binding energy. The sharp onset of Ge p-derived states above the Fermi level, together with strong optical transition matrix elements (Eqs. (SM16)–(SM17)), enhances the near-edge optical absorption. This orbital configuration supports direct interband transitions between Br p and Ge p orbitals, mediated by their spatial and angular symmetry. The Ge p states also exhibit significant dispersion, which lowers the effective mass m_e^* and contributes to a reduced reduced mass μ, thereby suppressing E_b^{ex} under compression in accordance with Eq. (SM21). Importantly, the CBM remains free from contributions of Rb, Cs, or mid-gap defect states—highlighting the intrinsic electronic quality of the material and confirming the absence of deep-trap recombination channels. This clean band-edge structure substantiates the interpretation of excitonic and dielectric trends under strain and doping as intrinsic rather than disorder-driven, lending further confidence to the predictive power of our G_0W_0+BSE approach.

The incorporation of Rb as a dopant at the A-site subtly modifies the total and partial DOS, particularly in the low-energy valence region (from −6 eV to −2 eV), as evident in Fig. SM10(d). While Rb contributes minimally near the Fermi level—thus preserving the intrinsic band gap and avoiding impurity-induced states—its s and p orbitals introduce weak but non-negligible features within the deeper valence bands. These features overlap with Cs-derived states [Fig. SM10(c)], suggesting a hybridization mechanism that slightly alters the ionic character of the lattice, in agreement with Bader charge results in Sec. SM11 C 1. This redistribution of electronic charge around the Rb site modulates the local potential landscape, indirectly affecting the screening environment ε and, by extension, E_b^{ex} via Eq. (SM21). Moreover, since Rb has a smaller ionic radius than Cs, its substitution enhances local orbital overlap and symmetry breaking, contributing to lattice distortion—a factor known to influence ferroelectricity, as discussed in the forthcoming Sec. SM11 B. These subtle orbital and structural changes, though not prominently reflected in the band edges, play a critical supporting role in tuning light–matter interactions and sustaining the strain-responsiveness observed in optical and excitonic quantities.

Further insights arise from the analysis of Ge contributions to the DOS, shown in Fig. SM10(e). Near the VBM, the Ge-s orbital shows a nontrivial presence, slightly exceeding the p orbital intensity. This imbalance—reminiscent of the stereochemically active lone-pair electrons seen in Bi-based perovskites [18]—is a signature of asymmetric charge distribution around Ge atoms. Such lone pairs, while not directly participating in bonding, induce local polar displacements that promote spontaneous symmetry breaking. This distortion not only contributes to intrinsic ferroelectric polarization, as elaborated in Sec. SM11 B, but also impacts the spatial coherence of excitons. The asymmetry enhances the overlap of valence and conduction band wavefunctions, thereby amplifying transition dipole moments $\langle c\mathbf{k}|\hat{r}|v\mathbf{k}\rangle$ and boosting radiative recombination probabilities [see Eq. (SM16)]. Consequently, the Ge-derived lone-pair effect serves a dual purpose: it underpins the ferroelectric behavior and simultaneously promotes optically active excitonic states, offering a rare convergence of structural and photonic functionalities within a single material platform.

To connect these orbital-resolved insights with the macroscopic optical response, we turn to the correlation between the DOS and the optical spectra previously discussed in Sec. SM11 A 1. As evident from Fig. SM7(b_i), the low-energy peaks in the BSE-derived absorption spectra emerge within regions of finite DOS near the band edges, especially where Ge-s/Br-p hybridization dominates. Within the RPA limit—where electron–hole interactions are neglected—these spectral features are markedly suppressed, as illustrated by the vanishing absorption in the 0–3 eV range for $CsGeBr_3$, highlighting the indispensable role of excitonic coupling. Mathematically, this can be traced to the off-diagonal matrix elements of the BSE kernel—short-range exchange $H^{(x)}$ [Eq. (SM7)] and long-range screened direct $H^{(c)}$ [Eq. (SM8)]—which mix interband configurations via real-space orbital overlap and Coulomb attraction, thereby generating resonant excitations and redistributing oscillator strength. The origin of these transitions lies in the distribution of available initial–final state pairs set by the underlying DOS and band dispersion; however, their intensities and spectral positions are governed by the excitonic kernel, whose strength scales with E_b^{ex} [cf. Eq. (SM21)]. Therefore, the sharp optical peaks near the absorption onset are not simply artifacts of band alignment, but rather emerge from the coherent interplay between the orbital-projected DOS and many-body interactions. This explains why even subtle variations in orbital composition near the Fermi level—such as those induced by Rb substitution or lattice strain—can substantially modify excitonic peak intensities and light–matter coupling efficiency.

Beyond its role in shaping optical transitions, the DOS profile also offers critical insight into lattice instabilities and ferroelectric tendencies—both central to the multifunctional character of lead-free halide perovskites. As highlighted in Fig. SM10(e), the prominent contribution of Ge-*s* orbitals near the valence band edge indicates the presence of stereochemically active lone pairs. These lone pairs, associated with asymmetric charge distributions, promote non-centrosymmetric lattice distortions, which are foundational to the emergence of spontaneous polarization. This behavior mirrors that observed in lone-pair-active ferroelectrics such as $BiFeO_3$ [18], where similar orbital asymmetries underpin switchable dipole formation. Furthermore, the redistribution of DOS intensity under Rb substitution—particularly in the 2–5 eV range—suggests a modified local bonding environment, potentially reinforcing polar displacements. Such atomic-scale insights from the DOS directly connect to the macroscopic dielectric screening trends analyzed in Sec. SM11 A 4, where suppressed energy loss and enhanced ferroelectric stability were observed in the Cl-based systems. Taken together, the DOS not only clarifies the orbital origins of optical transitions, but also serves as a fingerprint of ferroelectric activity, electronic asymmetry, and bond ionicity. These connections lay the foundation for the subsequent discussion of ferroelectric polarization and its coupling to electronic structure, thus completing the comprehensive picture of exciton-mediated light–matter interaction in these versatile perovskites.

Taken together, the orbital-resolved DOS data in Fig. SM10 complete the optical analysis by tracing the origin of key electronic transitions back to the chemical environment and symmetry-breaking atomic configurations. Importantly, the pronounced contribution of Ge-*s* lone pairs near the valence edge not only mediates strong interband transitions but also correlates with lattice asymmetries responsible for ferroelectric distortions. This link between orbital asymmetry and polar displacement, already hinted at in the excitonic trends of Secs. SM11 A 1 and SM11 A 2, becomes foundational in the context of spontaneous polarization and bistable switching behavior. As we transition into Part II, we shift focus from the optoelectronic functionality to the ferroelectric response, beginning with a quantitative analysis of double-well energy profiles that reveal how Rb doping stabilizes the polar phase without sacrificing switchability. These insights build upon the electronic structure landscape established in the DOS, reinforcing the interconnected nature of light–matter interaction and ferroic order in lead-free halide perovskites.

B. Part II: Ferroelectricity

This part investigates the origin and tunability of ferroelectric behavior in $CsGeX_3$ halide perovskites and their Rb-substituted derivatives, extending the optical and electronic insights developed in Part I, i.e., Sec. SM11 A, which addressed excitonic effects, bandgap modulation, dielectric screening, and orbital-level charge asymmetry. Here, in Part II, Sec. SM11 B, we begin by mapping the double-well energy landscapes that characterize ferroelectric switching, barrier heights, and phase stability across the halide series (Sec. SM11 B 1). In Sec. SM11 B 2, we quantify how Rb doping modifies spontaneous polarization and lattice anisotropy, revealing trends that transcend simple structural metrics. Sec. SM11 B 3 then disentangles the relative contributions of geometric distortion and electronic asymmetry by correlating polarization with c/a ratios and Born effective charge analyses. Together, these three subsections establish a microscopic framework for understanding how compositional tuning governs ferroic order in these lead-free systems.

1. Double-Well Energy Landscapes as Unified Descriptors of Ferroelectric Stability and Optoelectronic Functionality in Pure and Rb-Doped $CsGeX_3$

To elucidate the microscopic origin of the structure–property interdependence established in Part I (Sec. SM11 A), we turn to the lattice energetics governing polar instabilities in $CsGeX_3$ and their evolution under Rb doping. The double-well potential energy surfaces shown in Fig. SM11, expressed as the total energy ΔE versus the distortion parameter λ, provide a direct window into the ferroelectric switching landscape [49]. This parameter λ continuously interpolates between the centrosymmetric paraelectric structure ($\lambda = 0$) and the symmetry-broken ferroelectric minima ($\lambda = \pm 1$), capturing the fundamental displacive nature of the phase transition. Across all halide variants, the emergence of symmetric double wells confirms bistability and spontaneous symmetry breaking, hallmarks of a robust ferroelectric ground state. More importantly, the variation in well depth and curvature across chemical compositions directly reflects the strength of local lattice instabilities, which were shown in Sec. SM11 A 5 to modulate the orbital hybridization and in Sec. SM11 A 3 to influence both the QP band gap E_g^{GW} and dielectric screening ε_0. These structural distortions underpin the enhanced exciton binding energies E_b^{ex} reported in Sec. SM8 A, where reduced symmetry and increased lattice rigidity strengthen the Coulomb interaction between charge carriers. Thus, the double-well energy landscapes not only diagnose ferroelectric switching potential but also encapsulate a coherent physical mechanism linking structural distortion, electronic localization, and optical response—an interdependence that emerges as a central theme throughout Part I.

The energetic profiles in Fig. SM11 reveal a systematic decrease in the double-well barrier height $\Delta E_{\mathrm{barrier}}$ along the halogen series from Cl to I, with values of 47.66, 24.83, and 21.66 meV/atom for undoped $CsGeCl_3$, $CsGeBr_3$, and $CsGeI_3$, respectively. This trend parallels the reduction in off-center displacement of the Ge cation within the GeX_6 octahedral cage—0.35, 0.22, and 0.17 Å for X = Cl, Br, and I—which directly governs the depth and curvature of the energy wells. The lighter halide (Cl) induces stronger local lattice asymmetry due to its smaller ionic radius and higher electronegativity, leading to deeper

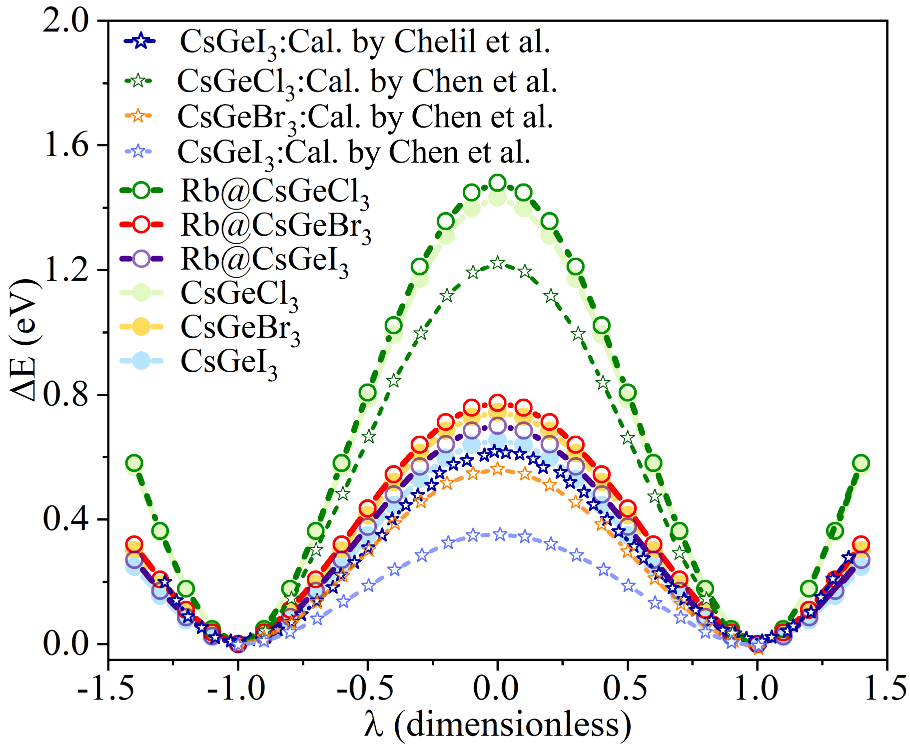

FIG. SM11. Double-well total energy profiles $\Delta E(\lambda)$ for pure $CsGeX_3$ (X = Cl, Br, I) and Rb-doped $Cs_{0.83}Rb_{0.17}GeX_3$, computed using PBE-GGA in WIEN2k. The distortion parameter λ interpolates between the centrosymmetric paraelectric structure ($\lambda = 0$) and the fully polarized ferroelectric configurations ($\lambda = \pm 1$). All systems exhibit a symmetric double-well topology characteristic of displacive ferroelectricity, with barrier heights and well curvatures reflecting the strength of spontaneous lattice instability. The enhancement of $\Delta E_{\text{barrier}}$ upon Rb doping, particularly in $CsGeCl_3$, signifies increased polarization retention and stronger coupling between structural distortion and electronic response. Rescaled reference data from Chelil *et al.* [51] and Chen *et al.* [52] are shown for comparison.

polarization wells and more stable ferroelectric minima. These geometric distortions were shown in Sec. SM11 A 5 to enhance orbital hybridization between Ge s/p and halogen p states, while simultaneously sharpening the band dispersion and widening the band gap (Sec. SM11 A 2). Moreover, the strong lattice rigidity associated with Cl-based compounds suppresses dielectric screening (Sec. SM11 A 1), resulting in elevated exciton binding energies E_b^{ex} (Sec. SM8 A). Conversely, the softer lattice in $CsGeI_3$ not only flattens the double-well but also increases polarizability, narrows the band gap, and weakens the exciton binding, as shown via the reduced reduced mass μ and enhanced ε_0 in Sec. SM8 A. This convergence of structural, dielectric, and electronic behavior underscores a key structure–property principle: the double-well barrier height is not merely a mechanical descriptor of lattice distortion but a physically encoded metric for dielectric response and excitonic confinement. Chemically, it reflects how halogen substitution alters both the symmetry-breaking force constants and the electronic screening environment, establishing a tunable pathway to modulate light–matter interactions through composition alone.

To further understand the tunability of ferroelectric stability, we now consider the effect of Rb substitution on the double-well profiles. As seen in Fig. SM11, introducing 17% Rb at the A-site of $CsGeCl_3$ increases the barrier height from 47.66 to 49.3 meV/atom, indicating enhanced structural rigidity and deeper polarization wells. This increase is consistent with the volumetric contraction and bond stiffening discussed in Sec. SM11 A 3, where the reduced lattice constant due to Rb incorporation mimics hydrostatic pressure. As established in that section, compression leads to a decrease in E_g^{GW} and an increase in ε_0, both of which stem from enhanced orbital overlap and modified charge density distribution around the Ge–X framework. This is further corroborated by the ELF analysis in Sec. SM8 D, where Rb doping strengthens charge localization along the Ge–Cl bonds, suggesting a transition toward more pronounced charge confinement. Mathematically, this corresponds to a local increase in the second derivative of the potential energy surface with respect to λ, i.e., $\partial^2 \Delta E/\partial \lambda^2$, reflecting a steeper well curvature and higher restoring force for atomic displacements. This increase in $\partial^2 \Delta E/\partial \lambda^2$ can be physically interpreted as the macroscopic manifestation of enhanced real-space charge localization along the Ge–X bonds, as captured by the ELF analysis. A higher degree of electron localization strengthens the electrostatic binding between cations and anions, in agreement with the Bader charge evidence of reinforced ionic character (Sec. SM11 C 1), thereby steepening the potential well and increasing the restoring force for atomic displacements. Physically, this indicates stronger coupling between lattice polarization and the underlying electronic structure—a theme echoed in Sec. SM11 A 1, where polarization-dependent screening was shown to directly impact the exciton binding energy E_b^{ex} through the inverse scaling in Eq. (SM21). Hence, Rb doping does more than simply stabilize the ferroelectric phase—it enhances the structural–electronic feedback loop, enabling dynamic modulation of excitonic and dielectric responses via local compositional tuning.

To contextualize these results, we compared our PBE-GGA-calculated energy barriers with prior studies on $CsGeI_3$, including those by Chelil *et al.* [51], based on the FP-LAPW method in WIEN2k, and Chen *et al.* [52], based on LDA and plane-wave pseudopotentials in VASP. To ensure quantitative comparability, the reported datasets were rescaled and normalized following the procedure. Reference data were processed to ensure consistency with our results through the following transformations: (i) the λ-axis was shifted so that energy minima aligned at $\lambda = \pm 1$; (ii) λ values were symmetrically normalized; (iii) energy values were offset such that the minima corresponded to zero; and (iv) energies were converted to eV by appropriate scaling. Specifically, meV/atom data from Chelil et al. [51] were multiplied by 30 (reflecting the number of atoms in our supercell) and divided by 1000, while meV/f.u. data from Chen et al. [52] were multiplied by 6 (matching our 30-atom supercell, as each formula unit contains 5 atoms) and similarly divided by 1000. These transformations were applied solely to harmonize axis scaling and units, without altering the physical interpretation of the reference data. This transformation aligns the different conventions for energy normalization (per atom vs. per formula unit) and structural interpolation. After rescaling, our $CsGeI_3$ energy barrier of 21.66 meV/atom closely matches the 20.3 meV/atom value from Chelil *et al.*, and shows strong consistency with the 18.4 meV/atom barrier from Chen *et al.*, despite the well-known underestimation of absolute barrier heights by LDA [53]. Additionally, our computed polar-to-nonpolar energy difference for $CsGeBr_3$ agrees with the 85 meV/f.u. (or ∼17 meV/atom) value reported by Zhang *et al.* [2]. These cross-validation results confirm the reliability and transferability of our structural energetics approach, reinforcing the connection between ferroelectric well depth and underlying bonding physics.

The enhanced double-well depth and curvature induced by Rb doping also carry direct implications for device-level ferroelectric functionality. Within a thermodynamic framework, the barrier height $\Delta E_{\mathrm{barrier}}$ determines the coercive field required for polarization switching, while the curvature at the minima relates to the phonon stiffness and dynamical response time. A steeper energy well, as observed in Rb-doped $CsGeCl_3$, implies both a higher coercive field and a longer polarization retention time—features essential for non-volatile memory and ferroic switching applications. In contrast, the shallow wells of $CsGeI_3$ suggest enhanced susceptibility to thermal fluctuations and quantum tunneling, pointing to incipient ferroelectricity or quantum paraelectric behavior under low-field or cryogenic conditions. These interpretations are consistent with the Berry-phase analysis of spontaneous polarization in Sec. SM8 B, where larger dipole moments and more abrupt phase evolution correlate with deeper wells and sharper structural asymmetry. Moreover, the dielectric screening discussed in Sec. SM11 A 1—which enters the exciton binding energy through Eqs. (SM19) and (SM21)—is inherently coupled to this double-well landscape, as polarization fluctuations contribute directly to the static dielectric constant. Consequently, the energy barriers in Fig. SM11 quantify not only structural stability but also serve as a multi-property descriptor linking exciton lifetime, dielectric tunability, and polarization-switching dynamics. This underlines a central result of the present work: that structural bistability and its compositional control via Rb doping can serve as a design axis for tuning light–matter interactions, excitonic dissociation, and field-driven ferroic transitions in halide perovskites.

To frame the role of the double-well profile more generally, we now consider it as a unified mathematical descriptor linking structural, electronic, and optical properties. The energy barrier $\Delta E_{\mathrm{barrier}}$ provides a direct estimate of the work required to reversibly switch polarization, and is proportional to the coercive field E_c under a Landau-type description, $E_c \propto \Delta E_{\mathrm{barrier}}/P_s$ [54], where P_s is the spontaneous polarization discussed in Sec. SM8 B. The curvature of the well at the minima, quantified by the second derivative $\partial^2 \Delta E/\partial \lambda^2$, determines the soft-mode phonon frequency ω_0 via $\omega_0^2 \propto (\partial^2 \Delta E/\partial \lambda^2)/M_{\mathrm{eff}}$, where M_{eff} is the reduced mass of the displacement coordinate. As shown in Secs. SM11 A 5 and SM8 D, the chemical environment—particularly the bonding strength along Ge–X chains—modifies both $\Delta E_{\mathrm{barrier}}$ and $\partial^2 \Delta E/\partial \lambda^2$ by altering the local force constants and orbital overlap. These structural quantities in turn modulate the dielectric screening ε_0 (Sec. SM11 A 1), which enters directly into the exciton binding energy via the inverse square scaling of Eq. (SM21). Thus, we see that $\Delta E(\lambda)$ is not only a structural signature of ferroelectricity, but a multivariate generator of dielectric and excitonic behavior—linking geometric asymmetry, phonon stiffness, electronic polarizability, and exciton confinement in a single potential energy surface. This formalism provides a robust predictive framework for evaluating the impact of alloying (e.g., Rb substitution) or external stimuli (e.g., pressure, strain) on a broad range of response functions central to light–matter interaction and ferroic functionality.

The robustness of this structure–function framework is further underscored by its quantitative agreement with prior theoretical studies. For example, our PBE-GGA barrier height for $CsGeI_3$ (21.66 meV/atom), computed using the all-electron FP-LAPW method in WIEN2k, closely matches the values reported by Chelil *et al.* [51] (20.3 meV/atom) and Chen *et al.* [52] (18.4 meV/atom), validating both the energy landscape topology and the structural distortion path. Moreover, our extracted polar-to-nonpolar energy difference for $CsGeBr_3$ is consistent with the 17 meV/atom value derived from the 85 meV/f.u. reported by Zhang *et al.* [2]. These cross-study comparisons affirm the transferability of our method across computational platforms (e.g., VASP vs. WIEN2k), functionals (LDA vs. GGA), and structural models. More importantly, our analysis adds depth by correlating these energy barriers with chemical bonding strength, orbital mixing, and charge localization metrics—as quantified by the ELF (Sec. SM8 D) and DOS (Sec. SM11 A 5) analyses.

For instance, the stronger ELF maxima and Ge–X bond localization observed in $CsGeCl_3$ explain its deeper double-well and higher ferroelectric stability, consistent with a more ionic Ge–Cl bond character revealed in Sec. SM11 C 1, while the shallower wells in $CsGeI_3$ reflect its more covalent Ge–I bonding and enhanced lattice softness.

For instance, the stronger ELF maxima and more localized, predominantly ionic Ge–Cl bonds observed in $CsGeCl_3$ explain its deeper double-well potential and higher ferroelectric stability, while the shallower wells in $CsGeI_3$ reflect weaker covalency and enhanced lattice softness.

By integrating energy landscapes with electron density topology, our approach moves beyond traditional barrier-height tabulations and establishes a structure-resolved design paradigm applicable to broader halide chemistries and perovskite derivatives. This benchmarking not only validates the accuracy of our first-principles methodology but also illustrates its predictive power in identifying chemically tunable pathways for co-optimizing ferroelectric and excitonic responses.

Viewed in totality, the double-well energy landscapes extracted in this work reveal far more than structural symmetry breaking—they encode a multidimensional design axis that unifies ferroelectric robustness, dielectric tunability, and excitonic control within a single structural descriptor. By tuning the shape, depth, and curvature of these wells through halogen chemistry and Rb alloying, one can simultaneously modulate the coercive field, polarization retention, and exciton binding—properties that are typically optimized independently. This convergence establishes structural bistability not merely as a hallmark of ferroelectricity, but as a programmable control parameter for engineering field-switchable optical responses, exciton lifetimes, and light–matter coupling strength. In particular, the deep and narrow wells in Rb-doped $CsGeCl_3$ suggest long-lived polarization states ideal for non-volatile memory or electric-field-controlled photonic devices, while the shallow wells in $CsGeI_3$ favor low-barrier dynamic switching and tunable dielectric response under minimal stimuli. When considered alongside the polarization-dependent absorption spectra (Sec. SM11 A) and the volume-driven excitonic trends (Sec. SM8 A), these energy profiles offer a coherent, predictive, and materials-agnostic framework for co-optimizing structural and optoelectronic functionalities.

Having established the bistable energy landscape as the structural foundation for ferroic behavior, we next quantify the macroscopic polarization associated with these distortions using the Berry-phase formalism (Sec. SM11 B 2), thereby linking the energy topology to an experimentally accessible order parameter.

2. *Enhancing Ferroelectric Polarization and Structural Tunability in Rb-Doped $CsGeX_3$ Halide Perovskites*

Building directly on the double-well energy landscapes presented in Sec. SM11 B 1, which reveal the presence of bistable minima and switchable polarization states in $CsGeX_3$ and its Rb-alloyed counterparts, we now shift focus to the quantitative evaluation of spontaneous polarization P_s—a macroscopic order parameter that encapsulates the degree of inversion symmetry breaking and underpins the dielectric, excitonic, and switching functionalities of ferroelectric perovskites. Within the modern theory of polarization, P_s is rigorously computed via the Berry-phase formalism, which tracks the geometric phase accumulated by the occupied electronic states as ions are adiabatically displaced along a continuous path. Specifically, we evaluate $P(\lambda)$ as a function of a dimensionless distortion coordinate λ, which interpolates between the nonpolar centrosymmetric structure ($\lambda = 0$) and the fully distorted polar configuration ($\lambda = \pm 1$). As shown in Fig. SM12, all $CsGeX_3$ compounds exhibit an approximately linear $P(\lambda)$ dependence, consistent with a soft-mode displacive ferroelectric mechanism in which the polarization grows smoothly with Ge off-centering. This linearity affirms that the polar instability is phonon-driven and structurally continuous, in contrast to order–disorder ferroelectrics. The strength of this response—and hence the slope of $P(\lambda)$—varies across the halogen series, reflecting systematic changes in the lattice restoring force and octahedral stiffness. Lighter halides such as Cl induce steeper polarization slopes, consistent with deeper energy wells (Fig. SM11), stronger Ge s–p stereochemical mixing, and more localized (more ionic) Ge–Cl bonding, whereas heavier halides like I suppress polar distortions due to increased ionic size and screening and exhibit greater Ge–I mid-bond sharing (more covalent). These chemical trends echo the orbital asymmetry and bond localization patterns identified earlier in Secs. SM8 D and SM11 A 5, thus reinforcing the electronic–structural coupling that underlies polarization. Importantly, partial substitution of Cs by Rb subtly steepens the $P(\lambda)$ profiles across all halides, indicating enhanced polarizability. This enhancement is driven by axial elongation of the unit cell and increased Ge displacement under Rb-induced chemical pressure—factors that simultaneously deepen the double-well profiles and amplify local dipole moments. Taken together, these Berry-phase results demonstrate that P_s is not only a measurable macroscopic signature of ferroelectricity, but also a sensitive probe of the underlying microscopic mechanisms, directly connecting the bonding topology, lattice strain, and electrostatic asymmetry that have emerged throughout the preceding analyses.

Quantitatively, the computed spontaneous polarization P_s values reveal a clear halogen-dependent trend, decreasing from 22.35 μC/cm^2 in $CsGeCl_3$ to 19.02 μC/cm^2 in $CsGeBr_3$ and further to 17.25 μC/cm^2 in $CsGeI_3$. This monotonic reduction mirrors the corresponding decrease in Ge off-center displacements—0.35 Å, 0.22 Å, and 0.16 Å, respectively—which originates from the increasing ionic radius and polarizability of the halide anions. Larger halides increase the covalent character of Ge–X bonding and reduce the rigidity of the GeX_6 framework, weaken the second-order Jahn-Teller distortion driven by the Ge s-lone pair, and thus diminish both the depth of the double-well (Sec. SM11 B 1) and the magnitude of ferroelectric instability. These compositional trends are clearly visible in the $P(\lambda)$ profiles in Fig. SM12, where both slope and curvature decrease from Cl to I, consistent with a softening of the polar mode and a reduced effective force constant. These predictions are strongly supported by experimental measurements. For $CsGeBr_3$, single-crystal studies report a P_s of $\sim$15 μC/cm^2 [2], while for $CsGeI_3$, thin-film

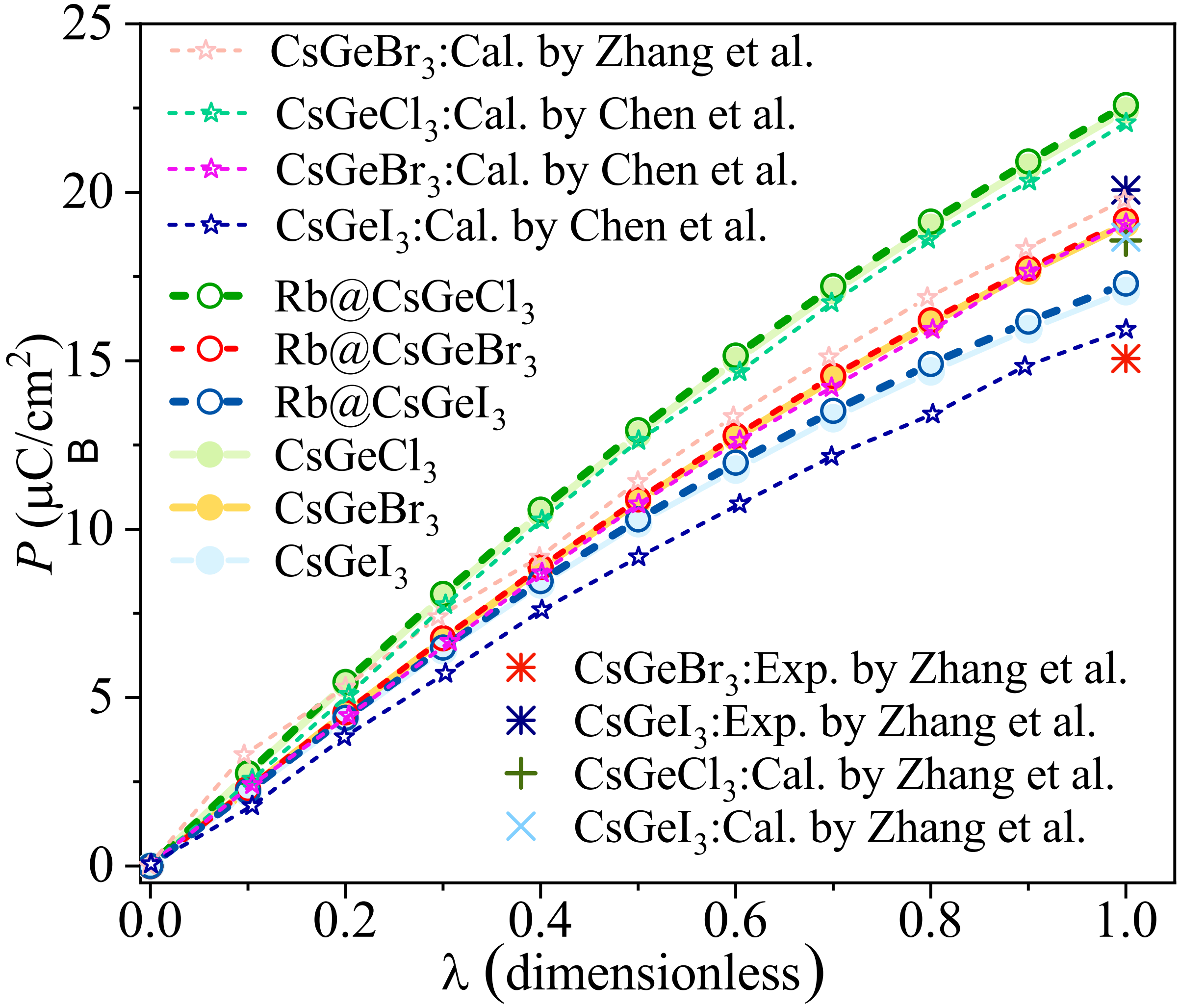

FIG. SM12. Variation of the electric polarization P (in μC/cm^2) as a function of the distortion parameter λ for pure $CsGeX_3$ (X = Cl, Br, I) and Rb-doped $Cs_{0.83}Rb_{0.17}GeX_3$, calculated using the PBE-GGA functional with WIEN2k. The parameter λ interpolates between the centrosymmetric structure (λ = 0) and the fully distorted polar phase (λ = ±1). For comparison, theoretical data from Chen *et al.* [52] ($CsGeX_3$, LDA/VASP) and Zhang *et al.* [2] ($CsGeCl_3$, $CsGeI_3$, GGA/WIEN2k) are included, along with experimental values for $CsGeBr_3$ and $CsGeI_3$ from the same study.

measurements yield values around 18–20 μC/cm^2, depending on film thickness and orientation. Although our 0 K PBE-GGA values slightly exceed these numbers, the discrepancy is within expected bounds given the absence of thermal disorder, domain effects, and surface screening in DFT calculations. Indeed, polarization in halide perovskites is known to be highly sensitive to extrinsic factors such as strain, dimensionality, and substrate clamping [51, 55]. Notably, the relatively high experimental P_s in $CsGeI_3$ thin films—despite I being the least polarizing halide—is likely a consequence of dimensional confinement and suppressed octahedral tilting, which locally enhance Ge off-centering. These trends align with similar enhancements observed in $BiFeO_3$ and hybrid organic-inorganic perovskites, where nanoscale effects boost ferroelectric order beyond expectations. Rb substitution introduces a modest yet systematic enhancement in P_s across all halides: increasing to 22.57, 19.15, and 17.28 μC/cm^2 for $Cs_{0.83}Rb_{0.17}GeX_3$ with X = Cl, Br, and I, respectively. While numerically small (on the order of ∼1%–8%), these gains are nontrivial in the context of practical device applications, where even subtle increases in dipole moment per unit cell can significantly impact switching dynamics, internal fields, and coupling to excitonic or optical responses. Structurally, Rb incorporation enhances tetragonality (c/a), elongating the axial lattice and amplifying Ge displacement—an effect explored in Sec. SM11 B 3. Moreover, this chemical tuning pathway circumvents the need for external fields or epitaxial strain, offering an intrinsic route for polarization engineering via A-site alloying. To further validate our Berry-phase results, we benchmarked them against an alternative approach based on BECs and ionic displacements. While both methods predict the same qualitative trends across the halide series, BEC-derived polarizations are systematically lower—e.g., 10.86 μC/cm^2 for $CsGeCl_3$, compared to 22.35 μC/cm^2 from the Bp. This discrepancy arises because the BEC approach captures only the ionic (nuclear) contribution, neglecting electronic polarization arising from charge redistribution. In contrast, the modern theory of polarization—as implemented via the Bp—includes the full quantum-mechanical response of the electronic wavefunctions to lattice displacements, making it the more complete and reliable metric for P_s in systems with significant covalency and lone-pair activity. Together, these insights reinforce the predictive fidelity of our first-principles approach, highlight the chemical flexibility of Rb doping, and point to a coherent structural–electronic mechanism that governs spontaneous polarization in $CsGeX_3$ perovskites.

Beyond static polarization trends, the implications of enhanced P_s extend directly to the thermodynamic and dynamic characteristics of ferroelectric behavior. The increase in spontaneous polarization induced by Rb doping implies a larger free-energy difference ΔE between the polar and nonpolar configurations, as captured by the deepened double-well potentials in Fig. SM11 (see also Sec. SM11 B 1). This stabilization of the polar phase leads to a higher coercive field E_c, the critical external electric field required to reverse polarization, which scales approximately as $E_c \sim \Delta E/(2P_s d)$, where d is the effective domain width. Experimental thin-film measurements on $CsGeI_3$ report a coercive field $E_c \approx 40$ kV cm^{-1} from a reconstructed P–E hysteresis loop after subtracting leakage current [2]; together with our computed increases in ΔE and P_s for Rb-doped compositions, this suggests that similar or higher E_c may be achievable under strain-stabilized conditions. Mathematically, the steepness of each potential well—quantified by the curvature $\kappa = \partial^2 E/\partial\lambda^2$ near the minimum—reflects the stiffness of the polar soft mode; larger κ corresponds to higher optical phonon frequencies, $\omega \propto \sqrt{\kappa/M}$, where M is the reduced mass, enhancing thermal resilience against entropic disorder. As a structural benchmark, Chen *et al.* [52] combine Rietveld-refined XRD and synchrotron X-ray pair distribution function (PDF) analyses with Berry-phase DFT and NEGF calculations to confirm the polar $R3m$ structure in $CsGeX_3$ (X = Cl, Br, I), report ferroelectric polarizations of ∼15.9, 19.0, and 22.0 μC cm^{-2} for $CsGeI_3$, $CsGeBr_3$, and $CsGeCl_3$, respectively, and map polarization-dependent photoresponse over 0.5–5.5 eV; the accompanying SI provides lattice and ADP parameters. Building on this framework, our energy landscape calculations for Rb-substituted compositions reveal an increase in the local curvature at the polar minima, implying a hardening of the polar soft mode ($\Delta\omega_s > 0$), consistent with the deepened double-well energetics in Fig. SM11 and the structural stiffening expected from chemical pressure. This dynamical hardening has critical implications for dielectric tunability. Within the Landau-Devonshire framework, the dielectric susceptibility χ varies inversely with the second derivative of the free energy: $\chi \sim 1/(\partial^2 F/\partial P^2)$. Thus, as the polarization well deepens and narrows with Rb doping, χ decreases and the material becomes less polarizable—a signature of increased robustness and lower dielectric loss. However, the coupling of phonon modes to the electronic polarizability (as discussed in Sec. SM11 A 1) enables field-tunable refractive index modulation. This opens the door to dynamic optical applications such as electro-optic switches and photonic modulators, where high P_s, low dielectric loss, and fast response time are crucial. In this light, Rb doping not only boosts P_s and stabilizes the ferroelectric phase, but also orchestrates a favorable balance between static polarization strength and dynamic field-responsiveness. The co-modulation of structural energetics, phonon dynamics, and dielectric behavior elevates $Cs_{1-x}Rb_xGeX_3$ as a promising materials platform for non-volatile memory, piezoelectric transducers, and tunable optoelectronics.

The polarization trends in Fig. SM12 quantitatively confirm the halogen- and Rb-dependence discussed above. For pristine compounds, Berry-phase-calculated spontaneous polarization P_s decreases systematically from 22.35 μC/cm^2 in $CsGeCl_3$ to 19.02 μC/cm^2 in $CsGeBr_3$ and 17.25 μC/cm^2 in $CsGeI_3$, reflecting the declining off-center displacement of Ge and softening of the double-well energy landscape (Sec. SM11 B 1). Upon 17% Rb alloying, P_s rises slightly but consistently to 22.57, 19.15, and 17.28 μC/cm^2, respectively. Though the absolute gains are modest (0.1–0.3 μC/cm^2), they are structurally significant, as they correspond to enhanced lattice distortion and electrostatic dipole stabilization—especially in $CsGeBr_3$, where the relative increase exceeds 1.3%. This tunability arises from chemical pressure effects: smaller Rb^+ ions compress the lattice slightly, increase the c/a ratio, and amplify Ge–X bond asymmetry, thus strengthening ferroelectric character. Such internal lattice deformation is supported by electron localization and ELF patterns (Sec. SM8 D), SM8 D), which reveal a halogen-dependent evolution: enhanced Ge–I covalency in I-based compounds and slightly increased Ge–Cl/Ge–Br ionicity in Cl/Br-based compounds upon Rb doping. These results align with prior experimental estimates of P_s in $CsGeBr_3$ (∼15 μC/cm^2) and $CsGeI_3$ thin films (∼20 μC/cm^2) [2], once finite-temperature effects and dimensionality are accounted for. Our calculations also maintain excellent agreement with prior theoretical results using the same exchange–correlation functional (e.g., GGA/WIEN2K), while discrepancies with LDA-based values [52] are attributed to differences in relaxed structures and c/a ratios. Moreover, when benchmarked against BEC estimates, Berry-phase polarizations are nearly double in magnitude—for example, 22.35 vs. 10.86 μC/cm^2 in $CsGeCl_3$—underscoring the importance of accounting for both ionic displacement and electronic redistribution. This highlights the inherently quantum mechanical nature of ferroelectricity in these materials, wherein electronic cloud deformation cooperates with structural asymmetry to stabilize the polar phase.

Taken together, these findings affirm the viability of Rb alloying as a subtle yet effective lever for tuning ferroelectric properties in lead-free halide perovskites. The modest enhancements in spontaneous polarization—though not dramatic—stem from chemically induced lattice distortions that intensify the polar off-centering of the Ge cation, particularly in compounds with intermediate halide softness. These results underscore a broader structure–function paradigm wherein electronic, dielectric, and optical responses can be modulated by targeted chemical substitution at the A-site. Moreover, the quantitative correspondence between theory and experiment, along with internal consistency across different exchange–correlation functionals and polarization formalisms, lends credibility to the predictive power of the Berry-phase framework in this materials class. Yet, a deeper question remains: Are these polarization trends governed purely by structural distortions—captured by

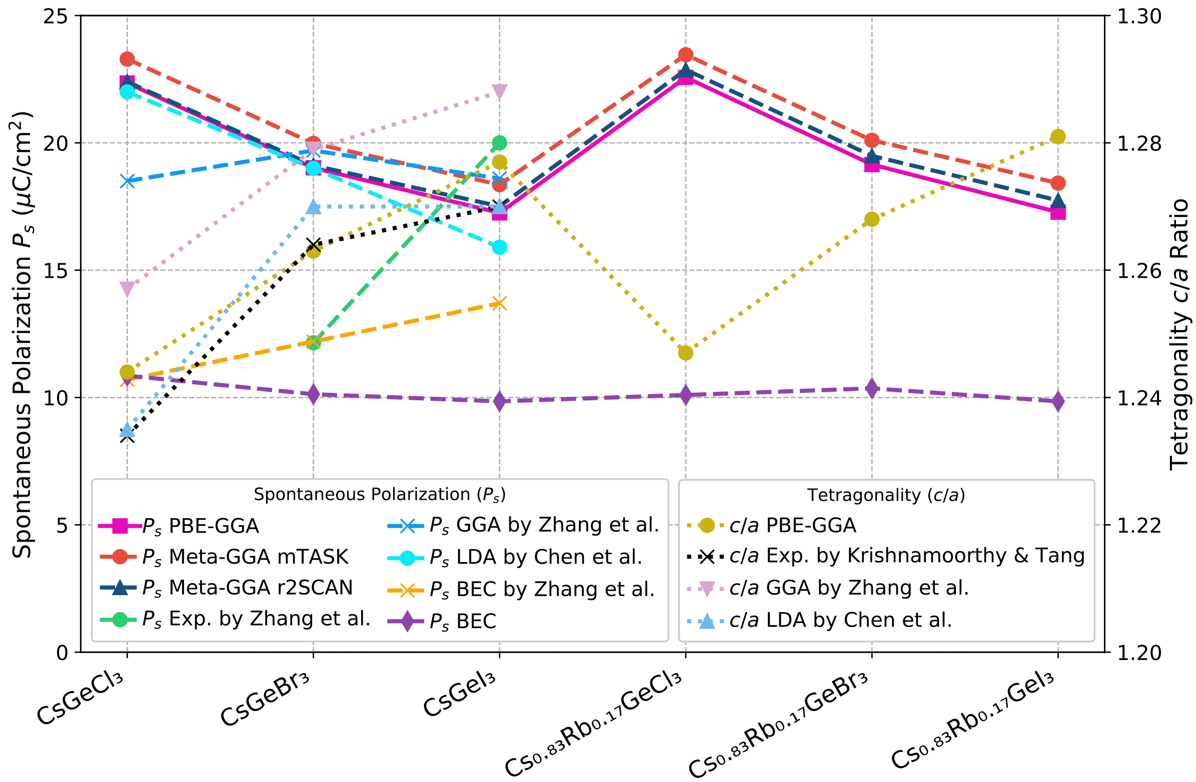

FIG. SM13. Calculated and experimental spontaneous polarization P_s and tetragonality ratio c/a for pure and Rb-doped $CsGeX_3$ (X = Cl, Br, I) perovskite compounds in the rhombohedral ($R3m$) phase. The left vertical axis shows P_s in μC/cm^2, calculated using PBE-GGA (orange circles with solid lines), mTASK (magenta up triangles with dashed lines), and r2SCAN (navy blue down triangles with dashed lines) meta-GGA functionals. Additional theoretical values based on BECs (BEC, violet pentagons) and prior studies using LDA (cyan right triangles) and GGA (light blue squares) are also displayed. Experimental measurements from Zhang *et al.* [2] for $CsGeBr_3$ and $CsGeI_3$ are shown as green triangles connected by dotted lines. The right vertical axis presents the structural tetragonality ratio c/a, derived from relaxed geometries using PBE-GGA (yellow circles with dotted lines), and compared against prior GGA (pink asterisks), LDA (blue stars), and experimental values reported by Krishnamoorthy and Tang (black crosses). This dual-axis representation illustrates the correlation between spontaneous polarization and lattice elongation, highlighting how Rb substitution enhances axial strain and sustains or boosts P_s across the halide series.

metrics like the c/a ratio—or do quantum electronic effects, such as charge redistribution and hybridization asymmetry, play a decisive role? In the following subsection (Sec. SM11 B 3), we disentangle these contributions by systematically analyzing the polarization–tetragonality relationship, incorporating comparative data from alternative functionals and BEC analyses. This structural–electronic decomposition offers critical insight into the microscopic origin of polarization and informs design strategies for next-generation ferroelectric semiconductors.

3. Disentangling Structural and Electronic Drivers of Polarization in Rb-Modified Halide Perovskites

A central question emerging from the preceding polarization analysis is whether the observed trends in spontaneous polarization (P_s) across $CsGeX_3$ (X = Cl, Br, I) and their Rb-substituted analogs arise solely from structural distortions or if deeper electronic mechanisms are at play. It is well known that ferroelectric polarization is often linked to axial elongation in perovskites, typically quantified via the tetragonality ratio (c/a). However, the presence of chemically induced perturbations, such as Rb doping and halogen substitution, may decouple this classical strain–polarization relationship. Here, we systematically explore the correlation between P_s and c/a across all compositions and exchange–correlation functionals to test the sufficiency of structural metrics in explaining the polarization behavior. To this end, we evaluate Berry-phase-calculated P_s values across a structurally diverse set of relaxed geometries and compare them with corresponding c/a ratios extracted from fully relaxed polar phases. Complementary BEC estimates are also employed to isolate the purely ionic displacement component of the polarization. This multifaceted approach allows us to critically assess whether P_s scales monotonically with lattice anisotropy, or whether electronic contributions—such as charge redistribution, bonding asymmetry, and lone-pair stereochemical activity—must be invoked to fully capture the microscopic origins of ferroelectricity in these lead-free halide perovskites.

TABLE SM3. Spontaneous electric polarization P_s (μC/cm^2), lattice parameter a (Å), and c/a ratio for $CsGeX_3$ (X = Cl, Br, I) and Rb-doped derivatives $Cs_{0.83}Rb_{0.17}GeX_3$ in the rhombohedral ($R3m$) phase, calculated using DFT. Polarization values are obtained via the Bp and BEC methods. Results are reported for the PBE-GGA functional and two meta-GGA functionals: mTASK and r2SCAN. For comparison, theoretical data from the literature for undoped compounds (using either Bp or BEC) and experimental values for $CsGeBr_3$ single crystals and $CsGeI_3$ thin films [2] are also included. The conventional hexagonal lattice parameters a and c were derived from the rhombohedral primitive lattice parameters a_r and α_r using the transformations $a = 2a_r \cos[(\pi - \alpha_r)/2]$ and $c = 3\sqrt{a_r^2 - a^2/3}$, following the method described in Chapter 4, Subchapter 4.3, Page 40 of Ref. [36]. Values obtained in this work are marked with an asterisk (*). To improve clarity, repeated entries within each compound group are displayed only once. Empty cells indicate values identical to those in the row immediately above. A dash (–) indicates either that a value is not available or not applicable (e.g., the exchange-correlation functional is undefined for experimental data).

Compound	XC	a (Å)	c/a	P_s (μC/cm^2)	Code	Method	Ref.
$CsGeCl_3$	PBE-GGA	7.770	1.244	22.35	WIEN2k	Bp	*
	mTASK			23.29			*
	r2SCAN			22.40			*
	PBE-GGA			10.86		BEC	*
	PBE-GGA	7.660$^\#$	1.234$^\#$	20.16		Bp	*
	LDA	7.684	1.235	22.00	VASP		[52]
	PBE-GGA	7.762	1.257	18.5			[2]
	PBE-GGA			10.7		BEC	[2]
$CsGeBr_3$	PBE-GGA	8.003	1.263	19.02	WIEN2k	Bp	*
	mTASK			19.98			*
	r2SCAN			19.11			*
	PBE-GGA			10.13		BEC	*
	PBE-GGA	7.892 $^\#$	1.264$^\#$	17.08		Bp	*
	LDA	8.367	1.270	19.00	VASP		[52]
	PBE-GGA	8.033	1.279	19.7			[2]
	PBE-GGA			12.2		BEC	[2]
	-	-	-	12-15	-	Exp.	[2]
$CsGeI_3$	PBE-GGA	8.495	1.277	17.25	WIEN2k	Bp	*
	mTASK			18.36			*
	r2SCAN			17.51			*
	PBE-GGA			9.85		BEC	*
	PBE-GGA	8.297$^\#$	1.270$^\#$	14.01		Bp	*
	LDA	8.372	1.270	15.90	VASP		[52]
	PBE-GGA	8.516	1.288	18.6			[2]
	PBE-GGA			13.7		BEC	[2]
	TB-mBJ	8.34	1.00	15.82	WIEN2k	Bp	[51]
	-	-	-	$\sim$20$^{\#\#}$	-	Exp.	[2]
$Cs_{0.83}Rb_{0.17}GeCl_3$	PBE-GGA	7.773	1.247	22.57	WIEN2k	Bp	*
	mTASK			23.46			*
	r2SCAN			22.87			*
	PBE-GGA			10.10		BEC	*
$Cs_{0.83}Rb_{0.17}GeBr_3$	PBE-GGA	7.997	1.268	19.15	WIEN2k	Bp	*
	mTASK			20.10			*
	r2SCAN			19.49			*
	PBE-GGA			10.36		BEC	*
$Cs_{0.83}Rb_{0.17}GeI_3$	PBE-GGA	8.501	1.281	17.28	WIEN2k	Bp	*
	mTASK			18.42			*
	r2SCAN			17.74			*
	PBE-GGA			9.85		BEC	*

$^\#$ Experimental lattice parameters: values for $CsGeCl_3$ and $CsGeI_3$ are taken from Ref. [40], and those for $CsGeBr_3$ from Ref. [56]. These parameters were used in specific calculations as indicated.
$^{\#\#}$ Indicates values measured from thin film samples.

Figure SM13 and Table SM3 offer a direct comparison between the spontaneous polarization P_s and the tetragonality ratio c/a for both pristine and Rb-substituted $CsGeX_3$ compositions (X = Cl, Br, I). Interestingly, while c/a increases steadily from $CsGeCl_3$ to $CsGeI_3$, the spontaneous polarization follows the opposite trend, decreasing from 22.35 μC/cm^2 to 17.25 μC/cm^2 within the PBE-GGA framework. This counterintuitive observation persists across more advanced exchange–correlation treatments: meta-GGA functionals such as mTASK and r2SCAN also predict decreasing P_s values with increasing c/a. Rb doping, despite producing only minor increments in the c/a ratio (typically $\lesssim$0.004), still yields modest enhancements in P_s—further decoupling the polarization response from structural elongation. Such systematic deviations from the classical ferroelectric expectation—that greater axial distortion should amplify polarization—suggest that structural anisotropy alone is insufficient to account for the observed trends. In particular, $CsGeCl_3$ stands out as having both the smallest tetragonality and the largest polarization, while $CsGeI_3$ shows the reverse behavior. These findings indicate that purely geometric metrics like c/a do not universally track ferroelectric strength in these compounds and that deeper electronic contributions must be considered to fully explain the polarization landscape.

To uncover the origin of this structural–electronic decoupling, we perform a deeper analysis of the electronic factors that may drive polarization independently of lattice distortion. While tetragonality reflects the macroscopic elongation of the lattice, it does not capture subtle quantum features such as asymmetric electron localization, bonding character, or lone-pair stereochemistry. In $CsGeX_3$ compounds, the Ge^{2+} cation possesses a stereochemically active $4s^2$ lone pair, which can hybridize with $4p$ states and nearby halide p orbitals to produce a non-centrosymmetric charge distribution that stabilizes the polar structure. The degree of this stereochemical Ge s–p mixing—and hence the electronic contribution to P_s—is strongly influenced by halide identity: Cl, being more electronegative, promotes greater lone-pair-induced charge asymmetry (despite a more ionic Ge–Cl bond overall) than Br or I, whereas I shows more covalent Ge–I mid-bond sharing and a softer lattice. This interpretation is consistent with the observed decrease in polarization from Cl to I, even as c/a increases. Furthermore, the incorporation of Rb enhances this electronic asymmetry by modifying the local bonding environment, as will be quantitatively shown in subsequent sections using Bader charge and electron ELF analyses. Together, these insights suggest that electronic structure, rather than purely ionic displacement, plays a central role in determining the magnitude and tunability of ferroelectric polarization in these lead-free halide perovskites.

To further assess the interplay between structural distortion and electronic polarization, we benchmark the Berry-phase computed P_s values against those derived from BEC analysis. Unlike the Berry-phase approach, which captures both ionic displacements and quantum-mechanical charge redistribution, the BEC method reflects a linearized approximation rooted in classical electrostatics. Across all halides, BEC-derived polarizations significantly underestimate the total P_s—by nearly 50% compared to Berry-phase results—underscoring the importance of electronic contributions beyond ionic movement. For instance, in $CsGeCl_3$, the BEC estimate yields $P_s \approx 10.86$ μC/cm^2, whereas the Berry-phase method reports 22.35 μC/cm^2 within PBE-GGA. Similar discrepancies are evident in $CsGeBr_3$ and $CsGeI_3$, with BEC-derived values trailing consistently behind. This divergence between the two methods reinforces the view that polarization in $CsGeX_3$ is not merely a function of atomic displacement. Instead, wavefunction asymmetry, covalent bonding, and lone-pair dynamics introduce non-negligible contributions that are invisible to classical treatments. Consequently, accurate modeling of P_s requires functionals and methodologies capable of resolving such quantum features, a point further supported by the sensitivity of P_s to exchange–correlation functional choice, as elaborated in the next section.

To gauge the role of electronic structure approximations in shaping the calculated spontaneous polarization, we systematically compare P_s values obtained using different exchange–correlation (XC) functionals. Notably, meta-GGA functionals such as mTASK and r2SCAN predict higher polarizations than the standard PBE-GGA across all halide compositions. This consistent enhancement highlights the superior ability of meta-GGA functionals to capture orbital asymmetry, charge localization, and mixed ionic–covalent bonding—core drivers of ferroelectricity. For example, in $CsGeCl_3$, the P_s increases from 22.35 μC/cm^2 with PBE-GGA to 23.29 μC/cm^2 using mTASK and 22.40 μC/cm^2 using r2SCAN. Analogous enhancements are observed for $CsGeBr_3$ and $CsGeI_3$, with polarization gains of up to $\sim$1 μC/cm^2 over PBE-GGA. These trends confirm that electronic effects are not only present but are also sensitive to the nuances of the underlying functional, which modulates the degree of electronic delocalization and hybridization. The improved polarization predictions from mTASK and r2SCAN align well with the known tendency of these functionals to strengthen short-range exchange interactions and correct self-interaction errors, thereby providing a more accurate description of bonding asymmetry. Importantly, the functional sensitivity of P_s also mirrors that of energy wells and band-edge states in these materials, reinforcing the intertwined nature of structural, electronic, and ferroelectric responses. Thus, polarization trends across halides and dopant levels should be interpreted in the context of the functional landscape, where electronic correlations and exchange mechanisms decisively shape the emergent ferroic behavior.

The pronounced sensitivity of spontaneous polarization to the choice of exchange–correlation functional underscores the electronic complexity underlying ferroelectric behavior in $CsGeX_3$ halide perovskites. While structural distortions—as captured by the c/a ratio—clearly modulate P_s, they do not fully determine its magnitude or trends across compositions and dopant levels. Instead, polarization emerges from a subtle interplay between lattice anisotropy and quantum electronic effects, including charge asymmetry, orbital hybridization, and lone-pair activity. The observed functional dependence reinforces this picture: functionals that better capture localized electronic interactions yield consistently higher polarization, aligning with trends in bonding character and charge redistribution. These findings motivate a deeper atomistic investigation into the origins of ferroelectricity, beyond structural metrics alone. In the next section, we dissect the electronic mechanisms responsible for the observed polarization patterns, drawing on Bader charge analysis and electron ELF mapping to elucidate the role of ionicity, covalency, and stereochemical activity in shaping the ferroic response. This structural–electronic decomposition offers a critical foundation for the rational design of high-performance, lead-free ferroelectric semiconductors.

TABLE SM4. Bader electron charge of atom q_{Atom} in (e) inside the pure compound $CsGeX_3$ and the doped compositions. The deviation of q_{Atom} from its formal value in free space $|\Delta q_{\text{Atom}}| = |q^{\text{Crystal}}_{\text{Atom}} - q^{\text{Free Space}}_{\text{Atom}}|$. Furthermore, the stoichiometric neutralization (SN) is also added to check the neutrality of the unit cell of the compounds.

ABX_3	q_A (e)	$\lvert\Delta q_A\rvert$ (e)	q_B (e)	Δq_B (e)	q_X (e)	$\lvert\Delta q_X\rvert$ (e)	q_{dop} (e)	$\lvert\Delta q_{\text{dop}}\rvert$ (e)	SN(e)
$CsGeCl_3$	0.8977	0.1023	1.0741	0.9259	-0.6657	0.3443	-	-	-0.02
$CsGeBr_3$	0.8770	0.1230	0.9043	1.0957	-0.5987	0.4013	-	-	-0.01
$CsGeI_3$	0.8682	0.1138	0.6483	1.3517	-0.5143	0.4557	-	-	-0.03
$Cs_{0.83}Rb_{0.17}GeCl_3$	0.9054	0.0946	1.1402	0.8598	-0.6688	0.3112	0.9184	0.0816	0.04
$Cs_{0.83}Rb_{0.17}GeBr_3$	0.8878	0.1122	0.9658	1.0442	-0.6069	0.3931	0.9075	0.0925	0.04
$Cs_{0.83}Rb_{0.17}GeI_3$	0.8728	0.1272	0.7278	1.2722	-0.5236	0.4764	0.8996	0.1004	0.03

C. Part III: Origin of Ferroelectricity

Part II, Sec. SM11 B, revealed a counterintuitive trend in which spontaneous polarization (P_s) does not directly scale with the degree of lattice distortion (quantified by the c/a ratio), suggesting that structural anisotropy alone cannot fully account for the observed ferroic behavior. To resolve this discrepancy, Part III turns to the quantum-electronic origins of ferroelectricity in $CsGeX_3$ perovskites and their Rb-substituted counterparts. To this end, in Sec. SM11 C 1, we analyze Bader electron charges to quantify charge transfer and distinguish ionic from covalent bonding contributions across the halide series. Then, in Sec. SM11 C 2, we use the ELF to probe the stereochemical activity of the Ge(II) lone pair and its role in driving polar displacements. Together, these analyses establish a microscopic framework that connects electronic structure to macroscopic polarization, bridging the gap between geometric trends and functional ferroic response.

1. *Bonding Character and Charge Redistribution via Bader Analysis*

As established in Sec. SM11 B 3, the halide-dependent trends in spontaneous polarization P_s defy expectations based on structural distortion alone, as quantified by the c/a ratio. Notably, $CsGeCl_3$ shows the highest P_s despite having the lowest c/a. To uncover the microscopic origins of this discrepancy, we examine bonding asymmetry and ionicity via Bader charge analysis.

This method, grounded in the quantum theory of atoms in molecules (QTAIM), partitions the electron density $\rho(\mathbf{r})$ into atom-centered basins using zero-flux surfaces (see Sec. SM8 C). The Bader charge q_Ω is obtained by integrating $\rho(\mathbf{r})$ over these basins [Eq. (SM25)], with surfaces defined by Eq. (SM24). The deviation $|\Delta q_{\text{Atom}}|$ from nominal free-space charges serves as a probe of covalency versus ionicity (Table SM4), and the stoichiometric neutralization (SN) [Eq. (SM28)] confirms global charge balance.

For the undoped $CsGeX_3$ compounds, A-site Cs atoms show small deviations ($|\Delta q_A| \approx 0.10$–$0.12\ e$), indicative of their ionic character. In contrast, Ge atoms exhibit larger deviations ($\Delta q_B = 0.93$–$1.35\ e$), reflecting greater covalency. Halogens follow an increasing trend in $|\Delta q_X|$ from Cl to I, signaling a progressive increase in covalent bonding with increasing halogen atomic number; accordingly, Ge–Cl is the most ionic and Ge–I the most covalent in this series. This mirrors the polarization trend from Sec. SM11 B 2, where $CsGeCl_3$ exhibits stronger P_s than $CsGeI_3$, despite lower distortion.

With Rb doping, several notable patterns emerge. The dopant Rb exhibits the smallest deviations ($|\Delta q_{\text{dop}}| = 0.08$–$0.10\ e$), consistent with its ionic role. However, Ge atoms show reduced Δq_B values upon doping, indicating weakened covalent Ge–X bonding. For example, Δq_B drops from 0.93 to 0.86 e (Cl), 1.10 to 1.04 e (Br), and 1.35 to 1.27 e (I). Corresponding changes reveal a halogen-dependent evolution under Rb doping: for I-based compounds, covalency increases on the I site (higher $|\Delta q_X|$) even as Ge becomes slightly more ionic (lower $|\Delta q_B|$), yielding a modest net increase in Ge–I bond polarizability, whereas Cl/Br-based compounds show slightly increased Ge–Cl/Ge–Br ionicity.

These changes support the observed increase in P_s upon doping (Table SM3 and Sec. SM11 B 2).

Overall, these findings reinforce the central premise that ferroelectricity in $CsGeX_3$ is governed not solely by structural distortion but also by electronic bonding asymmetry. The degree of ionicity, modulated through both halogen chemistry and A-site substitution, critically determines the magnitude of P_s. These insights build upon the broader framework of compositional tuning for ferroic enhancement, as discussed in Sec. SM11 B.

Nonetheless, Bader analysis, while precise in quantifying atomic charge redistribution, lacks spatial resolution for capturing orbital-level asymmetries—particularly the lone-pair localization on Ge(II) cations, which plays a pivotal role in stereochemically driven ferroelectricity. To resolve this, we now proceed to Sec. SM11 C 2, where the ELF provides a complementary orbital-level picture of electron asymmetry and lone-pair activity across the halide series.

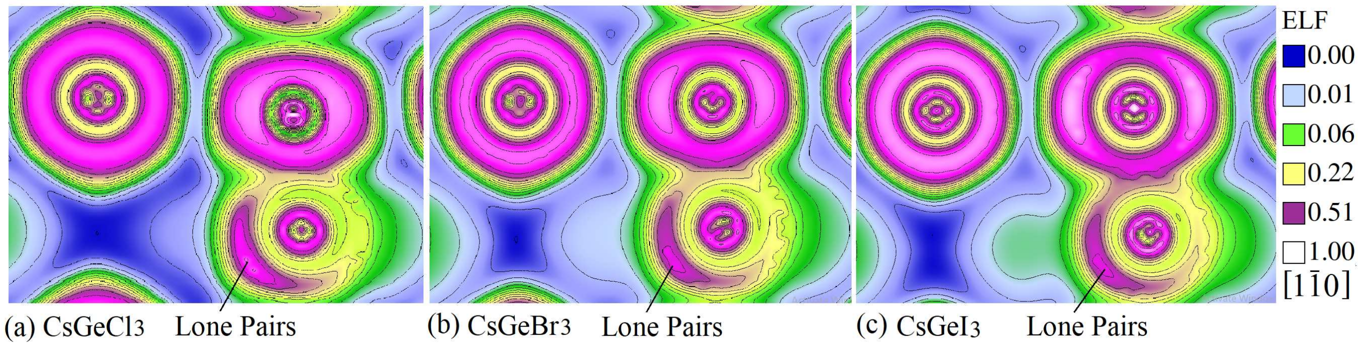

FIG. SM14. ELF contour maps for (a) $CsGeCl_3$, (b) $CsGeBr_3$, and (c) $CsGeI_3$ projected onto the [1$\bar{1}$0] crystallographic plane. The top-left atom corresponds to Cs, the top-right to the halogen (Cl, Br, or I), and the bottom-right to Ge. The ELF, ranging from 0 (blue, fully delocalized) to 1 (white, fully localized), highlights strong lone-pair localization near Ge atoms, with $CsGeCl_3$ exhibiting the most intense localization (ELF > 0.51), followed by $CsGeBr_3$ and $CsGeI_3$. ELF calculations were performed using the mTASK meta-GGA functional [20] and `VX_HCTH407` local potentials [21], providing high-fidelity descriptions of electron localization essential for lone-pair analysis. These observations are consistent with the quantitative normalized ELF values extracted from image-based analysis, supporting the trend of decreasing ferroelectric polarization strength across the $CsGeX_3$ series (Cl > Br > I).

TABLE SM5. Comparison of normalized ELF values, spontaneous polarization strength, and structural distortion in $CsGeX_3$ (X = Cl, Br, I) compounds. The normalized ELF values quantify the Ge-centered lone-pair localization. Polarization strength is inferred from spontaneous polarization (P_s), and structural distortion is assessed from the c/a ratio, where a larger c/a indicates greater lattice distortion away from the cubic limit (c/a = 1).

Compound	ELF Trend	P_s Trend	Distortion (c/a) Trend
$CsGeCl_3$	Most pronounced (0.264)	Strongest (22.35 $\mu C/cm^2$)	Least pronounced (1.244)
$CsGeBr_3$	Intermediate (0.259)	Moderate (19.02 $\mu C/cm^2$)	Intermediate (1.263)
$CsGeI_3$	Least pronounced (0.225)	Weakest (17.25 $\mu C/cm^2$)	Most pronounced (1.277)

2. *Electron Localization as the Microscopic Origin of Ferroelectricity*

To reconcile the observed inconsistencies between structural distortion (c/a, Sec. SM11 B 3), spontaneous polarization (P_s, Sec. SM11 B 2), and charge transfer asymmetry (Δq, Sec. SM11 C 1), we shift focus from geometric and ionic metrics to a quantum-electronic perspective rooted in stereochemical lone-pair activity. In this context, the ELF serves as a spatially resolved measure of electron localization that directly probes the presence of non-bonding s^2 lone pairs on Ge(II). As established in Sec. SM8 D, ELF is defined via the excess Pauli kinetic energy density [Eq. (SM31)] and ranges between 0 (fully delocalized) and 1 (fully localized). High ELF values near the Ge atom signal asymmetric charge confinement, which is a hallmark of stereochemically active lone pairs capable of inducing polar lattice distortions. By quantifying ELF across the $CsGeX_3$ (X = Cl, Br, I) series, we aim to bridge the gap between localized orbital asymmetry and macroscopic ferroic behavior—thereby identifying a microscopic origin of ferroelectricity that cannot be captured solely by structural parameters or Bader charges.

Figure SM14 presents ELF contour maps for $CsGeCl_3$, $CsGeBr_3$, and $CsGeI_3$, each projected onto the crystallographic [1$\bar{1}$0] plane to emphasize electron localization around Ge centers. In all cases, the Ge atom (bottom-right corner) is surrounded by asymmetric, lobe-shaped high-ELF regions, indicating the presence of stereochemically active $4s^2$ lone pairs. Among the three halides, $CsGeCl_3$ displays the most intense localization with ELF values exceeding 0.51, while $CsGeBr_3$ exhibits slightly weaker confinement, and $CsGeI_3$ reveals the most diffuse electron density distribution. This systematic attenuation of ELF intensity from Cl to I directly mirrors the trend in spontaneous polarization reported in Sec. SM11 B 2, where $CsGeCl_3$ shows the highest P_s and $CsGeI_3$ the lowest. Crucially, these ELF trends run counter to the structural distortion captured by the c/a ratio (Sec. SM11 B 3), where $CsGeI_3$ exhibits the largest distortion but weakest polarization. This inverse relationship underscores the central premise of this section: that lone-pair localization—not structural elongation—is the microscopic driver of ferroelectricity in $CsGeX_3$.

To complement these visual trends with quantitative precision, we developed a custom Python-based image processing framework, detailed in Sec. SM9, to extract normalized ELF values centered on the Ge sites. The workflow segments ELF contour maps in the HSV color space, isolates semicircular lone-pair features through morphological operations, and eliminates contributions from the Ge atomic core. This approach yields dimensionless ELF metrics normalized to the total projected ELF area, allowing for direct comparison across chemically distinct compounds. The resulting normalized ELF values are 0.264 for $CsGeCl_3$, 0.259 for $CsGeBr_3$, and 0.225 for $CsGeI_3$, as summarized in Table SM5. These metrics robustly follow the trend in spontaneous polarization (Cl > Br > I), reinforcing the hypothesis from Sec. SM11 B 2 that enhanced electron localization around Ge(II) atoms is the primary contributor to ferroelectric strength. The consistency between visual and quantitative ELF analyses confirms the reliability of electron localization as a transferable descriptor of lone-pair stereochemical activity in halide perovskites.

A striking insight emerges when comparing the normalized ELF values with the c/a ratios listed in Table SM5 and analyzed in Sec. SM11 B 3. $CsGeI_3$ exhibits the highest structural distortion ($c/a = 1.277$), yet its ELF localization (0.225) and spontaneous polarization ($P_s = 17.25\ \mu C/cm^2$) are the weakest among the series. Conversely, $CsGeCl_3$ shows the smallest c/a distortion (1.244) but the strongest ELF localization (0.264) and the highest P_s (22.35 $\mu C/cm^2$). This inverse correlation underscores a key conclusion: structural distortion alone is insufficient to explain ferroelectric behavior in $CsGeX_3$ compounds. Rather, it is the quantum-mechanical asymmetry arising from stereochemically active Ge(II) lone pairs—quantified via ELF—that better governs the polarization strength. The stronger lone-pair localization in $CsGeCl_3$ is associated with predominantly ionic Ge–Cl bonds, whereas the more diffuse lone-pair distribution in $CsGeI_3$ corresponds to more covalent Ge–I bonding, in agreement with the Bader charge analysis in Sec. SM11 C 1. This distinction reconciles the discrepancy identified in Sec. SM11 B 3 between geometric metrics and macroscopic polarization, and further validates the ELF as a superior microscopic descriptor of ferroic behavior.

Taken together, the ELF analysis consolidates a unifying microscopic framework that reconciles the discrepancies across Secs.SM11 B 3,SM11 B 2, and SM11 C 1. By directly quantifying the stereochemical activity of Ge(II) lone pairs, the ELF provides a robust, geometry-independent metric for ferroelectric strength in $CsGeX_3$. The observed ELF trend (Cl > Br > I) mirrors that of spontaneous polarization and the ionic-to-covalent character trend revealed by Bader charge asymmetry (Sec. SM11 C 1), yet departs from the structural distortion trend—thereby highlighting the primacy of electronic asymmetry over geometric elongation. The integration of high-fidelity ELF simulations using mTASK+`VX_HCTH407` (Sec. SM9) with image-based normalization enables reproducible, transferable quantification of lone-pair localization, scalable across diverse perovskite chemistries. As such, this framework not only explains the origin of polarization in $CsGeX_3$, but also establishes ELF as a predictive descriptor for designing new lead-free optoferroelectric materials.

The ELF is fundamentally a measure of the probability of finding an electron with parallel spin in the vicinity of another reference electron, thereby serving as a spatial indicator of electron pairing and localization (Sec. SM8 D). A high ELF value at the *mid-bond* typically signals significant interatomic electron sharing—characteristic of strong covalent bonding—whereas lower mid-bond ELF together with stronger localization on one atom reflects reduced covalent contribution and a shift toward more ionic character. In $CsGeCl_3$, pronounced ELF maxima concentrate around the Ge $4s^2$ lone pair and polarize toward Cl, with relatively low mid-bond ELF, consistent with a more ionic Ge–Cl bond (Sec. SM11 C 1) and a deeper double-well (Sec. SM11 B 1). By contrast, $CsGeI_3$ exhibits enhanced mid-bond ELF, reflecting more covalent Ge–I bonding and a shallower double-well with greater lattice softness. ELF alone cannot definitively establish bond character; complementary analyses such as Bader charge partitioning (Sec. SM11 C 1), projected density of states (PDOS), or crystal orbital Hamilton population (COHP) analysis are recommended.

Future efforts may exploit this approach to guide chemical substitutions, dimensionality tuning, or strain-engineering strategies aimed at enhancing functional response in environmentally benign perovskite systems.

[1] N. Thi Han, V. Khuong Dien, and M.-F. Lin, Electronic and optical properties of $CsGeX_3$ (X= Cl, Br, and I) compounds, ACS Omega **7**, 25210 (2022), https://doi.org/10.1021/acsomega.2c02088.

[2] Y. Zhang, E. Parsonnet, A. Fernandez, S. M. Griffin, H. Huyan, C.-K. Lin, T. Lei, J. Jin, E. S. Barnard, A. Raja, P. Behera, X. Pan, R. Ramesh, and P. Yang, Ferroelectricity in a semiconducting all-inorganic halide perovskite, Sci. Adv. **8**, eabj5881 (2022).

[3] Z.-G. Lin, L.-C. Tang, and C.-P. Chou, Study on mid-IR NLO crystals $CsGe(Br_xCl_{1-x})_3$, Optical Materials **31**, 28 (2008).

[4] U. Schwarz, F. Wagner, K. Syassen, and H. Hillebrecht, Effect of pressure on the optical-absorption edges of $csgebr_3$ and $csgecl_3$, Phys. Rev. B **53**, 12545 (1996).

[5] M. Berry, Classical adiabatic angles and quantal adiabatic phase, J. Phys. A: Math. Gen. **18**, 15 (1985).

[6] D. Vanderbilt, Berry-phase theory of proper piezoelectric response, J. Phys. Chem. Solids **61**, 147 (2000).

[7] D. Xiao, M.-C. Chang, and Q. Niu, Berry phase effects on electronic properties, Rev. Mod. Phys. **82**, 1959 (2010).

[8] M. S. Hybertsen and S. G. Louie, Electron correlation in semiconductors and insulators: Band gaps and quasiparticle energies, Phys. Rev. B **34**, 5390 (1986).

[9] L. Hedin, New Method for Calculating the One-Particle Green's Function with Application to the Electron-Gas Problem, Phys. Rev. **139**, A796 (1965).

[10] E. E. Salpeter and H. A. Bethe, A Relativistic Equation for Bound-State Problems, Phys. Rev. **84**, 1232 (1951).

[11] G. Onida, L. Reining, and A. Rubio, Electronic excitations: density-functional versus many-body Green's-function approaches, Rev. Mod. Phys. **74**, 601 (2002).

[12] X. Leng, F. Jin, M. Wei, and Y. Ma, GW method and Bethe–Salpeter equation for calculating electronic excitations, WIREs Computational Molecular Science **6**, 532 (2016).

[13] X. Blase, I. Duchemin, D. Jacquemin, and P.-F. Loos, The Bethe–Salpeter Equation Formalism: From Physics to Chemistry, J. Phys. Chem. Lett. **11**, 7371 (2020), pMID: 32787315, https://doi.org/10.1021/acs.jpclett.0c01875.

[14] W. Kohn and L. J. Sham, Self-Consistent Equations Including Exchange and Correlation Effects, Phys. Rev. **140**, A1133 (1965).

[15] G. Strinati, Application of the green's functions method to the study of the optical properties of semiconductors, La Rivista del Nuovo Cimento (1978-1999) **11**, 1 (1988).

[16] S. Sagmeister and C. Ambrosch-Draxl, Time-dependent density functional theory versus Bethe–Salpeter equation: an all-electron study, Phys. Chem. Chem. Phys. **11**, 4451 (2009).

[17] Y. Gillet, *Ab initio study of Raman and optical spectra of crystalline materials and their temperature dependence*, Phd thesis, Université catholique de Louvain, Louvain-la-Neuve, Belgium (2017).

[18] S. Rahimi, R. Ebrahimi-Jaberi, F. Jalali-Asadabadi, L. Mollabashi, and S. Jalali-Asadabadi, Influence of (Ba,F) multidoping on structural, magnetic, optical, and electrical properties as well as performance enhancement of multiferroic $BiFeO_3$, Phys. Rev. B **106**, 115205 (2022).

[19] T. Sander, E. Maggio, and G. Kresse, Beyond the Tamm-Dancoff approximation for extended systems using exact diagonalization, Phys. Rev. B **92**, 045209 (2015).

[20] J. Doumont, F. Tran, and P. Blaha, Implementation of self-consistent MGGA functionals in augmented plane wave based methods, Phys. Rev. B **105**, 195138 (2022).

[21] B. Neupane, H. Tang, N. K. Nepal, S. Adhikari, and A. Ruzsinszky, Opening band gaps of low-dimensional materials at the meta-GGA level of density functional approximations, Phys. Rev. Mater. **5**, 063803 (2021).

[22] S. Ahmed, J. Kivinen, B. Zaporzan, L. Curiel, S. Pichardo, and O. Rubel, BerryPI: A software for studying polarization of crystalline solids with WIEN2k density functional all-electron package, Comput. Phys. Commun. **184**, 647 (2013).

[23] M. V. Berry, Quantal phase factors accompanying adiabatic changes, Proc. R. Soc. A **392**, 45 (1984).

[24] S. Rahimi, S. Jalali-Asadabadi, P. Blaha, and F. Jalali-Asadabadi, Nonzero spontaneous electric polarization in metals: novel predictive methods and applications, Scientific Reports **14**, 672 (2024).

[25] R. F. W. Bader, A quantum theory of molecular structure and its applications, Chem. Rev. **91**, 893 (1991).

[26] R. F. W. Bader, *Atoms in Molecules: A Quantum Theory (International Series of Monographs on Chemistry)* (Oxford University Press, 1994).

[27] P. Hohenberg and W. Kohn, Inhomogeneous Electron Gas, Phys. Rev. **136**, B864 (1964).

[28] A. O. de-la Roza, M. Blanco, A. M. Pendás, and V. Luaña, Critic: a new program for the topological analysis of solid-state electron densities, Comput. Phys. Commun. **180**, 157 (2009).

[29] A. O. de-la Roza, E. R. Johnson, and V. Luaña, Critic2: A program for real-space analysis of quantum chemical interactions in solids, Comput. Phys. Commun. **185**, 1007 (2014).

[30] M. Yazdani-Kachoei, S. Jalali-Asadabadi, and N. Arianmehr, Topological analysis of $CeMIn_5$ (M = Co, Rh) electron charge densities, Comput. Mater. Sci. **164**, 205 (2019).

[31] M. Yazdani-Kachoei and S. Jalali-Asadabadi, Topological analysis of electron density in half-Heusler ZrXBi (X = Co, Rh) compounds: A density functional theory study accompanied by Bader's quantum theory of atoms in molecules, J. Alloys Compd. **828**, 154287 (2020).

[32] K. Koumpouras and J. A. Larsson, Distinguishing between chemical bonding and physical binding using electron localization function (ELF), J. Phys.: Condens. Matter **32**, 315502 (2020).

[33] A. Gulans, S. Kontur, C. Meisenbichler, D. Nabok, P. Pavone, S. Rigamonti, S. Sagmeister, U. Werner, and C. Draxl, exciting: a full-potential all-electron package implementing density-functional theory and many-body perturbation theory, J. Phys.: Condens. Matter **26**, 363202 (2014).

[34] E. Sjöstedt, L. Nordström, and D. Singh, An alternative way of linearizing the augmented plane-wave method, Solid State Commun. **114**, 15 (2000).

[35] J. P. Perdew, K. Burke, and M. Ernzerhof, Generalized gradient approximation made simple, Phys. Rev. Lett. **77**, 3865 (1996).

[36] P. Blaha, K. Schwarz, G. K. H. Madsen, D. Kvasnicka, J. Luitz, R. Laskowski, F. Tran, and L. D. Marks, WIEN2k, An Augmented Plane Wave + Local Orbitals Program for Calculating Crystal Properties, Karlheinz Schwarz, Technische Universität Wien, Vienna, Austria, ISBN 3-9501031-1-2 (2021).

[37] G. Xiang, Y. Wu, M. Zhang, J. Leng, C. Cheng, and H. Ma, Strain-induced bandgap engineering in $CsGeX_3$ (X = I, Br or Cl) perovskites: insights from first-principles calculations, Phys. Chem. Chem. Phys. **24**, 5448 (2022).

[38] A. C. Dias, M. P. Lima, and J. L. F. Da Silva, Role of Structural Phases and Octahedra Distortions in the Optoelectronic and Excitonic Properties of $CsGeX_3$ (X = Cl, Br, I) Perovskites, J. Phys. Chem. C **125**, 19142 (2021), https://doi.org/10.1021/acs.jpcc.1c05245.

[39] A. J. Kale, B. Pal, and A. Dixit, Theoretical Insights on Pb-Free Rhombohedral $CsGeI_3$ over Cubic $CsMX_3$ (M-: Pb, Sn, Ge, and X-: Cl, Br, I) Perovskite-Based Single-Junction Solar Cell with Efficiency >30%, physica status solidi (a) **221**, 2300464 (2024), https://onlinelibrary.wiley.com/doi/pdf/10.1002/pssa.202300464.

[40] T. Krishnamoorthy, H. Ding, C. Yan, W. L. Leong, T. Baikie, Z. Zhang, M. Sherburne, S. Li, M. Asta, N. Mathews, and S. G. Mhaisalkar, Lead-free germanium iodide perovskite materials for photovoltaic applications, J. Mater. Chem. A **3**, 23829 (2015).

[41] L.-C. Tang, C.-S. Chang, L.-C. Tang, and J. Y. Huang, Electronic structure and optical properties of rhombohedral $CsGeI_3$ crystal, J. Phys.: Condens. Matter **12**, 9129 (2000).

[42] R. A. Jishi, O. B. Ta, and A. A. Sharif, Modeling of Lead Halide Perovskites for Photovoltaic Applications, J. Phys. Chem. C **118**, 28344 (2014), https://doi.org/10.1021/jp5050145.

[43] U.-G. Jong, C.-J. Yu, Y.-H. Kye, Y.-G. Choe, W. Hao, and S. Li, First-Principles Study on Structural, Electronic, and Optical Properties of Inorganic Ge-Based Halide Perovskites, Inorg. Chem. **58**, 4134 (2019), https://doi.org/10.1021/acs.inorgchem.8b03095.

[44] J. Even, L. Pedesseau, J.-M. Jancu, and C. Katan, Dft and $k \cdot p$ modelling of the phase transitions of lead and tin halide perovskites for photovoltaic cells, Phys. Status Solidi RRL **8**, 31 (2014).

[45] I. E. Castelli, J. M. García-Lastra, K. S. Thygesen, and K. W. Jacobsen, Bandgap calculations and trends of organometal halide perovskites, APL Mater. **2**, 081514 (2014).

[46] W. Azeem, M. K. Shahzad, S. Hussain, F. Azad, M. J. Aslam, V. Tirth, H. Alqahtani, A. Algahtani, T. Al-Mughanam, and Y. H. Wong,

Investigation of semiconductor to metallic transitions of perovskite $CsGeCl_3$ material through induced pressure: a DFT calculation for photovoltaic and optoelectronic applications, Materials for Renewable and Sustainable Energy **14**, 1 (2025).
[47] J. Qu, Y. Wang, Z. Li, M. Li, T. Pei, N. Li, D. Jiang, B. Yang, B. Li, M. Ye, P. Zhu, Y. Wang, G. Liu, X. Wang, and W. Yang, Origin of Pressure-Induced Nonlinear Optical Property Enhancement in $CsGeCl_3$ Perovskite: $[GeCl_6]$ Octahedron Distortion and Band Gap Closing, J. Am. Chem. Soc. **147**, 6717 (2025), pMID: 39939151.
[48] D.-K. Seo, N. Gupta, M.-H. Whangbo, H. Hillebrecht, and G. Thiele, Pressure-Induced Changes in the Structure and Band Gap of $CsGeX_3$ (X = Cl, Br) Studied by Electronic Band Structure Calculations, Inorg. Chem. **37**, 407 (1998), pMID: 11670288.
[49] G. Liu, S. Zhang, W. Jiang, and W. Cao, Losses in ferroelectric materials, Mater. Sci. Eng. R Rep. **89**, 1 (2015).
[50] M. Azadparvar, H. A. Rahnamaye Aliabad, and E. G. Özdemir, Optoelectronic and thermoelectric properties of Sb_2S_3 under hydrostatic pressure for energy conversion, AIP Adv. **13**, 065218 (2023).
[51] N. Chelil, M. Sahnoun, Z. Benhalima, R. Larbi, and S. M. Eldin, Insights into the relationship between ferroelectric and photovoltaic properties in $CsGeI_3$ for solar energy conversion, RSC advances **13**, 1955 (2023).
[52] R. Chen, B. Luo, C. Liu, X. Ma, L. Qiao, B. Yao, R. Gao, Z. Feng, J. Liu, H. Lin, X. Kong, and W. Ren, Polarization Controlled Photocurrent in Perovskite $CsGeX_3$ (X = Cl, Br, I), J. Phys. Chem. C **127**, 19788 (2023), https://doi.org/10.1021/acs.jpcc.3c04619.
[53] Y. Zhang, J. Sun, J. P. Perdew, and X. Wu, Comparative first-principles studies of prototypical ferroelectric materials by LDA, GGA, and SCAN meta-GGA, Phys. Rev. B **96**, 035143 (2017).
[54] T. Shigenari, Raman spectra of soft modes in ferroelectric crystals, in *Ferroelectric Materials-Synthesis and Characterization* (IntechOpen, 2015).
[55] M. Dawber, K. M. Rabe, and J. F. Scott, Physics of thin-film ferroelectric oxides, Rev. Mod. Phys. **77**, 1083 (2005).
[56] L. C. Tang, J. Y. Huang, C. S. Chang, M. H. Lee, and L. Q. Liu, New infrared nonlinear optical crystal $CsGeBr_3$: synthesis, structure and powder second-harmonic generation properties, J. Phys.: Condens. Matter **17**, 7275 (2005).